Search for new dimuon resonances with the ATLAS detector at the LHC

Knut Oddvar Høie Vadla
Department of Physics
University of Oslo

Thesis presented for the degree of
Master of Science

June 2015

Abstract

A search for new resonances in the dimuon invariant mass spectrum, with the ATLAS detector at the LHC, is performed in this thesis. The data stem from proton-proton collisions at a center-of-mass energy of $\sqrt{s} = 8$ TeV in 2012, and correspond to an integrated luminosity of approximately 5.1 fb^{-1}. The analysis is performed within the new analysis model in ATLAS, developed for storage and handling of data in the upcoming Run 2 of data-taking at the LHC, which is scheduled to start in June 2015. The experimental data are compared to the estimated backgrounds, obtained from Monte Carlo simulated samples, and are found to be in relatively good agreement. Hence, no significant deviations from the Standard Model expectations are found. The work is performed completely within the new analysis model, which confirms that the model is well functioning and is in time to be deployed for the upcoming LHC Run 2. As a follow-up to the 8 TeV analysis, new simulated samples at $\sqrt{s} = 13$ TeV have been considered in the thesis, to estimate the background for resonance searches in the dimuon channel, in preparation for Run 2 at higher energy and luminosity.

Acknowledgments

First, I would like to thank my supervisor Farid Ould-Saada, for giving me valuable advise on which directions to follow, and for sharing his extensive experience from his work in this field. My co-supervisor, James Catmore, also deserves a big thanks for all his help with both analysis and programming related technicalities, and for keeping me up to date on the ongoing development of the new analysis model, which proved very convenient. Thank you, both Farid and James, for always welcoming questions and for your positive attitude.

I also want to give a special thanks to Magnar Kopangen Bugge, Vanja Morisbak and Eirik Gramstad, for sharing their knowledge and experience from work with similar analyses. And to the rest of the experimental particle physics group at the University of Oslo, thank you for providing an enjoyable environment to be a part of, and for the social gatherings we have had also outside of the university.

Contents

Introduction **3**

1 The Standard Model of particle physics and theories beyond **4**
1.1 The particles and forces . . . 4
1.1.1 The fermions: leptons and quarks . . . 4
1.1.2 The gauge bosons and the fundamental forces . . . 5
1.1.3 The Higgs boson . . . 7
1.2 Lagrangian field theory . . . 7
1.3 The Klein-Gordon field . . . 8
1.4 The Dirac field . . . 11
1.5 Gauge theories . . . 12
1.5.1 Quantum electrodynamics (QED) . . . 13
1.5.2 Quantum chromodynamics (QCD) . . . 15
1.5.3 Electroweak theory . . . 17
1.6 The Brout-Englert-Higgs mechanism . . . 21
1.7 Shortcomings of the Standard Model - and theories beyond . . . 23
1.7.1 E_6-motivated Z' models . . . 23
1.7.2 The sequential Standard Model Z' . . . 24
1.7.3 Graviton excitations in the Randall-Sundrum models . . . 24

2 The LHC and the ATLAS detector **25**
2.1 The LHC and particle collider experiments . . . 25
2.1.1 Center-of-mass energy and invariant mass . . . 25
2.1.2 Interaction cross-section and luminosity . . . 26
2.2 Interactions of particles with matter . . . 26
2.2.1 Charged particles . . . 27
2.2.2 Photons . . . 28
2.2.3 Electromagnetic showers . . . 28
2.2.4 Hadrons . . . 29
2.3 The ATLAS detector at the LHC . . . 29
2.3.1 The ATLAS coordinate system . . . 30
2.3.2 The inner detector . . . 30
2.3.3 The electromagnetic calorimeters . . . 31
2.3.4 The hadronic calorimeters . . . 32
2.3.5 The muon spectrometer . . . 33
2.3.6 The trigger system . . . 34

3 The new analysis model in ATLAS for Run 2 at $\sqrt{s} = 13$ TeV **37**
3.1 The new event data model . . . 37
3.2 The derivation framework . . . 38
3.3 Performance . . . 40

4 8 TeV analysis **41**
4.1 Event and muon selection . . . 41
4.1.1 Event level . . . 42
4.1.2 Muon level . . . 44
4.1.3 Dimuon level . . . 44
4.2 Experimental data . . . 45
4.3 Background estimation . . . 45
4.3.1 Processes . . . 46
4.3.2 Monte Carlo samples . . . 47
4.4 Z' signal samples . . . 48
4.5 Comparison of data and estimated background . . . 50
4.5.1 Invariant mass distribution . . . 50
4.5.2 Kinematic properties . . . 52
4.6 Comparison with the ATLAS publication at $\sqrt{s} = 8$ TeV . . . 53
4.6.1 Data and Monte Carlo samples . . . 54
4.6.2 Higher-order corrections to cross-sections . . . 54
4.6.3 Muon selection . . . 55
4.6.4 Momentum resolution and smearing . . . 55
4.6.5 Systematic uncertainties . . . 56
4.6.6 Invariant mass distribution . . . 57
4.7 Angular distributions . . . 59
4.8 Summary . . . 61
4.9 Experimental limits on new physics . . . 62

5 13 TeV analysis **65**
5.1 Event and muon selection . . . 65
5.2 Background estimation . . . 66
5.2.1 Monte Carlo samples . . . 67
5.2.2 Z' signal . . . 69
5.2.3 Invariant mass distribution . . . 69
5.2.4 Kinematic properties . . . 70
5.3 Involvement in the exotic dilepton analysis group in ATLAS . . . 71
5.4 Summary . . . 71

Conclusions **72**

Appendices **73**

A Data and simulation samples **74**
A.1 8 TeV samples . . . 74
A.1.1 Experimental data and Good Runs List . . . 74
A.1.2 Simulation . . . 74
A.2 13 TeV samples . . . 75
A.2.1 Simulation . . . 75

Introduction

In 2011 and 2012 CERN's Large Hadron Collider (LHC) provided the first period of proton-proton (pp) collisions for data-taking, referred to as "Run 1", at a center-of-mass energy of $\sqrt{s} = 7$ TeV during the first year and at $\sqrt{s} = 8$ TeV during the second. This first round of experiments proved a huge success due to the discovery of a new particle that is consistent with the long-awaited Higgs boson. This particle is predicted in the Standard Model (SM) to be the manifestation of a vacuum field, that is responsible for the mechanism by which the fundamental massive particles acquire their masses. The discovery made by the ATLAS and CMS experiments, and announced on 4 July 2012, contributed to Francois Englert and Peter Higgs being awarded the Nobel prize in physics the following year, "for the theoretical discovery of a mechanism that contributes to our understanding of the origin of mass of subatomic particles".

Other important results have also been obtained by CERN's experiments during Run 1, including improvements of exclusion limits set on new particles and phenomena, which are predicted by theories that go beyond the SM. These theories address aspects of nature which are currently unknown. Common to many of them are the predictions of new neutral bosons, which form the motivation for the search performed in this thesis.

In February 2013 the first long shutdown period at the LHC was initiated, which lasted for about two years, and where machines and equipment were overhauled and upgraded to tackle the higher collision energies and rates planned for "Run 2" of pp collisions at $\sqrt{s} = 13$ TeV, currently expected to start up in June 2015. During the shutdown the ATLAS experiment decided to also renew its Run 1 analysis model, for storage and handling of data. This resulted in the development of a new and more efficient data format, along with a new "derivation framework" for centralized production of intermediate-sized "derived formats", aimed at specific analyses.

In this thesis, a search for resonances in the dimuon invariant mass spectrum, from data taken during pp collisions at $\sqrt{s} = 8$ TeV, is compared to the expected background from SM processes. The work is performed within the new analysis model in ATLAS, and hence provides a verification that the aspects of the model addressed in this work are ready for use in Run 2.

As a preparation for the upcoming pp collisions at $\sqrt{s} = 13$ TeV, the thesis will also consider some possibility studies in ATLAS of new dilepton resonances accommodating the new conditions. To this end, the background relevant for resonance searches in the dimuon channel will be estimated.

The thesis starts with an introduction to the contents of the Standard Model of particle physics, its mathematical formalism and theories addressing its limitations, in chapter 1. This is, in chapter 2, followed by a short overview of the Large Hadron Collider and the interactions of particles with matter, before introducing the different components of the ATLAS detector. Chapter 3 explains the features of the new analysis model to be used in ATLAS in Run 2. The main work of the thesis is presented in chapter 4, which contains a search for resonant deviations of experimental data from the estimated background at $\sqrt{s} = 8$ TeV in the dimuon channel, within the new analysis model. Finally, there will be given an estimate of the background to dimuon resonance searches at $\sqrt{s} = 13$ TeV, in preparation for the upcoming run at the LHC.

Chapter 1

The Standard Model of particle physics and theories beyond

From what we know so far, everything in the universe is composed of a few basic building blocks called fundamental particles. We also know that there exist four fundamental forces, by which these particles interact with each other. Our knowledge about three of these forces (gravity not included) together with the elementary particles are collected in what is called the Standard Model (SM) of particle physics. This theory has been very successful in explaining the known particles and their interactions, but also in making precise predictions about particles and phenomena before they were discovered. The last proof of this being the discovery of a Higgs boson, which seems to be in agreement with the predicted SM Higgs boson. Through this the existence of the important Brout-Englert-Higgs mechanism is indicated, which breaks the electroweak symmetry and gives mass to the electroweak gauge bosons and the fermions.

1.1 The particles and forces

This section is based on the introductory parts of the books [1, 2].

1.1.1 The fermions: leptons and quarks

The elementary particles can be divided into smaller groups according to the properties they possess.

One of these properties is called spin. It is a quantum mechanical attribute that can only take certain discrete values, and gives the particles an intrinsic angular momentum. The classical analog of spin would be rotation of an object about its own axis. Experiments have not been able to measure the spatial size of the elementary particles, and they are in the SM considered as pointlike with no internal structure. Hence the classical description does not make sense in the current quantum mechanical interpretation of particles. Even so, spin is an important feature of the behavior of particles. We classify particles with half-integer spin as fermions and particles with integer spin as bosons.

Fermions can be referred to as matter particles, and are further divided into leptons and quarks. All stable matter is composed of what is called the first generation of fermions, which consists of the up (u) and down (d) quarks, that make up the protons $p(uud)$ and neutrons $n(udd)$ in the atomic nulei, along with the electron (e^-). The electron neutrino ν_e is also part of the first generation of fermions, but is not a part of the composition of matter. It is, however, involved in phenomena where matter transforms, like in nuclear β-decay ($n \to p + e^- + \bar{\nu}_e$, where the bar denotes antiparticle).

There are in total three generations of fermions, which in principle are heavier copies of the first generation. The second generation consists of the charm (c) and strange (s) quarks, and the muon (μ^-) and muon neutrino (ν_μ) leptons. The third and heaviest generation includes the top (t) and bottom/beauty (b) quarks, and the tau (τ^-) and tau neutrino (ν_τ) leptons. Particles of these two heavier generations are being produced in high-energetic processes, and will quickly decay to lighter and more stable particles. The three generations of fermions are summarized in Fig. 1.1.

The statement that particles are heavier in higher generations is not necessarily true for the neutrinos. They were at first thought to be massless, but have later been found to have some very small non-zero masses, although they have yet to be determined. Through the discovery of neutrino oscillations, we now know that the neutrinos referred to in the SM are merely "flavor" eigenstates which are superpositions of three different quantum mechanical mass eigenstates, called ν_1, ν_2 and ν_3. One of the reasons why we do not know the masses of the neutrinos, is that they only interact with other particles through the weak force, and are therefore extremely hard to measure in experiments. The fact that the masses are so small and are known to be very close in value, adds to the difficulty of determining them.

Apart from the neutrinos, which are electrically neutral, all the other fermions have an electric charge. The leptons have integer charges (e^-, μ^-, τ^-: -1), in terms of the electron charge, while the quarks have fractional electric charges (u, c, t: $+2/3$ and d, s, b: $-1/3$). Particles with an electric charge are affected by the electromagnetic force.

Unlike the leptons, the quarks also hold another quantum number, the so called color charge. This quantum number can take three different values or states, called red, green and blue. Particles having color charge feel the strong force. The nature of this interaction prohibits free single or bound particle states with a net color charge. Hence quarks cannot exist as free single particles (at least not in the low energy regime), but must make bound states with other quarks in order to appear collectively as "colorless" objects. This can be done by forming either three-quark states, called baryons ($\{r, g, b\}$ or $\{\bar{r}, \bar{g}, \bar{b}\}$), or two-quark states, called mesons ($\{i, \bar{i}\}$; where $i = r$, g, b).

In addition, each fermion has its own antiparticle, which is identical to its antipartner except with the electric charge and all other additive quantum numbers inverted. Since the neutrinos are electrically neutral, it is not established experimentally whether they have distinct antiparticles or whether they in fact are their own antiparticles (Majorana neutrinos).

1.1.2 The gauge bosons and the fundamental forces

In the Standard Model the electromagnetic, weak and strong forces are mediated by particles called gauge bosons. These are spin-1 particles, as opposed to the fermions with spin-1/2.

The photon, γ, is the particle mediating the electromagnetic interaction, and couples to particles with electric charge. It is massless, electrically neutral and stable, giving the electromagnetic force an infinite range. The photon arises from transverse polarization states of the electromagnetic field, and is responsible for electromagnetic radiation. The electromagnetic field also has scalar/time-like and longitudinal polarization states, which are responsible for the instantaneous Coulomb interaction between electrically charged particles, where oppositely charged particles experience a mutually attracting force and particles of equal charge experience a repelling force.

The weak interaction has three force carriers: the electrically neutral Z^0, and the electrically charged W^+ and W^-. They are all relatively heavy compared to the other SM particles (except the top quark and the Higgs boson), and have short lifetimes, giving the weak interaction a very short range. Even though its strength is of the same order of magnitude as the electromagnetic

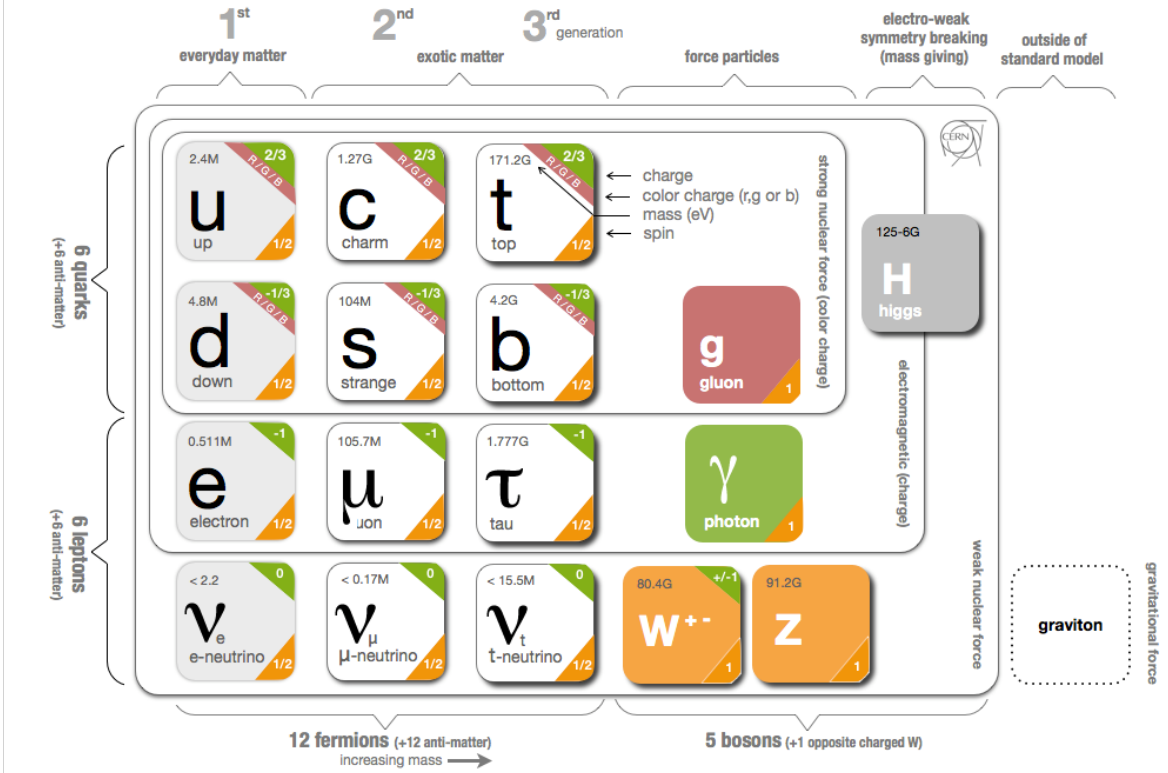

Figure 1.1: Graphic table of the contents of the Standard Model[1].

interaction at extremely short distances, it is already several orders of magnitude weaker at a distance of the proton radius ($\sim 10^{-15}$ m). This very short range is part of the reason why it is called the weak force. It separates from the other interactions by allowing charged currents, i.e. particles going in and out of the interaction vertex differing in one unit of electric charge, due to the exchange of a $W^{\pm}$ boson. It is also the only interaction to violate parity conservation, an operation of spatial inversion through the origin. This comes from the nature of the weak interaction, where the weak gauge bosons only couples to left-handed particle and right-handed antiparticle helicity states (helicity denotes the particle's spin-alignment projected onto the direction of its linear momentum).

In the strong interaction the gluon, g, is the mediator of the corresponding force. The gluon only interacts with particles with a color charge, and since it carries both color and anticolor itself, it not only interacts with quarks, but also with other gluons. There are in fact eight physical gluon states with different color combinations: $r\bar{g}$, $g\bar{r}$, $r\bar{b}$, $b\bar{r}$, $g\bar{b}$, $b\bar{g}$, $\frac{1}{\sqrt{2}}(r\bar{r} - g\bar{g})$ and $\frac{1}{6}(r\bar{r} + g\bar{g} - 2b\bar{b})$. In contrast to the electromagnetic interaction, where the force is getting weaker with increasing distance between electrically charged particles, the strong force grows stronger with increasing distance between two color-charged particles. Hence, quarks can in a sense be regarded as "more free" at shorter distances, a phenomenon called asymptotic freedom, and will be subjected to color confinement at larger distances, in order to maintain the bound colorless state. In high-energy collisions where a $q\bar{q}$-pair is produced in the final state, the

[1]Source: `https://cdsweb.cern.ch/journal/CERNBulletin/2012/35/News%20Articles/1473657?ln=en`

strong interaction between the two quarks moving away from each other holds enough energy to create new $q\bar{q}$-pairs, which again will split to new such quark-pairs, until they eventually have sufficiently low energy to form bound states of colorless hadrons. This process is called hadronization, where quarks and gluons will show up as "cones" of hadrons, called jets, in the detectors; one jet for each final state quark or gluon. At a distance corresponding to the proton radius, the strong force is about three orders of magnitude stronger than the electromagnetic force, and about eight orders of magnitude stronger than the weak force.

The gauge bosons along with some of their characteristics, are listed in Fig. 1.1.

1.1.3 The Higgs boson

The Higgs boson is the only particle in the Standard Model which has spin-0, a so called scalar particle. So when it finally was discovered by ATLAS [3] and CMS [4] in 2012, it was the first fundamental scalar particle ever to be confirmed.

But there are other aspects with this particle that made the discovery so important and long awaited. The Higgs boson was the last missing piece in the Standard Model, and perhaps most importantly, it confirmed the existence of its associated Higgs field. This field was proposed to be responsible for the electroweak symmetry breaking [5–10], which, apart from the photon, made the otherwise massless gauge bosons of the electroweak symmetry acquire masses. They do so through interactions with the non-zero vacuum expectation value of the Higgs field. This is called the Brout-Englert-Higgs mechanism, which also can be used to explain the masses of the fermions.

The discovered Higgs boson has been found to be electrically neutral, have positive parity and a mass of $m_H = 125.09 \pm 0.21\,(\text{stat}) \pm 0.11\,(\text{syst})$ GeV, as obtained by the combined mass measurements [11] of ATLAS and CMS. Along with its decay rates to other SM particles, its properties are still found to be in agreement with the SM Higgs, but more investigation is needed in order to properly confirm that this is in fact the Higgs boson predicted by the Standard Model. It is listed together with the rest of the SM particles in Fig. 1.1.

1.2 Lagrangian field theory

This section is mostly based on chapter 2 in Ref . [12]

The mathematical formalism of the Standard Model is based on the concept of quantized fields. Each set of particle/antiparticle has its own field or set of field components, e.g. $\phi_r(x)$, where $r = 1, \ldots, N$ and $x = x^\mu = (ct, x, y, z)$ (with $x_\mu = (ct, -x, -y, -z)$), which spans the four-dimensional space-time of the universe.

To obtain the dynamics of these fields we find a suitable Lagrangian density, $\mathscr{L}$, which describes the interactions and the kinetic and potential energy involved in the system. The Lagrangian density

$$\mathscr{L} = \mathscr{L}(\phi_r(x), \phi_{r,\mu}(x)), \tag{1.1}$$

where

$$\phi_{r,\mu} \equiv \partial_\mu \phi_r \equiv \frac{\partial \phi_r}{\partial x^\mu}, \tag{1.2}$$

is hence a functional of the fields and their derivatives w.r.t. the space-time coordinates. We also define the momentum fields conjugate to $\phi_r(x)$ as

$$\pi_r(x) = \frac{\partial \mathscr{L}}{\partial \dot{\phi}_r(x)}. \tag{1.3}$$

The principle of stationary action can then be used on the action integral of the Lagrangian density, over a region in the four-dimensional configuration space, to find the equations of motion of the fields, also called the field equations.

In order to quantize the fields we let the spatial coordinates and their conjugate momenta go to operators:

$$\mathbf{x} \to \hat{\mathbf{x}}, \quad \mathbf{p} \to \hat{\mathbf{p}} = -\mathrm{i}\hbar\boldsymbol{\nabla}, \tag{1.4}$$

and impose the canonical commutation relations on them, which gives

$$\begin{aligned} [\phi_r(\mathbf{x},t), \pi_s(\mathbf{x}',t)] &= \mathrm{i}\hbar\delta_{rs}\delta(\mathbf{x}-\mathbf{x}') \\ [\phi_r(\mathbf{x},t), \phi_s(\mathbf{x}',t)] = [\pi_r(\mathbf{x},t), \pi_s(\mathbf{x}',t)] &= 0 \end{aligned}. \tag{1.5}$$

These are the equal-time commutation relations of the fields.

1.3 The Klein-Gordon field

This section is mainly based on chapter 3 and 5 in Ref. [12].

Bosons, i.e. integer spin particles, can be described by fields which satisfy the Klein-Gordon equation. This equation stems from the relation between the energy E, the rest mass m and the momentum $\mathbf{p}$ of relativistic particles:

$$E^2 = m^2c^4 + \mathbf{p}^2c^2. \tag{1.6}$$

If we replace E and $\mathbf{p}$ by their operator representations in quantum mechanics,

$$\mathbf{p} \to -\mathrm{i}\hbar\boldsymbol{\nabla}, \quad E \to \mathrm{i}\hbar\frac{\partial}{\partial t}, \tag{1.7}$$

and let the particles be represented by a real scalar field $\phi(x)$, we arrive at the Klein-Gordon equation for this field

$$\left[\Box + \left(\frac{mc}{\hbar}\right)^2\right]\phi(x) = 0, \tag{1.8}$$

where

$$\Box = \frac{1}{c^2}\frac{\partial^2}{\partial t^2} - \nabla^2 \tag{1.9}$$

and $\nabla^2 = \partial_\mu\partial^\mu$. The complete set of solutions of the Klein-Gordon equation for $\phi(x)$ can be expressed in terms of positive and negative energy solutions:

$$\phi(x) = \phi^+(x) + \phi^-(x). \tag{1.10}$$

However, this simple case applies only to single particle fields, which leads to difficulties because of negative probability densities for negative energy solutions. By instead considering a complex scalar field, we have two independent fields, ϕ and its complex conjugate $\phi^\dagger$. We can interpret this as dealing with two different particles, namely a type of particle and its antiparticle, where positive energy solutions correspond to particles and negative energy solutions to antiparticles. We then get a second Klein-Gordon equation for the complex conjugate field:

$$\left[\Box + \left(\frac{mc}{\hbar}\right)^2\right]\phi^\dagger(x) = 0. \tag{1.11}$$

At quantization both the real and complex fields satisfy the corresponding canonical commutation relations given in (1.5).

If we now consider the fields to span a finite three-dimensional volume V (which we later can let go to infinity in all directions), with fixed boundary conditions, we can Fourier expand the fields in terms of an infinite sum of waves with different frequencies $\omega_{\mathbf{k}}$ and corresponding wave vectors $\mathbf{k}$:

$$\phi(x) = \phi^+(x) + \phi^-(x) = \sum_{\mathbf{k}} \left(\frac{\hbar c^2}{2V\omega_{\mathbf{k}}} \right)^{1/2} [a(\mathbf{k})\mathrm{e}^{-\mathrm{i}kx} + b^\dagger(\mathbf{k})\mathrm{e}^{\mathrm{i}kx}], \tag{1.12}$$

$$\phi^\dagger(x) = \phi^{\dagger+}(x) + \phi^{\dagger-}(x) = \sum_{\mathbf{k}} \left(\frac{\hbar c^2}{2V\omega_{\mathbf{k}}} \right)^{1/2} [b(\mathbf{k})\mathrm{e}^{-\mathrm{i}kx} + a^\dagger(\mathbf{k})\mathrm{e}^{\mathrm{i}kx}]. \tag{1.13}$$

(The normalization factors are depentent on the choice of representation of the solutions.) We can then consider every point in space to be affected by a harmonic oscillator potential, where $a(\mathbf{k})$ and $a^\dagger(\mathbf{k})$, and $b(\mathbf{k})$ and $b^\dagger(\mathbf{k})$, can be interpreted as annihilation and creation operators of particles and antiparticles, respectively. These operators satisfy the following commutation relations:

$$\left[a(\mathbf{k}), a^\dagger(\mathbf{k}') \right] = \left[b(\mathbf{k}), b^\dagger(\mathbf{k}') \right] = \delta_{\mathbf{k}\mathbf{k}'}, \tag{1.14}$$

and all other commutators vanish. Quantizing the potentials and treating the coefficients in the Fourier expansion of the fields as operators, with the corresponding commutation relations, is often referred to as second quantization.

Complex scalar fields of this kind can be associated with electrically charged particles of spin-0, e.g. mesons like pions and kaons.

Spin-1 vector particles, like the photon, can also be described as quanta of fields that are solutions to the Klein-Gordon equation. In order to represent the photon in this way, we need to add a polarization vector $\varepsilon_r^\mu(\mathbf{k})$, where $r = 0, \ldots, 3$ denote the four possible polarization states of the photon (two transverse, one longitudinal and one scalar/time-like), and $\mu = 0, \ldots, 3$ denote the four components of the electromagnetic field $A^\mu(x)$, to which the photon is associated. The polarization vectors satisfy the orthonormality relation

$$\varepsilon_r(\mathbf{k})\varepsilon_s(\mathbf{k}) = \varepsilon_{r\mu}(\mathbf{k})\varepsilon_s^\mu(\mathbf{k}) = -\zeta_r \delta_{rs} \tag{1.15}$$

and the completeness relation

$$\sum_r \zeta_r \varepsilon_r^\mu(\mathbf{k})\varepsilon_r^\nu(\mathbf{k}) = -g^{\mu\nu}, \tag{1.16}$$

where $\zeta_0 = -1$ and $\zeta_1 = \zeta_2 = \zeta_3 = 1$.

Maxwell's equations can be written in covariant form using the electromagnetic field tensor $F^{\mu\nu}$, expressed in terms of the four-vector potential $A^\mu(x) = (\phi, \mathbf{A})$,

$$F^{\mu\nu}(x) = \partial^\nu A^\mu(x) - \partial^\mu A^\nu(x), \tag{1.17}$$

and the charge-current density $s^\mu(x) = (c\rho(x), \mathbf{j}(x))$, as

$$\Box A^\mu(x) - \partial^\mu[\partial_\nu A^\nu(x)] = \frac{1}{c} s^\mu(x). \tag{1.18}$$

In the free field case ($s^\mu(x) = 0$), using the Lorentz gauge ($\partial_\nu A^\nu(x) = 0$), the Klein-Gordon equation reduces to the massless wave equation

$$\Box A^\mu(x) = 0, \tag{1.19}$$

where the mass term disappears, which is consistent with the photon being massless. The electromagnetic field can then be expanded in terms of a complete set of solutions of the wave equation (1.19):

$$A^{\mu}(x) = A^{\mu+}(x) + A^{\mu-}(x), \tag{1.20}$$

where

$$A^{\mu+}(x) = \sum_{r\mathbf{k}} \left(\frac{\hbar c^2}{2V\omega_{\mathbf{k}}} \right)^{1/2} \varepsilon_r^{\mu}(\mathbf{k}) a(\mathbf{k}) \mathrm{e}^{-\mathrm{i}kx} \tag{1.21}$$

and

$$A^{\mu-}(x) = \sum_{r\mathbf{k}} \left(\frac{\hbar c^2}{2V\omega_{\mathbf{k}}} \right)^{1/2} \varepsilon_r^{\mu}(\mathbf{k}) a^{\dagger}(\mathbf{k}) \mathrm{e}^{\mathrm{i}kx}. \tag{1.22}$$

The Feynman photon propagator, $D_{\mathrm{F}}^{\mu\nu}(x - x')$, for a virtual photon appearing as an intermediate state in particle interactions, e.g. $q\bar{q} \to \gamma \to \mu^+\mu^-$, is given by

$$\langle 0|\mathbf{T}\left\{A^{\mu}(x)A^{\nu}(x')\right\}|0\rangle = \mathrm{i}\hbar c D_{\mathrm{F}}^{\mu\nu}, \tag{1.23}$$

where $\mathbf{T}$ denotes a time-ordered product of the fields in the curly parenthesis, and

$$D_{\mathrm{F}}^{\mu\nu}(x) = \frac{-g^{\mu\nu}}{(2\pi)^4} \int \frac{\mathrm{d}^4k\, \mathrm{e}^{-\mathrm{i}kx}}{k^2 + \mathrm{i}\varepsilon}, \tag{1.24}$$

where ε is a small positive number which is taken to go to zero after integration. $D_{\mathrm{F}}^{\mu\nu}(x)$ is related to the momentum space propagator $D_{\mathrm{F}}^{\mu\nu}(k)$ by

$$D_{\mathrm{F}}^{\mu\nu}(x) = \frac{1}{(2\pi)^4} \int \mathrm{d}^4k\, D_{\mathrm{F}}^{\mu\nu}(k) \mathrm{e}^{-\mathrm{i}kx}, \tag{1.25}$$

with

$$D_{\mathrm{F}}^{\mu\nu}(k) = \frac{-g^{\mu\nu}}{k^2 + \mathrm{i}\varepsilon}. \tag{1.26}$$

For massive vector bosons, such as the gauge bosons $W^{\pm}$ and Z of the electroweak theory, the Feynman propagator is given by

$$D_{\mathrm{F}}^{\mu\nu}(k, m) = \frac{-g^{\mu\nu} + k^{\mu}k^{\nu}/m^2}{k^2 - m^2 + \mathrm{i}\varepsilon}, \tag{1.27}$$

where m represents the mass of the boson in question. For the Higgs boson, the corresponding internal Feynman propagator is

$$D_{\mathrm{F}}^{\mu\nu}(k, m_H) = \frac{1}{k^2 - m_H^2 + \mathrm{i}\varepsilon}. \tag{1.28}$$

1.4 The Dirac field

The following section is mainly based on chapter 4 in Ref. [12]

Because of the problematic negative probability densities emerging from solutions of the Klein-Gordon equation, Dirac began to search for an alternative formulation of relativistic quantum mechanics. He suggested an expression consisting only of first order derivatives in space and time, on the form:

$$\hat{E}\psi(x) = (\boldsymbol{\alpha} \cdot \hat{\boldsymbol{p}}c + \beta m)\psi(x), \tag{1.29}$$

where $\boldsymbol{\alpha}$ and β were suitable quantities to be determined, and $\psi(x)$ is a wave function. In order to represent relativistic particles ψ must satisfy the Einstein energy-momentum relation (1.6), and thereby also the Klein-Gordon equation. This puts restrictions on $\boldsymbol{\alpha}$ and β, which in the simplest case require them to be 4×4 Hermitian matrices, for particles with non-zero mass. α and β can be expressed in terms of the γ-matrices

$$\gamma^0 = \beta, \quad \gamma^i = \beta\alpha_i, \quad i = 1, 2, 3, \tag{1.30}$$

which satisfy the anticommutation relations

$$\{\gamma^\mu, \gamma^\nu\} = 2g^{\mu\nu} \tag{1.31}$$

and the Hermiticity conditions $\gamma^{0\dagger} = \gamma^0$ and $\gamma^{i\dagger} = -\gamma^i$.

Writing out $\hat{E}$ and $\hat{\mathbf{p}}$ in terms of their operator representation, and $\boldsymbol{\alpha}$ and β in terms of the γ-matrices, the Dirac equation can be expressed as

$$\mathrm{i}\hbar\gamma^\mu \frac{\partial\psi(x)}{\partial x^\mu} - mc\psi(x) = 0, \tag{1.32}$$

where the wave function ψ has four components, because of the dimensions of the γ-matrices, and Eq. (1.32) has an implied sum over spinor indices and matrix elements for each of the four components of ψ, where ψ is known as a Dirac spinor,

$$\psi(x) = \begin{pmatrix} \psi_1(x) \\ \psi_2(x) \\ \psi_3(x) \\ \psi_4(x) \end{pmatrix}. \tag{1.33}$$

The adjoint field $\overline{\psi}(x)$, conveniently defined as

$$\overline{\psi}(x) = \psi^\dagger(x)\gamma^0, \tag{1.34}$$

satisfies the adjoint Dirac equation

$$\mathrm{i}\hbar\frac{\partial\overline{\psi}(x)}{\partial x^\mu}\gamma^\mu + mc\overline{\psi}(x) = 0. \tag{1.35}$$

It turns out that the four component Dirac field is suitable for describing particles and antiparticles of spin-1/2. This is due to its four corresponding degrees of freedom, which can be associated with components of spin up and spin down for both particle and antiparticle, hence the name spinor. The Dirac field therefore provides the appropriate field description of the material particles, namely the fermions, or in other words, particles that obey Fermi-Dirac statistics. In contrast to bosons, which obey Bose-Einstein statistics, where several identical

particles can occupy the same quantum state, the Pauli exclusion principle states that two identical fermions cannot occupy the same quantum state simultaneously.

In analogy with the Fourier expansion of the Klein-Gordon field, we can also quantize the Dirac field by expanding it in terms of the complete set of plane wave solutions of the Dirac equation, split in a positive and a negative energy part; now in terms of the three-momentum $\mathbf{p}$ and the corresponding energy $E_{\mathbf{p}}$ of the discrete momentum states:

$$\psi(x) = \psi^+(x) + \psi^-(x) = \sum_{r\mathbf{p}} \left(\frac{mc^2}{VE_{\mathbf{p}}}\right)^{1/2} [c_r(\mathbf{p})u_r(\mathbf{p})\mathrm{e}^{-\mathrm{i}px/\hbar} + d_r^\dagger(\mathbf{p})v_r(\mathbf{p})\mathrm{e}^{\mathrm{i}px/\hbar}], \tag{1.36}$$

and for the adjoint field:

$$\overline{\psi}(x) = \overline{\psi}^+(x) + \overline{\psi}^-(x) = \sum_{r\mathbf{p}} \left(\frac{mc^2}{VE_{\mathbf{p}}}\right)^{1/2} [d_r(\mathbf{p})\overline{v}_r(\mathbf{p})\mathrm{e}^{-\mathrm{i}px/\hbar} + c_r^\dagger(\mathbf{p})\overline{u}_r(\mathbf{p})\mathrm{e}^{\mathrm{i}px/\hbar}]. \tag{1.37}$$

Here $c_r(\mathbf{p})$ and $c_r^\dagger(\mathbf{p})$, and $d_r(\mathbf{p})$ and $d_r^\dagger(\mathbf{p})$, represent annihilation and creation operators for fermions and antifermions, respectively. $u_r(\mathbf{p})$ and $v_r(\mathbf{p})$, and their adjoints, make up the spinor parts of the states; where $r = 1, 2$ denotes the two possible spin polarizations. We can normalize the spinors so that

$$u_r^\dagger(\mathbf{p})u_r(\mathbf{p}) = v_r^\dagger(\mathbf{p})v_r(\mathbf{p}) = \frac{E_{\mathbf{p}}}{mc^2}, \tag{1.38}$$

and they will then satisfy the orthonormality relations

$$\begin{gathered} u_r^\dagger(\mathbf{p})u_s(\mathbf{p}) = v_r^\dagger(\mathbf{p})v_s(\mathbf{p}) = \frac{E_{\mathbf{p}}}{mc^2}\delta_{rs} \\ u_r^\dagger(\mathbf{p})v_s(-\mathbf{p}) = 0 \end{gathered}. \tag{1.39}$$

Instead of imposing the harmonic oscillator commutation relations on the creation and annihilation operators, as was done for the boson fields, we now impose *anti*commutation relations:

$$\{c_r(\mathbf{p}), c_s^\dagger(\mathbf{p}')\} = \{d_r(\mathbf{p}), d_s^\dagger(\mathbf{p}')\} = \delta_{rs}\delta_{\mathbf{pp}'}, \tag{1.40}$$

where all other anticommutators vanish. These anticommutators are chosen because they make the fermion fields behave according to the Pauli principle and Fermi-Dirac statistics.

1.5 Gauge theories

Chapter 11 in Ref. [12] has been used as base for this section.

In order to arrive to theoretical models which describe the interactions between the particle fields, there are some conditions that the theory needs to fulfill. We want it to be Lorentz invariant and expressed in a covariant way. This means that the mathematical expressions involved have to be invariant under Lorentz transformations in special relativity, and maintain the same mathematical form in all reference frames. We want the theory to be local, which means that all fields and quantities that appear in interaction Lagrangian densities are evaluated at the same space-time point x^μ. To avoid infinities when calculating radiative corrections, we also require that the theory be renormalizable. This involves regularization of integrals over four-momenta, in terms of convergence factors, so that the integral is well-defined and convergent for all four-momenta. The expressions are then written in terms of the physical and observable attributes (e.g. charge and mass) of the interacting particles, instead of the corresponding

"bare" attributes of the uninteracting and unobservable particles. In this way the divergences are incorporated into the unobservable relationship between the physical and "bare" quantities, and the original theory is restored, i.e. the theory is renormalized.

We also want the Lagrangian densities, that describe the fields and interactions, to be gauge invariant, i.e. be invariant under so-called gauge transformations. The gauge principle will be demonstrated through the case of Quantum electrodynamics (QED), which represents the simplest form of a gauge theory.

Before continuing I will just make a small remark on the practice of units. It is common to use natural units when working with relativistic quantum field theory, where one expresses quantities in units of action ($\hbar$), velocity (c) and energy (MeV). Both $\hbar$ and c occur often in the mathematical expressions, so, in addition, setting $\hbar = c = 1$, provides a convenient simplification. I will use this convention in the rest of this chapter.

1.5.1 Quantum electrodynamics (QED)

The free field Lagrangian density, from which the Dirac equations (1.32) and (1.34) can be derived,

$$\mathscr{L}_0 = \overline{\psi}(x)\left[\mathrm{i}\gamma^\mu \frac{\partial}{\partial x^\mu} - m\right]\psi(x), \tag{1.41}$$

remains unchanged, i.e. is invariant, under a set of global phase transformations of the fields (transformations not dependant on x):

$$\begin{aligned} \psi(x) &\to \psi'(x) = \psi(x)\mathrm{e}^{-\mathrm{i}\alpha} \\ \overline{\psi}(x) &\to \overline{\psi}'(x) = \overline{\psi}(x)\mathrm{e}^{\mathrm{i}\alpha} \end{aligned}, \tag{1.42}$$

where α is an arbitrary real constant. Since the Dirac fields represent particles with electric charge, this invariance of the Lagrangian density, under a global phase transformation of the free fields, implies conservation of the electric charge current density

$$s^\mu(x) = q\overline{\psi}(x)\gamma^\mu\psi(x) \tag{1.43}$$

and the total electric charge

$$Q = q\int \mathrm{d}^3\mathbf{x}\psi^\dagger(x)\psi(x), \tag{1.44}$$

in accordance with Noether's theorem.

However, when looking at field interactions we do not need to consider global phase transformations, but are merely interested in local phase transformations since we are working with a local theory. The Dirac fields will then transform locally as

$$\begin{aligned} \psi(x) &\to \psi'(x) = \psi(x)\mathrm{e}^{-\mathrm{i}qf(x)} \\ \overline{\psi}(x) &\to \overline{\psi}'(x) = \overline{\psi}(x)\mathrm{e}^{\mathrm{i}qf(x)} \end{aligned}, \tag{1.45}$$

where q is a real constant, which in this case represents the electric charge and coupling constant of QED, and $f(x)$ is a real differentiable function. If the local phase transformations of (1.45) are performed on the fields in the free-fermion Lagrangian density, Eq. (1.41), by use of Taylor-expansion for infinitesimal $f(x)$, $\mathscr{L}_0$ transforms as

$$\mathscr{L}_0 \to \mathscr{L}_0' = \mathscr{L}_0 + q\overline{\psi}(x)\gamma^\mu\psi(x)\partial_\mu f(x), \tag{1.46}$$

and consequently $\mathscr{L}_0$ is not invariant under this transformation. In order to restore the invariance of the Lagrangian density, we introduce a new term, called the interaction term, through the minimal substitution,

$$\partial_\mu \to D_\mu = \partial_\mu + \mathrm{i}qA_\mu(x), \tag{1.47}$$

where the ordinary derivative ∂_μ is being replaced by the "covariant derivative" D_μ, and the new "gauge field" A_μ is required to transform as

$$A_\mu(x) \to A'_\mu(x) = A_\mu(x) + \partial_\mu f(x). \tag{1.48}$$

Under the coupled transformations (1.45) and (1.48) the covariant derivative of the "matter field" $D_\mu\psi(x)$ transforms in the same way as the field $\psi(x)$ itself,

$$D_\mu\psi(x) \to \mathrm{e}^{-\mathrm{i}qf(x)} D_\mu\psi(x). \tag{1.49}$$

The total Lagrangian density for the fermion fields

$$\mathscr{L} = \mathscr{L}_0 + \mathscr{L}_\mathrm{I} = \overline{\psi}(x)[\mathrm{i}\gamma^\mu D_\mu - m]\psi(x), \tag{1.50}$$

where

$$\mathscr{L}_\mathrm{I} = -q\overline{\psi}(x)\gamma^\mu\psi(x)A_\mu(x) \tag{1.51}$$

is the interaction term, is then invariant under the gauge transformations (1.45) and (1.48), and hence is called gauge invariant. So by adding an extra term, containing a gauge field which transforms in a way that makes the Lagrangian density gauge invariant, we have obtained the QED interaction between the matter field of the fermions and the gauge field of the photon.

The free-photon Lagrangian density can be expressed as

$$\mathscr{L}^\mathrm{photon} = -\frac{1}{4}F_{\mu\nu}(x)F^{\mu\nu}(x), \tag{1.52}$$

where $F^{\mu\nu}$ is the electromagnetic field tensor.

Since the gauge transformations in QED are unitary scalar operations, where probability amplitudes are unaffected by the transformations, we associate QED with a U(1) gauge group.

One way to obtain the probability for a specific interaction/process to happen, is through the so-called S-matrix expansion. The matrix element $\langle f|S|i\rangle$ corresponds to the transition probability amplitude for an initial state $|i\rangle$ to produce a final state $|f\rangle$, in a given order of perturbation theory. This transition amplitude is proportional to the so-called Feynman amplitude $\mathscr{M}$, which contains the fundamental physics of the specific interaction. The Feynman amplitude is obtained by applying the Feynman rules belonging to the interaction in question. This can, very conveniently, be carried out by first drawing a Feynman diagram of the process, and then construct the mathematical expression of the amplitude from the Feynman rules of the elements involved in the diagram. The three basic elements of the matrix element are the spinors (and polarization states) of the incoming and outgoing particles, the propagator of an intermediate particle and a vertex factor for each interaction vertex.

The basic QED vertex is shown in Fig. 1.2, and has the form $\overline{u}^f_s(\mathbf{p}^f)[\mathrm{i}e\gamma^\alpha]u^f_r(\mathbf{p}^i)$, where u denotes a spinor, i (f) the initial (final) state particle, r (s) the spin state of the initial (final) state particle (e.g. up or down), and $\mathrm{i}e\gamma^\alpha$ the vertex factor of the QED interaction.

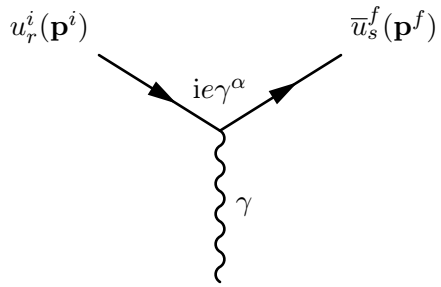

Figure 1.2: Feynman diagram of the basic QED vertex, of an initial and a final state fermion interacting with a photon.

1.5.2 Quantum chromodynamics (QCD)

Whereas the electromagnetic fields describe particles/antiparticles with electric charge $\pm e$, the strong interaction deals with particles/antiparticles with three color charges $r/\bar{r}$, $g/\bar{g}$ and $b/\bar{b}$, with a separate field for each color charge. So, each quark flavor $f = u, d, s, c, b, t$, results in three fields, which we for convenience place in a three component field

$$\Psi^f(x) = \begin{pmatrix} \psi_r^f(x) \\ \psi_g^f(x) \\ \psi_b^f(x) \end{pmatrix}, \tag{1.53}$$

with the corresponding adjoint field

$$\overline{\Psi}^f(x) = \left(\overline{\psi}_r^f(x), \overline{\psi}_g^f(x), \overline{\psi}_b^f(x)\right). \tag{1.54}$$

The free-field Lagrangian density for the quark fields is then

$$\mathscr{L}_0 = \overline{\Psi}^f(x)[\mathrm{i}\partial\!\!\!/ - m_f]\Psi^f(x), \tag{1.55}$$

where $\partial\!\!\!/ \equiv \gamma^\mu \partial_\mu$. It is invariant under the global phase transformations ($j = 1, 2, \ldots, 8$)

$$\begin{aligned} \Psi^f(x) &\to \Psi^{f\prime}(x) = U(\alpha)\Psi^f(x) \equiv \mathrm{e}^{\mathrm{i}\alpha_j\lambda_j/2}\Psi^f(x) \\ \overline{\Psi}^f(x) &\to \overline{\Psi}^{f\prime}(x) = \overline{\Psi}^f(x)U^\dagger(\alpha) \equiv \overline{\Psi}^f(x)\mathrm{e}^{-\mathrm{i}\alpha_j\lambda_j/2}, \end{aligned} \tag{1.56}$$

where λ_j represent eight linearly independent Hermitian 3×3 matrices, and α_i are eight arbitrary real numbers with $\alpha \equiv (\alpha_1, \alpha_2, \ldots, \alpha_8)$. In terms of group theory the operators $U(\alpha)$ represent the group of 3×3 unitary matrices with the "special" property that $\det(U(\alpha)) = +1$. Hence they perform so-called SU(3) group transformations, where the λ_j-matrices act as generators of the group. Since the free field Lagrangian density is invariant under these global three-dimensional phase transformations, it can be shown that there are eight conserved current densities

$$S_i^\mu(x) = \frac{1}{2}\overline{\Psi}^f(x)\gamma^\mu\lambda_i\Psi^f(x), \tag{1.57}$$

corresponding to exchange of the eight different gluon states with distinct color combinations, through which the eight color charges

$$\hat{F}_i \equiv \int \mathrm{d}^3\mathbf{x} S_i^0(x) = \frac{1}{2}\int \mathrm{d}^3\mathbf{x}\Psi^{f\dagger}(x)\lambda_i\Psi^f(x) \tag{1.58}$$

are conserved.

Generalizing from global to local phase transformations, we now get

$$\begin{aligned}\Psi^f(x) &\to \Psi^{f\prime}(x) = \mathrm{e}^{\mathrm{i}g_s\lambda_j\omega_j(x)/2}\Psi^f(x)\\ \overline{\Psi}^f(x) &\to \overline{\Psi}^{f\prime}(x) = \overline{\Psi}^f(x)\mathrm{e}^{-\mathrm{i}g_s\lambda_j\omega_j(x)/2},\end{aligned} \tag{1.59}$$

where $\omega_j(x)$ are eight arbitrary real differentiable functions, and g_s is the coupling constant of the strong interaction. The Lagrangian density in Eq. (1.55) is not invariant under these local transformations, so we again use the same approach as for QED and replace the ordinary derivative with a covariant derivative

$$\partial^\mu \to D^\mu = \partial^\mu + \mathrm{i}g_s\lambda_j A_j^\mu(x)/2, \tag{1.60}$$

where A_j^μ are eight real gauge fields, each associated with a gluon state. It can be shown that for the resulting Lagrangian density to be gauge invariant, the gauge fields have to transform as

$$A_i^\mu(x) \to A_i^{\mu\prime}(x) \equiv A_i^\mu(x) - \partial^\mu\omega_i(x) - g_s f_{ijk}\omega_j(x)A_k^\mu(x), \tag{1.61}$$

where f_{ijk} are totally antisymmetric structure constants related to the commutation relations of the color operators $\hat{F}_i$.

The full gauge invariant Lagrangian density of the quarks and their interaction with gluons can now be expressed as

$$\mathscr{L}^q(x) = \mathscr{L}_0 + \mathscr{L}_\mathrm{I} = \overline{\Psi}^f(x)[\mathrm{i}\not{D} - m_f]\Psi(x), \tag{1.62}$$

with the interaction term being

$$\mathscr{L}_\mathrm{I} = -\frac{1}{2}g_s\overline{\Psi}^f(x)\gamma_\mu\lambda_j\Psi^f(x)A_j^\mu(x). \tag{1.63}$$

The gluon Lagrangian density can be written as

$$\mathscr{L}^\mathrm{gluon} = -\frac{1}{4}G_{i\mu\nu}(x)G_i^{\mu\nu}(x) \tag{1.64}$$

$$\begin{aligned}&= -\frac{1}{4}F_{i\mu\nu}(x)F_i^{\mu\nu}(x) + g_s f_{ijk}A_{i_\mu}(x)A_{j\nu}(x)\partial^\mu A_k^\nu(x)\\ &\quad - \frac{1}{4}g_s^2 f_{ijk}f_{ilm}A_j^\mu(x)A_k^\nu(x)A_{l\mu}(x)A_{m\nu}(x)\end{aligned} \tag{1.65}$$

where

$$F_i^{\mu\nu}(x) = \partial^\nu A_i^\mu(x) - \partial^\mu A_i^\nu(x) \tag{1.66}$$

is the gluon field analog of the electromagnetic field tensor, with A_i^μ being the gluon fields, and with

$$G_i^{\mu\nu} \equiv F_i^{\mu\nu}(x) + g_s f_{ijk}A_j^\mu(x)A_k^\nu(x). \tag{1.67}$$

The first term in Eq. (1.65) is the free gluon field part, similar to the Lagrangian density of the photon in QED. But in contrast to the photon, the gluons have self-interaction terms, apparent in the second and third term, representing three- and four-point gluon interaction vertices, respectively. Fig. 1.3 shows the basic QCD vertices.

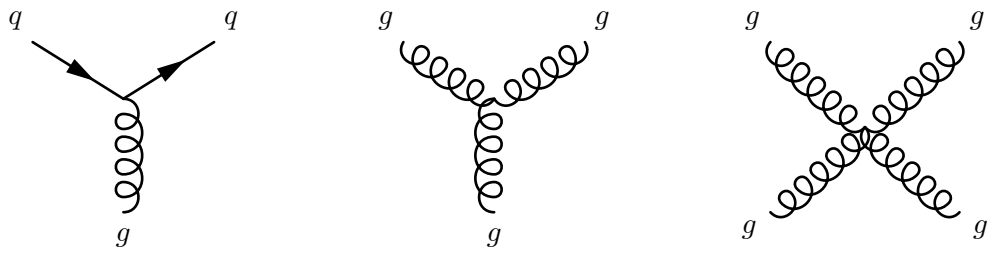

(a) (b) (c)

Figure 1.3: Feynman diagrams of the basic QCD vertices, showing (a) quark interaction with a gluon, (b) three-point and (c) four-point self-interactions of gluons.

1.5.3 Electroweak theory

This part, concerning the electroweak gauge theory, is mainly based on chapter 17 in Ref. [12].

Experiments have shown that the only charged leptonic currents involved in the weak interaction are of the form

$$J_\alpha(x) = \sum_l \overline{\psi}_l(x)\gamma_\alpha(1-\gamma_5)\psi_{\nu_l}(x) \tag{1.68}$$

and

$$J^\dagger_\alpha(x) = \sum_l \overline{\psi}_{\nu_l}(x)\gamma_\alpha(1-\gamma_5)\psi_l(x), \tag{1.69}$$

where ψ_l and ψ_{ν_l} denote the quantized fields of the charged leptons $l = e, \mu, \tau$ and of the corresponding neutrinos, respectively, and γ_5 is a 4×4 matrix which satisfies the anticommutation relation $\{\gamma^\mu, \gamma_5\} = 0$. Hence, we can express the weak leptonic current (1.68) as

$$J^\alpha(x) = J^\alpha_{\mathrm{V}}(x) - J^\alpha_{\mathrm{A}}(x), \tag{1.70}$$

in terms of a vector current

$$J^\alpha_{\mathrm{V}}(x) = \sum_l \overline{\psi}_l(x)\gamma^\alpha\psi_{\nu_l}(x) \tag{1.71}$$

and an axial vector current

$$J^\alpha_{\mathrm{A}}(x) = \sum_l \overline{\psi}_l(x)\gamma^\alpha\gamma_5\psi_{\nu_l}(x). \tag{1.72}$$

Whereas the vector current part will change sign under a space inversion, the axial current part will not, and therefore the weak interaction does not conserve parity, in contrast to the electromagnetic and strong interactions.

One can show that for massless particles with a spinor component w_r, the γ_5 matrix acts as the spin projection operator $\sigma_{\mathbf{p}}$,

$$\gamma_5 w_r(\mathbf{p}) = \sigma_{\mathbf{p}} w_r(\mathbf{p}), \tag{1.73}$$

where

$$\sigma_{\mathbf{p}} = \frac{\boldsymbol{\sigma}\cdot\mathbf{p}}{|\mathbf{p}|}, \tag{1.74}$$

and $\boldsymbol{\sigma}$ are 4×4 matrices built from the 2×2 Pauli matrices. We can then define helicity projection operators

$$P_{\mathrm{L}} = \frac{1}{2}(1 - \gamma_5), \quad P_{\mathrm{R}} = \frac{1}{2}(1 + \gamma_5), \tag{1.75}$$

that project out left- and right-handed helicity states, namely states with third component of spin anti-parallel and parallel to the direction of linear momentum, respectively. With these definitions, we see that the leptonic current (1.68) can be expressed as

$$J_\alpha(x) = 2 \sum_l \overline{\psi}_l^{\mathrm{L}}(x) \gamma_\alpha \psi_{\nu_l}^{\mathrm{L}}(x), \tag{1.76}$$

with only contributions from left-handed helicity states to the weak interaction of leptons. The same applies to the weak interactions between quarks. For massless particles the helicity eigenstates are also chiral eigenstates (eigenstates of γ_5), while massive particles can be regarded as approximate chiral eigenstates only in the ultra relativistic limit where $E \gg m$.

The different treatment of left- and right-handed helicity states in the weak interactions makes it convenient to collect the left-handed states in a doublet

$$\Psi_l^{\mathrm{L}}(x) = \begin{pmatrix} \psi_{\nu_l}^{\mathrm{L}}(x) \\ \psi_l^{\mathrm{L}}(x) \end{pmatrix}, \tag{1.77}$$

called a weak isospin doublet because of its similarity with the isospin symmetry of the strong interaction, while the right-handed fields are singlet states. The free-lepton Lagrangian density can then be expressed as

$$\mathscr{L}_0 = \mathrm{i} \left[\overline{\Psi}_l^{\mathrm{L}}(x) \partial\!\!\!/ \Psi_l^{\mathrm{L}}(x) + \overline{\psi}_l^{\mathrm{R}}(x) \partial\!\!\!/ \psi_l^{\mathrm{R}}(x) + \overline{\psi}_{\nu_l}^{\mathrm{R}}(x) \partial\!\!\!/ \psi_{\nu_l}^{\mathrm{R}}(x) \right]. \tag{1.78}$$

By performing global SU(2) transformations on this Lagrangian density, with

$$U(\alpha) \equiv \mathrm{e}^{\mathrm{i}\alpha_j \tau_j / 2}, \tag{1.79}$$

where $\alpha \equiv (\alpha_1, \alpha_2, \alpha_3)$ are three arbitrary real numbers and the three group generators τ_j, $j = 1, 2, 3$, satisfying the commutation relations $[\tau_i, \tau_j] = 2\mathrm{i}\varepsilon_{ijk}\tau_k$, the left-handed fields will transform as

$$\begin{aligned} \Psi_l^{\mathrm{L}}(x) &\to \Psi_l^{\mathrm{L}\prime}(x) = \mathrm{e}^{\mathrm{i}\alpha_j \tau_j / 2} \Psi_l^{\mathrm{L}}(x) \\ \overline{\Psi}_l^{\mathrm{L}}(x) &\to \overline{\Psi}_l^{\mathrm{L}\prime}(x) = \overline{\Psi}_l^{\mathrm{L}}(x) \mathrm{e}^{-\mathrm{i}\alpha_j \tau_j / 2} \end{aligned}, \tag{1.80}$$

while the right-handed fields are left unaffected. The Lagrangian density (1.78) is invariant under these transformations, which leads to three conserved weak isospin currents

$$J_i^\alpha(x) = \frac{1}{2} \overline{\Psi}_l^{\mathrm{L}}(x) \gamma^\alpha \tau_i \Psi_l^{\mathrm{L}}(x), \tag{1.81}$$

along with the three corresponding weak isospin charges

$$I_i^{\mathrm{W}} = \int \mathrm{d}^3\mathbf{x} J_i^0(x) = \frac{1}{2} \int \mathrm{d}^3\mathbf{x} \Psi_l^{\mathrm{L}\dagger}(x) \tau_i \Psi_l^{\mathrm{L}}(x). \tag{1.82}$$

The previously formulated charged currents J_α and $J_\alpha^\dagger$ can now be written as a linear combination of the two weak isospin currents J_1 and J_2:

$$\begin{aligned} J^\alpha(x) &= 2[J_1^\alpha(x) - \mathrm{i}J_2^\alpha(x)] = \overline{\psi}_l(x) \gamma^\alpha (1 - \gamma_5) \psi_{\nu_l}(x) \\ J^{\alpha\dagger}(x) &= 2[J_1^\alpha(x) + \mathrm{i}J_2^\alpha(x)] = \overline{\psi}_{\nu_l}(x) \gamma^\alpha (1 - \gamma_5) \psi_l(x) \end{aligned}, \tag{1.83}$$

with the third conserved current being a neutral current

$$J_3^\alpha(x) = -\frac{1}{2}\overline{\Psi}_l^{\mathrm{L}}(x)\gamma^\alpha\tau_3\Psi_l^{\mathrm{L}}(x) = \frac{1}{2}\left[\overline{\psi}_{\nu_l}^{\mathrm{L}}(x)\gamma^\alpha\psi_{\nu_l}^{\mathrm{L}}(x) - \overline{\psi}_l^{\mathrm{L}}(x)\gamma^\alpha\psi_l^{\mathrm{L}}(x)\right]. \tag{1.84}$$

The free-field Lagrangian density of Eq. (1.78) is also invariant under U(1) global phase transformations performed by the operator

$$U \equiv \mathrm{e}^{\mathrm{i}\beta\mathrm{Y}}, \tag{1.85}$$

with β being a real number and Y being the weak hypercharge operator $Y = Q/e - I_3^{\mathrm{W}}$ (e is the electron charge), also reminiscent of the concept of hypercharge in the strong interaction. The invariance of the Lagrangian density under such transformations leads to conservation of the weak hypercharge current

$$J_Y^\alpha(x) = s^\alpha(x)/e - J_3^\alpha(x) = -\frac{1}{2}\overline{\Psi}_l^{\mathrm{L}}(x)\gamma^\alpha\Psi_l^{\mathrm{L}}(x) - \overline{\psi}_l^{\mathrm{R}}(x)\gamma^\alpha\psi_l^{\mathrm{R}}(x), \tag{1.86}$$

and the corresponding weak hypercharge

$$Y = \int \mathrm{d}^3\mathbf{x}J_Y^0(x). \tag{1.87}$$

By generalizing the transformations to local phase transformations, introducing new gauge fields and substituting the partial derivatives with suitable covariant derivatives, the leptonic Lagrangian density can now be written as

$$\mathscr{L}^{\mathrm{leptons}} = \mathrm{i}\left[\overline{\Psi}_l^{\mathrm{L}}(x)\not{D}\Psi_l^{\mathrm{L}}(x) + \overline{\psi}_l^{\mathrm{R}}(x)\not{D}\psi_l^{\mathrm{R}}(x) + \overline{\psi}_{\nu_l}^{\mathrm{R}}(x)\not{D}\psi_{\nu_l}^{\mathrm{R}}(x)\right], \tag{1.88}$$

where

$$D^\mu\Psi_l^{\mathrm{R}}(x) = \left[\partial^\mu + \mathrm{i}g\tau_j W_j^\mu(x)/2 - \mathrm{i}g'B^\mu(x)/2\right]\Psi_l^{\mathrm{L}}(x) \tag{1.89}$$

$$D^\mu\psi_l^{\mathrm{R}}(x) = \left[\partial^\mu - \mathrm{i}g'B^\mu(x)\right]\psi_l^{\mathrm{R}}(x) \tag{1.90}$$

$$D^\mu\psi_{\nu_l}^{\mathrm{R}}(x) = \partial^\mu\psi_{\nu_l}^{\mathrm{R}}(x). \tag{1.91}$$

Here, the gauge invariant SU(2) transformations have introduced three new gauge fields W_i^μ along with a coupling constant g, and the gauge invariant U(1) transformations have also brought along a new gauge field B^μ together with a coupling constant g'. The leptonic Lagrangian density consists of a free-lepton part $\mathscr{L}_0$ and an interaction part $\mathscr{L}_{\mathrm{I}}$, where the latter,

$$\mathscr{L}_{\mathrm{I}} = -gJ_i^\mu(x)W_{i\mu}(x) - g'J_Y^\mu(x)B_\mu(x), \tag{1.92}$$

is containing the three weak isospin currents with their associated gauge boson interactions, and the last term being the weak hypercharge current with its associated interaction with the B_μ gauge field.

In the same manner as we expressed the charged currents J_α and $J_\alpha^\dagger$ as linear combinations of the $J_{1\alpha}$ and $J_{2\alpha}$ currents, we can now make linear combinations of the $W_{1\mu}$ and $W_{2\mu}$ fields to express charged W_μ and $W_\mu^\dagger$ fields:

$$\begin{aligned} W_\mu(x) &= \frac{1}{\sqrt{2}}[W_{i\mu}(x) - \mathrm{i}W_{2\mu}(x)] \\ W_\mu^\dagger(x) &= \frac{1}{\sqrt{2}}[W_{i\mu}(x) + \mathrm{i}W_{2\mu}(x)] \end{aligned}. \tag{1.93}$$

(a) (b)

Figure 1.4: Examples of the basic (a) neutral and (b) charged current vertices of the electroweak interactions.

These are the fields that represent the $W^\pm$ gauge bosons in the Standard Model.

We can also express the $W_{3\mu}$ and B_μ fields as linear combinations of two other gauge fields Z_μ and A_μ:

$$\begin{aligned} W_{3\mu}(x) &= \cos\theta_{\mathrm{W}} Z_\mu(x) + \sin\theta_{\mathrm{W}} A_\mu(x) \\ B_\mu(x) &= -\sin\theta_{\mathrm{W}} Z_\mu(x) + \cos\theta_{\mathrm{W}} A_\mu(x) \end{aligned}, \tag{1.94}$$

with θ_{W} known as the weak mixing angle. By demanding that A_μ is the electromagnetic field, we obtain the following relation:

$$g\sin\theta_{\mathrm{W}} = g'\cos\theta_{\mathrm{W}} = e. \tag{1.95}$$

So, interpreting A_μ as the photon field and Z_μ as the field associated to the gauge boson Z^0, the interaction Lagrangian density can then be expressed on the form

$$\begin{aligned} \mathscr{L}_{\mathrm{I}} = &- s^\mu(x) A_\mu(x) - \frac{g}{2\sqrt{2}}\left[J^{\mu\dagger}(x) W_\mu(x) + J^\mu(x) W_\mu^\dagger(x)\right] \\ &- \frac{g}{\cos\theta_{\mathrm{W}}}\left[J_3^\mu(x) - \sin^2\theta_{\mathrm{W}} s^\mu(x)/e\right] Z_\mu(x). \end{aligned} \tag{1.96}$$

The first term in Eq. (1.96) corresponds to the current of the electromagnetic interaction, while the second and the last term represent the charged and neutral currents of the weak/electroweak interaction, respectively. Since the weak mixing angle θ_{W} is non-zero, we therefore get a unified theory of the electromagnetic and weak interactions, where the Lagrangian density (1.96) is said to be $\mathrm{SU(2)_L}\times\mathrm{U(1)}_Y$ gauge invariant.

The Lagrangian density of the non-interacting and self-interacting gauge bosons in the electroweak theory can be represented by

$$\begin{aligned} \mathscr{L}^{\mathrm{EWbosons}} = &- \frac{1}{4} B_{\mu\nu}(x) B^{\mu\nu}(x) - \frac{1}{4} F_{i\mu\nu}(x) F_i^{\mu\nu}(x) \\ &+ g\varepsilon_{ijk} W_{i\mu}(x) W_{j\nu}(x) \partial^\mu W_k^\nu(x) \\ &- \frac{1}{4} g^2 \varepsilon_{ijk}\varepsilon_{ilm} W_j^\mu(x) W_k^\nu(x) W_{l\nu}(x) W_{m\nu}(x) \end{aligned}, \tag{1.97}$$

where $B^{\mu\nu}$ represents the non-interacting part of the A^μ, Z^μ and W^μ gauge fields, and

$$F_i^{\mu\nu}(x) \equiv \partial^\nu W_i^\mu(x) - \partial^\mu W_i^\nu(x) \tag{1.98}$$

are the three electromagnetic field tensor analogs of the three W_i^μ fields. We also in (1.97), like for the gluons in the strong interaction, see that in addition to the free-field part there are three- and four-point interaction terms which describe various interactions between the four electroweak

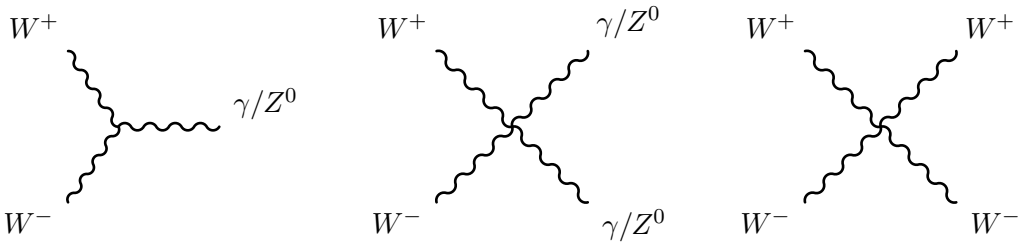

Figure 1.5: Feynman diagrams of the self-interactions of the electroweak gauge bosons.

gauge bosons themselves. These are on the form $W^\dagger WZ$, $W^\dagger WA$, $W^\dagger WZ^2$, $W^\dagger WA^2$, $W^\dagger WAZ$ and $(W^\dagger W)^2$, and are shown in Fig. 1.5. In contrast with QCD, there are some self-interaction constructs of the electroweak gauge bosons which are not allowed, due to the gauge structure of the electroweak interactions. Self-interactions which are not allowed, include A^3, AZ^2, Z^3, A^2Z^2, A^4 and Z^4.

1.6 The Brout-Englert-Higgs mechanism

This section is mostly based on chapter 18 in Ref. [12].

So far, the theory reviewed has treated all particles as massless, because simply inserting mass terms in the Lagrangian density will destroy the gauge invariance. The way to obtain the necessary mass terms for the massive particles is through the Brout-Englert-Higgs mechanism, which is based on the concept of spontaneous symmetry breaking. The idea is that the vacuum is filled by some complex scalar field, called the Higgs field, with a symmetric potential, but where the ground state is degenerate with a non-zero expectation value. At some point in time, when the universe was cooling down, the physical vacuum spontaneously broke the symmetry by "choosing" one of the infinitely many ground states available, and thereby giving particles their mass, related to how strongly they interact with the vacuum expectation value of this Higgs field.

To break the $\mathrm{SU(2)_L}$ symmetry the Higgs field must be a two component field

$$\Phi(x) = \begin{pmatrix} \phi_a(x) \\ \phi_b(x) \end{pmatrix}, \tag{1.99}$$

where ϕ_a and ϕ_b are scalar fields placed in the weak isospin doublet Φ. Under $\mathrm{SU(2)_L}\times\mathrm{U(1)}_Y$ gauge transformations Φ will transform in the same way as the weak isospin doublet Ψ_l^{L}. We also introduce the free Higgs field Lagrangian density

$$\mathscr{L}^{\mathrm{H}}(x) = [D^\mu\Phi(x)]^\dagger[D_\mu\Phi(x)] - \mu^2\Phi^\dagger(x)\Phi(x) - \lambda[\Phi^\dagger(x)\Phi(x)]^2, \tag{1.100}$$

where the covariant derivative is defined to be

$$D^\mu\Phi(x) = \left[\partial^\mu + \mathrm{i}g\tau_j W_j^\mu(x)/2 + \mathrm{i}g'YB^\mu(x)\right]\Phi(x) \tag{1.101}$$

and

$$\mathscr{V}(\Phi) = \mu^2\Phi^\dagger(x)\Phi(x) + \lambda[\Phi^\dagger(x)\Phi(x)]^2 \tag{1.102}$$

is the potential of the Higgs field, often called the "Mexican hat potential" or the "wine bottle potential" due to its shape. In (1.102) we need to have $\lambda > 0$ in order to get finite minima, and

$\mu^2 < 0$ to obtain the degenerate ground state, making a circle about the origin in the complex plane, with the radius squared being

$$\Phi_0^\dagger \Phi_0 = |\phi_a^0|^2 + |\phi_b^0|^2 = \frac{-\mu^2}{2\lambda}. \tag{1.103}$$

We can choose the ground state Φ_0 to be

$$\Phi_0 = \begin{pmatrix} \phi_a^0 \\ \phi_b^0 \end{pmatrix} = \begin{pmatrix} 0 \\ v/\sqrt{2} \end{pmatrix}, \tag{1.104}$$

where

$$v = \sqrt{\frac{-\mu^2}{\lambda}} \quad (> 0), \tag{1.105}$$

and all other ground states are related to this particular one by a phase transformation.

The ground state of the Higgs field is in general not invariant under combined $\mathrm{SU(2)_L}\times\mathrm{U(1)}_Y$ gauge transformations, but we need it to be invariant under U(1) gauge transformations in order to ensure that the photon stays massless and that electric charge is conserved. By assigning to the Higgs field a weak hypercharge value of $Y = \frac{1}{2}$, the lower component in the doublet, ϕ_b, will be electrically neutral. Thus, the spontaneous symmetry breaking will only occur in the electrically neutral component of the Higgs field, and electric charge is hence conserved.

It is useful to parametrize the Higgs field Φ in terms of its deviation from the vacuum field Φ_0:

$$\Phi(x) = \frac{1}{\sqrt{2}} \begin{pmatrix} \eta_1(x) + \mathrm{i}\eta_2(x) \\ v + \sigma(x) + \mathrm{i}\eta_3(x) \end{pmatrix}. \tag{1.106}$$

The η_i fields ($i = 1, 2, 3$) correspond to unphysical massless scalar fields, which give rise to so called Goldstone bosons. We want to get rid of these unphysical fields, and in the so-called unitary gauge these fields are transformed away, giving

$$\Phi(x) = \frac{1}{\sqrt{2}} \begin{pmatrix} 0 \\ v + \sigma(x) \end{pmatrix}. \tag{1.107}$$

In the standard electroweak theory the three degrees of freedom of the η_i fields, each field having one, will in the unitary gauge be transferred into giving the electroweak gauge bosons $W^\pm$ and Z^0 longitudinal polarization states, which is what gives them their respective masses, while the σ field will on quantization give rise to massive scalar Higgs bosons.

In order to obtain the lepton masses we need to add an additional term to the electroweak Lagrangian density:

$$\begin{aligned} \mathscr{L}^{\mathrm{H,leptons}}(x) = &- g_l \left[\Psi_l^{\mathrm{L}}(x) \psi_l^{\mathrm{R}}(x) \Phi(x) + \Phi^\dagger(x) \overline{\psi}_l^{\mathrm{R}}(x) \Psi_l^{\mathrm{L}}(x) \right] \\ &- g_{\nu_l} \left[\Psi_l^{\mathrm{L}}(x) \psi_{\nu_l}^{\mathrm{R}}(x) \widetilde{\Phi}(x) + \widetilde{\Phi}^\dagger(x) \overline{\psi}_l^{\mathrm{R}}(x) \Psi_{\nu_l}^{\mathrm{L}}(x) \right], \end{aligned} \tag{1.108}$$

where g_l and g_{ν_l} are dimensionless coupling constants for leptons and neutrinos, respectively, and

$$\widetilde{\Phi}(x) = -\mathrm{i}[\Phi^\dagger(x)\tau_2]^{\mathrm{T}} = \begin{pmatrix} \phi_b^*(x) \\ -\phi_a^*(x) \end{pmatrix} \tag{1.109}$$

with τ_2 being the second Pauli matrix. The Higgs and lepton fields here couple through Yukawa interactions (spinors coupling to scalar field). These couplings will be proportional to the mass

of the lepton in question. And so, the masses of the leptons are determined by how strongly they couple to the Higgs field.

The second term in (1.108) does account for neutrinos with non-zero masses, but not for neutrino oscillations. A more complicated term is required to account for this process.

In a similar manner as for the leptons, we can also add terms to the Lagrangian density which through the same mechanism will generate the masses of the quarks as well.

1.7 Shortcomings of the Standard Model - and theories beyond

Even though the Standard Model has been very successful in explaining the electroweak and strong interactions, along with the mechanism which makes the fermions and the electroweak gauge bosons acquire mass, there are still aspects with nature where the SM comes up short.

The fact that the weak interaction only couples to left-handed particles and right-handed antiparticles, is seen as a violation of an anticipated left-right symmetry. Theories that go beyond the SM, e.g. the so-called left-right symmetric models [13], provide solutions to how such a symmetry can be restored by introducing new gauge groups.

With the electroweak unification in mind, it is thought that there exists a higher symmetry where also the strong and electroweak interactions are unified. Models that address these issues are called grand unified theories (GUT). Similar to the left-right symmetric models, they predict the existence of new gauge symmetries along with new neutral gauge bosons of spin-1, often referred to as Z' bosons.

Another yet unexplained phenomenon, is the huge difference, of the order of 10^{16}, in the scale at which the electroweak symmetry spontaneously breaks and the Planck scale. This is called the hierarchy problem, and relates to the question of why the gravitational force is so much weaker than the SM forces at the electroweak scale. Among the proposed solutions are a new doublet of vector bosons (Z^*, W^*) [14], composite Higgs models with a new technicolor force [15] and models with extra dimensions [16], containing quantum black holes and graviton excitations of spin-2.

A short description of a few of these models, which predict new particles that can give rise to dilepton final-states, will be given in this section.

1.7.1 E_6-motivated Z' models

Several grand-unification models, including superstring theories, involve an E_6 gauge group [17], which can break in different ways to give the SM gauge group $SU(3)_C \times SU(2)_L \times U(1)_Y$, along with new gauge symmetries. One possibility is the following breakdown of E_6:

$$E_6 \rightarrow SO(10) \times U(1)_\psi, \tag{1.110}$$

where the SO(10) group can break further down, e.g. in terms of

$$SO(10) \rightarrow SU(4) \times SU(2)_L \times SU(2)_R, \tag{1.111}$$

or

$$SO(10) \rightarrow SU(5) \times U(1)_\chi. \tag{1.112}$$

Breaking of the $SU(2)_R$ symmetry in Eq. 1.111 can then result in a $U(1)_{3R}$ gauge group [18], where 3R denotes third component of right-handed weak isospin, giving rise to an associated Z'_{3R} gauge boson; or a new Z'_{B-L}, where B and L denotes baryon and lepton number, respectively,

from breaking the SU(4) and obtaining a $U(1)_{B-L}$ symmetry [18]. Both of these Z's could exist at the TeV scale.

The $U(1)_\psi$ and $U(1)_\chi$ in Eq. 1.110 and Eq. 1.111, respectively, are associated with new Z'_ψ and Z'_χ gauge bosons, where there can be a mixing of the two [17,18]. One of the corresponding symmetries can remain unbroken down to intermediate energy scales, and an observable Z' would then in general need to be described as a linear combination of the bosons belonging to the two gauge groups,

$$Z'(\theta_{E_6}) = Z'_\psi \cos\theta_{E_6} + Z'_\chi \sin\theta_{E_6}, \tag{1.113}$$

parametrized by the mixing angle θ_{E_6}.

1.7.2 The sequential Standard Model Z'

The sequential Standard Model Z' (or Z'_{SSM}) [18] is basically a heavier copy of the SM Z boson, where both are considered to have equivalent couplings to SM fermions. The Z'_{SSM} separates from the SM Z in its higher mass, where the width of the resonance is scaled up according to its pole-mass. It is not expected in terms of gauge theories, unless it has different couplings to exotic fermions, or arise as an excited state of the SM Z, in models with extra dimensions at the weak scale. Nevertheless, because of its simplicity, it is useful as a benchmark model for comparing constraints from different sources.

1.7.3 Graviton excitations in the Randall-Sundrum models

In the Randall-Sundrum models [16] the hierarchy problem is solved by adding a fifth dimension, where the higher-dimensional effective Planck scale is of the order of the electroweak scale. This is realized, in the original model, by two four-dimensional "branes", one confining the SM particles, called the TeV brane, and another where gravity originates, called the Planck brane; both situated within a five-dimensional bulk with a warped metric. Only gravity can propagate in the bulk, and gets exponentially suppressed, due to the warped geometry, when propagating from the Planck brane to the TeV brane. This makes gravity appear much weaker than the SM forces on the four-dimensional TeV brane. The fifth dimension is compactified, leading to Kaluza-Klein towers of excited graviton states.

The phenomenology of the RS model is characterized by the mass of the lightest Kaluza-Klein excitation mode of the graviton, G^*, and the coupling strength of the G^* to SM particles, described by the ratio $k/\bar{M}_{Pl}$, where k is a coupling that defines the warp factor of the extra dimension and $\bar{M}_{Pl} = M_{Pl}/\sqrt{8\pi}$ is the reduced Planck mass.

The branching ratio of the G^* to dileptons is relatively small, due to the spin-2 nature of the graviton. Dilepton searches are, however, sensitive to spin-2 resonances, because of the clean final-state.

Chapter 2

The LHC and the ATLAS detector

2.1 The LHC and particle collider experiments

The Large Hadron Collider (LHC) is to date the largest and most powerful particle accelerator that has been built. It consists of a 27 km long ring of superconducting magnets, with four main detector complexes along its path: ATLAS, CMS, ALICE and LHCb. The LHC is designed to accelerate bunches of up to 10^{11} protons with a rate of 40 million collisions per second. This was intended to provide a center-of-mass energy of $\sqrt{s}$ =14 TeV for proton-proton collisions with an instantaneous luminosity of 10^{34} cm^{-2}s^{-1}. Due to technical difficulties, the LHC operated at *pp*-collisions of 7 TeV in 2011 and 8 TeV in 2012, before shutting down for technical upgrades, and preparing for Run 2 at 13 TeV in 2015.

The LHC is also designed to accelerate lead nuclei at 5.5 TeV per nucleon pair, with an instantaneous luminosity of 10^{27} cm^{-2}s^{-1}, for studies of heavy-ion collisions.

2.1.1 Center-of-mass energy and invariant mass

The center-of-mass energy at which LHC operates, is essential with regard to which particles can be produced in collisions. Due to the energy-momentum relation

$$E^2 = (pc)^2 + (m_0c)^2, \tag{2.1}$$

where E is the total energy, $p = |\mathbf{p}| = |\gamma m_0 \mathbf{v}|$ is the momentum, $v = |\mathbf{v}|$ the velocity and m_0 the rest mass of a particle, it is possible to "convert" energy to mass, and vice versa. Because of energy and momentum conservation, we can by accelerating relatively light particles up to high energies and colliding them, produce new and heavier particles, where some of the energy of the initial-state particles have been used to create a heavier intermediate-state particle.

In terms of special relativity, the center-of-mass frame is a special case of the center-of-momentum frame, which is an inertial frame where the vector sum of all particles' momenta is equal to zero. The total energy of a particle at rest in this reference frame, will only be determined by its rest mass, since it has no kinetic energy in this frame. Hence, the mass of the particles being produced in collisions are bound by the amount of energy that LHC can give the colliding particles, as measured in the center-of-mass frame.

In the equivalent of Eq. 2.1 for a collection of particles, E, $\mathbf{p}$ and m_0 are replaced by sums over the respective quantities belonging to the particles in the system considered. The system of particles will then have a corresponding invariant mass $m = \sum_i m_{0,i}$ (equal in all reference frames), which is often expressed in terms of the quantity $s = m^2$, which is the invariant mass squared. For the case of two particles, the invariant mass of the system is given by

$$\sqrt{s} = m = \sqrt{(E_1 + E_2)^2 - (\mathbf{p}_1 + \mathbf{p}_2)^2}, \tag{2.2}$$

as expressed in natural units with $c = 1$. Eq. (2.2) is maximized when the vector sum of the colliding particles' momenta is equal to zero, i.e. in the center-of-mass frame, where $\mathbf{p}_1 = -\mathbf{p}_2$. Since the two particle beams at the LHC have equal energy and momenta, but opposite direction, the detectors of the experiments are in fact situated in the center-of-mass frame of the colliding beams. Thus, in the laboratory frame of the detectors, the total energy of the two particle beams, expressed in terms of E_1 and E_2, is equal to their center-of-mass energy $\sqrt{s} = E_1 + E_2$.

Since the colliding protons are composite particles, it is actually their quarks and gluons that go into the interactions that produce new particles. And since these interacting particles carry only a fraction of the protons', which will vary from collision to collision, their interactions will give rise to production of particles with a wide range of masses. Hence, the LHC is sometimes referred to as a discovery machine, because it gives us the possibility of probing a large energy domain.

2.1.2 Interaction cross-section and luminosity

The number of particles N produced at the LHC, by a certain process and over a certain amount of time of collisions, is given by

$$N = \sigma \int L(t)dt, \tag{2.3}$$

where σ is the interaction cross-section for the process and L is the instantaneous luminosity, integrated over time t. The cross-section is a measure of the quantum mechanical probability for the process to happen, which can be calculated using the Feynman rules in quantum field theory. The instantaneous luminosity is a quantity that links the number of events observed for a particular process, to its cross-section. At the LHC the protons in the accelerator are grouped into bunches, intended to be separated by 25 ns, corresponding to a collision frequency of $f = 40$ MHz. Assuming that the beams have a Gaussian profile and collide head-on, the instantaneous luminosity is then given by

$$L = f\frac{n_1 n_2}{4\pi\sigma_x\sigma_y}, \tag{2.4}$$

where n_1 and n_2 are the number of particles in the colliding bunches, and σ_x and σ_y are the root-mean-square (rms) horizontal and vertical beam sizes, respectively. These quantities may vary for different bunch-crossings, hence the denoted time dependence for the instantaneous luminosity $L(t)$ in (2.3).

The interaction cross-section has dimensions of area, and can be thought of as an effective cross-sectional area of a target particle, situated within a volume with an incoming flux of a certain type of particles. Then the size of the cross-sectional area per target particle, will represent the rate of interactions with the incoming particles per unit flux. The cross-section corresponding to particle interactions are very small when expressed in S.I. units, and therefore another unit, called "barn", is often used to express such quantities; where 1 barn $\equiv 10^{-28}$ m^2. In relation to processes on elementary particle level, the cross-sections are typically given in terms of picobarn (pb), where 1 pb $= 10^{-12}$ barn, and femtobarn (fb), where 1 fb $= 10^{-15}$ barn.

2.2 Interactions of particles with matter

Before giving an overview of the ATLAS detector at the LHC in Sec 2.3, this section will give a short description of how particles interact with matter. It is namely through such interactions with the detectors that we can measure the particles produced at the LHC. And by knowing the

characteristics of these interactions, we can identify the different types of particles based on the signatures they leave in the detectors.

This section is based on chapter 1.2 in Ref. [1].

2.2.1 Charged particles

Ionization

An electrically charged particle that passes through a medium will interact electromagnetically with the atomic electrons, and lose energy by ionizing the atoms in the medium. The energy loss of such a particle per unit length traversed in the medium, is given by the Bethe-Bloch equation

$$\frac{\mathrm{d}E}{\mathrm{d}x} \approx -4\pi\hbar^2 c^2 \alpha^2 \frac{nZ}{m_e v^2} \left[\ln\left(\frac{2\beta^2\gamma^2 c^2 m_e}{I_e} \right) - \beta^2 \right], \tag{2.5}$$

where $v = \beta c$ is the velocity of the particle, α is the fine-structure constant, m_e is the electron mass, Z is the atomic number and n the number density of the atoms in the medium. I_e is the effective ionization potential of the material, averaged over all atomic electrons, and can approximated by $I_e \sim 10Z$ eV. The energy loss per unit length is largest for small velocities, due to the $1/v^2$ dependency. For highly relativistic particles, with $v \approx c$, Eq. (2.5) depends logarithmically on $(\beta\gamma)^2$, where

$$\beta\gamma = \frac{v/c}{\sqrt{1-(v/c)^2}} = \frac{p}{mc}, \tag{2.6}$$

which gives a slow rise with increasing momentum p.

Expressing the number density in Eq. (2.5) as $n = \rho/(Am_u)$, where ρ is the density of the medium, A is the atomic mass number and m_u is the unified atomic mass unit, and dividing by ρ on both sides, the Bethe-Bloch equation becomes

$$\frac{1}{\rho}\frac{\mathrm{d}E}{\mathrm{d}x} \approx -\frac{4\pi\hbar^2 c^2 \alpha^2}{m_e v^2 m_u} \frac{Z}{A} \left[\ln\left(\frac{2\beta^2\gamma^2 c^2 m_e}{I_e} \right) - \beta^2 \right]. \tag{2.7}$$

While the rate of energy loss is proportional to the density, it is not significantly dependent on the type of material, since Z/A is approximately constant for most elements. The Bethe-Bloch equation has a minimum for $\beta\gamma \approx 3$; where particles corresponding to this value are called minimum ionizing particles.

All charged particles lose energy through ionization when traversing a medium, but the energy thresholds for when this process is important differs for different types of particles. Ionization is the main form of energy loss for muons, except at energies above about 100 GeV where also bremsstrahlung, discussed in the next section, is contributing. When propagating through iron, muons will lose approximately 13 MeV/cm, which makes it possible for muons to travel several meters in such materials.

Bremsstrahlung

For electrons at low energies, ionization is the dominant process of energy loss, but for electrons above a "critical energy" E_c, another process called bremsstrahlung instead becomes dominant. An electron then radiates a photon in the electromagnetic potential of a nucleus. The critical energy is approximately

$$E_c \sim \frac{800}{Z} \text{ MeV}, \tag{2.8}$$

where Z is the charge of the nucleus. Since the electrons of interest in particle physics experiments have energies of the order of several GeV, such electrons will be well above this critical energy, and thus lose energy predominantly through bremsstrahlung. While bremsstrahlung occurs for all charged particles, the rate of energy loss through this process is inversely proportional to the mass of the particle squared, and therefore is much less important for muons and heavier particles than it is for electrons. However, at very high energies, $E_\mu > 100$ GeV, bremsstrahlung will also be significant for muons.

The average distance over which electrons lose a factor $1/e$ of their energy through bremsstrahlung, is called the radiation length X_0, and is approximated by

$$X_0 \approx \frac{1}{4\alpha n Z^2 r_e^2 \ln(287/Z^{1/2})}, \tag{2.9}$$

where n is the number density of nuclei and r_e is the "classical electron radius",

$$r_e = \frac{e^2}{4\pi\epsilon_0 m_e c^2} = 2.8 \times 10^{-15} \text{ m}, \tag{2.10}$$

where ϵ_0 is the permittivity of vacuum. The radiation length is dependent on the atomic number Z, and is relatively short for high-Z materials, e.g. for iron and lead it is $X_0(\text{Fe}) = 1.76$ cm and $X_0(\text{Pb}) = 0.56$ cm, respectively.

2.2.2 Photons

Photons will at low energies mainly interact with materials through the photoelectric effect. In this process the photon is absorbed by an atomic electron, whereby the electron is emitted from the atom.

At higher energies, $E_\gamma \sim 1$ MeV, Compton scattering takes over as the dominant process. The photon is then inelastically scattered by interaction with an atomic electron, where the photon loses some of its energy to the electron.

At even higher energies, $E_\gamma > 10$ MeV, the dominant process for photons is the production of electron-positrion pairs, through interactions with the electromagnetic field of atomic nuclei. The radiation length X_0, given in Eq. (2.9), will be approximately 7/9 of the mean free path of the pair-production process for such high-energy photons.

2.2.3 Electromagnetic showers

A high-energy electron interacting with a material will radiate a bremsstrahlung photon, where this photon subsequently will produce an e^+e^- pair. These processes will continue to happen as the new photons, electrons and positrons also will interact with the medium, causing a cascade of particles, called an electromagnetic shower. Thus both electrons and photons with high energies will give rise to such cascades.

The number of particles in an electromagnetic shower approximately doubles with each radiation length traversed in the material. So, for an initial electron or photon of energy E starting an electromagnetic shower, the average energy of the individual particles after x radiation lengths will be

$$\langle E \rangle \approx \frac{E}{2^x}. \tag{2.11}$$

The shower will stop developing when the average energy of the particles involved gets below the critical energy E_c, where at this point the electrons and positrons will start to primarily lose

their energy through ionization. The number of particles in the shower will therefore be at a maximum after $x_{\max}$ radiation lengths, where $\langle E \rangle \approx E_c$. Inserting this condition in (2.11) gives

$$x_{\max} = \frac{\ln(E/E_c)}{\ln 2}. \tag{2.12}$$

For a high-Z material like lead with $E_c \sim 10$ MeV, an electromagnetic shower of 100 GeV will reach its maximum after $x_{\max} \sim 13X_0$, which corresponds to 10 cm of lead. Hence, electromagnetic showers deposit most of their energy in a relatively small region of space. Even though this is a stochastic process, the large number of particles involved leads to small deviations for different showers with approximately equal energy.

2.2.4 Hadrons

Electrically charged hadrons, like protons and charged pions, will in the same manner as charged leptons lose energy by ionizing the material they pass through, by interacting electromagnetically with the atoms of the medium. In contrast to leptons, hadrons consist of quarks and can thereby also interact with the atomic nuclei by the strong interaction. Such hadronic interactions make the hadrons split and produce new hadrons, resulting in a cascade of mostly charged pions, but also neutral hadrons like neutrons, π^0s and K_Ls. Hadronic showers are characterized by the nuclear interaction length λ_{I}, defined as the mean distance between hadronic interactions of relativistic hadrons. This is analogous to the electromagnetic radiation length X_0, but the nuclear interaction length is however considerably larger than its electromagnetic counterpart. For iron the nuclear interaction length is $\lambda_{\mathrm{I}} \approx 17$ cm, compared to its radiation length of $X_0 \approx 1.8$ cm.

Because of the many possible final states that can be produced in high-energy hadronic interactions, hadronic showers develop more variably than electromagnetic showers. Also, when π^0s are produced they will decay by $\pi^0 \to \gamma\gamma$, giving the shower an electromagnetic component. This electromagnetic contribution will vary from shower to shower, and is dependent on the number of π^0s being produced.

2.3 The ATLAS detector at the LHC

ATLAS (A Toroidal LHC ApparatuS) is built as a general purpose detector, meant for studying a wide range of particles and phenomena produced in *pp* and heavy-ion collisions.

The ATLAS detector basically consists of four different types of detectors:

- The inner detector: tracking and measuring the momentum of charged particles in a magnetic field
- The electromagnetic calorimeter: measuring the energy of electrons, positrons and photons
- The hadronic calorimeter: measuring the energy of hadrons
- The muon detector: tracking and measuring the momentum of muons in a magnetic field

A sketch of the full detector setup is shown in Fig. 2.1. There will in this chapter be given a short overview of the different components of the ATLAS detector, based on Ref. [20].

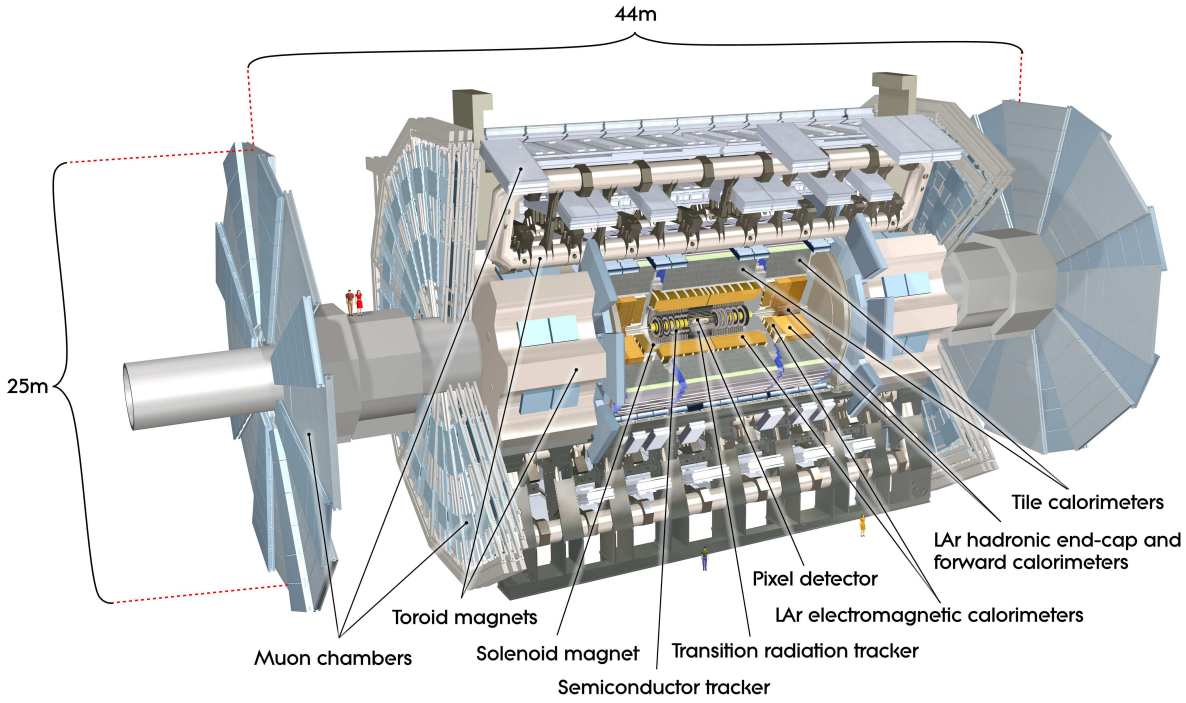

Figure 2.1: A full depiction of the ATLAS detector. From Ref. [20].

2.3.1 The ATLAS coordinate system

The center of the coordinate system is taken to be the nominal interaction point, with the z-axis pointing along the beam line and the $x-y$-plane transverse to the beam line; the positive x-axis is pointing towards the center of the LHC ring and the positive y-axis is pointing upwards. The azimuthal angle ϕ is the angle around the beam axis (0,2π), while the polar angle θ is the angle between the positive and negative z-axis (0,π). The pseudorapidity η is defined from the polar angle θ as $\eta = -\ln\tan(\theta/2)$, and the distance ΔR in the pseudorapidity-azimuthal angle space is defined as $\Delta R = \sqrt{(\Delta\eta)^2 + (\Delta\phi)^2}$.

2.3.2 The inner detector

The Inner Detector (ID), shown in Fig. 2.2, consists of two types of precision tracking detectors: silicon pixel and silicon microstrip (SCT) trackers, in addition to the Transition Radiation Tracker (TRT), consisting of straw tubes filled with xenon-based gas. The ID has a sylindrical shape with several concentric layers of trackers around the beam axis in the barrel region, while in the end-cap regions the trackers are located on discs perpendicular to the beam axis.

The innermost layers, closest to the interaction vertex region, consist of pixel detectors, that provide the highest granularity, which is needed for accurate vertex reconstruction. Particles typically pass three pixel layers, where the intrinsic accuracies in the barrel are 10 μm ($R-\phi$) and 115 μm (z) and in the disks 10 μm ($R-\phi$) and 115 μm (R). The addition of an extra Insertable B-Layer (IBL) [21], in time for Run 2, provides an additional tracking layer, between the existing b-layer and the beam-pipe. This enhances the tracking precision and reconstruction of secondary vertices, which is essential to identify the rapidly decaying b-quarks. The IBL is also meant to help the inner detector to better cope with the higher luminosity in the upcoming run, resulting in increased radiation damage of the silicon detectors.

For the SCT, eight layers are crossed by each track, corresponding to four space-points. The

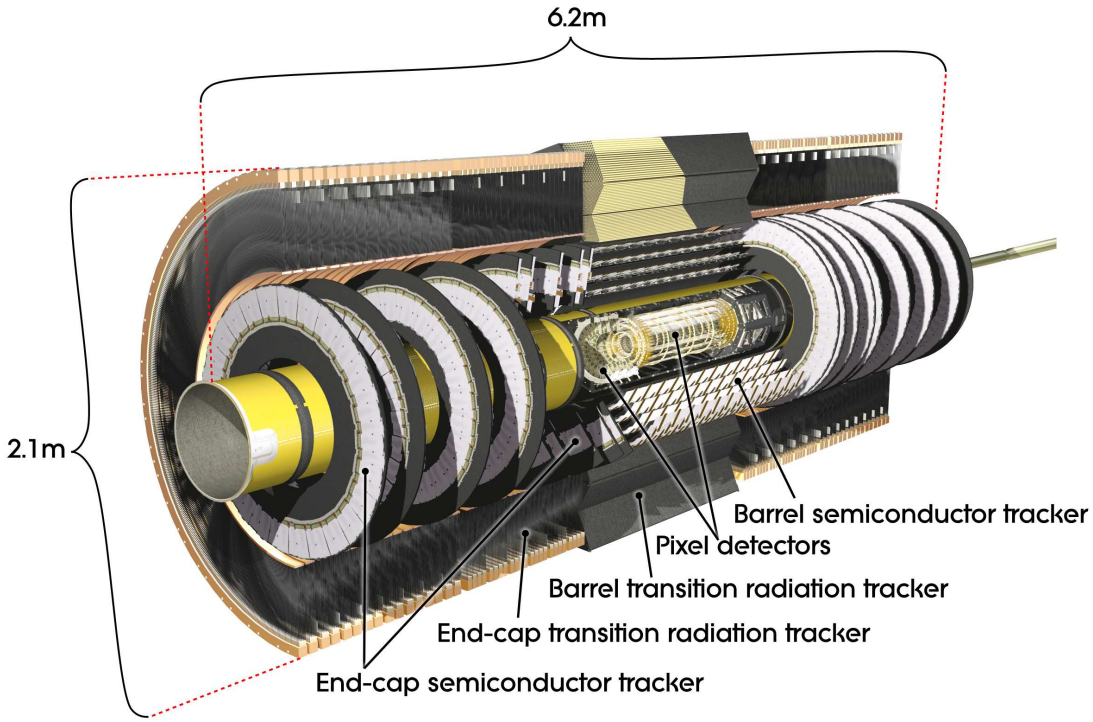

Figure 2.2: The ATLAS inner detector setup. From Ref. [20].

intrinsic accuracies for the strip detectors are in the barrel region 17 μm ($R-\phi$) and 580 μm (z) and in the disks 17 μm ($R-\phi$) and 580 μm (z).

The outermost region of the ID is covered by TRT straw tubes, which are 4 mm in diameter each. In the barrel region the straws are lying parallel to the beam axis an are 144 cm long. They only provide $R-\phi$ information, and have an intrinsic accuracy of 130 μm per straw. In the end-cap regions the straws are 37 cm long and are placed radially in wheels. Typically 36 hits are measured by the TRT per track, which, despite lower spatial resolution compared to the silicon trackers, are taken at larger radii and are important in measurements of momentum. Detection of transition-radiation photons in the gas of the straw tubes enhances the capabilities of electron identification.

The ID is immersed in a 2 T magnetic field provided by a solenoid. Due to the Lorentz force experienced by charged particles in a magnetic field, the particles will be deflected perpendicularly to the direction of the B-field, and hence make helical trajectories through the detectors. The arc of these trajectories are used to calculate the momentum of the corresponding particles.

The precision tracking detectors cover the region $|\eta| < 2.5$, while the TRT has coverage for $|\eta| < 2$. The p_{T} resolution of the ID tracking detector, together with the η coverage and p_{T} and energy resolution of the other subdetector systems, is given in the table in Fig. 2.6.

2.3.3 The electromagnetic calorimeters

The electromagnetic (EM) calorimeters, which can be seen as the inner parts of the illustration in Fig. 2.3, are divided into a barrel part, for $|\eta| < 1.475$, and two end-cap parts covering $1.375 < |\eta| < 3.2$, each placed within their own cryostat. The barrel part consists of two half-barrels separated by a small gap of 4 mm at $z = 0$. The end-cap parts consist of two separated coaxial wheels; an outer wheel covering the region $1.375 < |\eta| < 2.5$, and an inner wheel covering $2.5 < |\eta| < 3.2$.

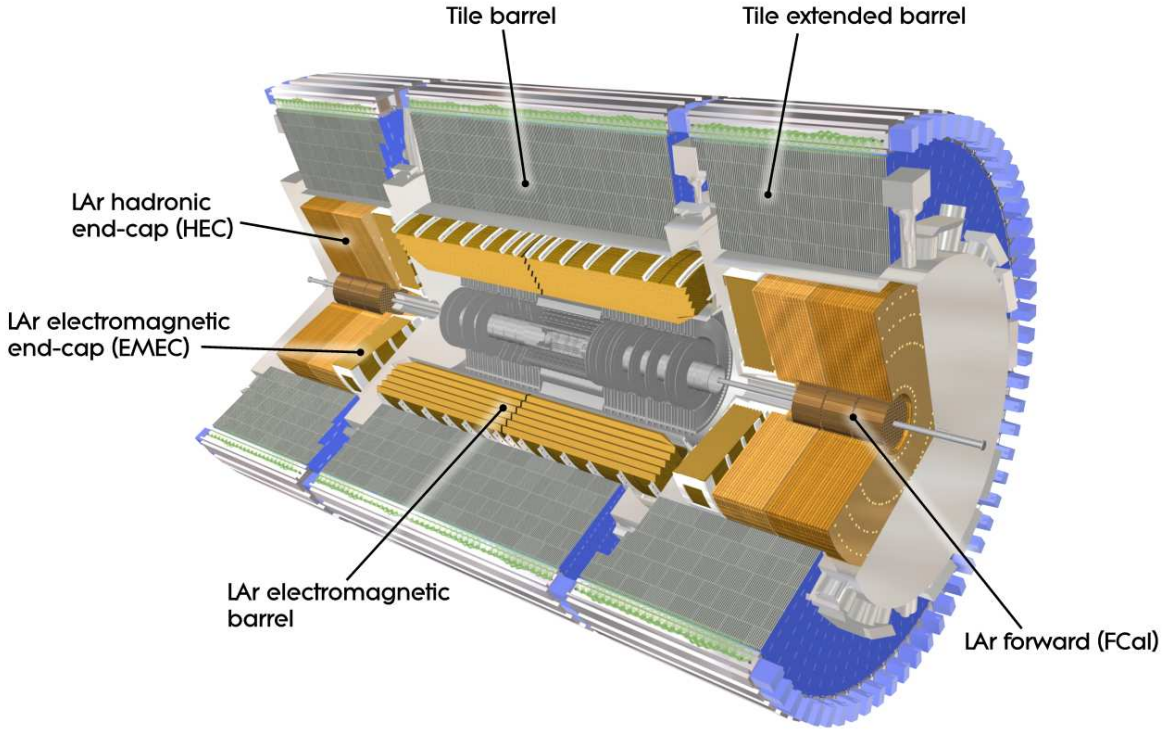

Figure 2.3: A visuaization of the electromagnetic and hadronic calorimeters in ATLAS. From Ref. [20].

The detector consists of Liquid Argon (LAr) and lead absorber plates, with accordian-shaped kapton electrodes. The accordian geometry makes a complete azimuthal coverage possible, without cracks. The thickness of the absorber plates have been optimized w.r.t. the energy resolution of the EM calorimeter as a function of η. The region $|\eta| < 2.5$ is devoted to precision physics, and therefore the EM calorimeter is in this region segmented in three sections in depth, while the end-cap parts have two sections in depth with courser lateral granularity.

In order to make good measurements of the particles' energy, they need to deposit as much energy as possible in the calorimeter. The total thickness of the EM calorimeter is hence > 22 radiation lengths X_0 in the barrel region and $> 24X_0$ in the end-caps, to prevent punch-through into the muon system.

In the region of $|\eta| < 1.8$ a presampler detector is placed to correct for the energy lost by the electrons and photons before they reach the calorimeter. It is 1 and 0.5 mm in the barrel and end-cap regions, respectively, and consists of a layer of active LAr.

2.3.4 The hadronic calorimeters

To detect the energy of hadrons a tile calorimeter is placed directly outside of the EM calorimeter, with a coverage in the barrel region of $|\eta| < 1.0$ and in the extended barrel region $0.8 < |\eta| < 1.7$. It uses steel as the absorber and scintillating tiles as the active material. Two sides of the scintillating tiles read out the produced photons into wavelength shifting fibres, which are collected by photomultiplier tubes. The tile calorimeter extends from an inner radius of 2.28 m to an outer radius of 4.25 m, segmented in three layers in depth. This corresponds to approximately 9.7 interaction lengths λ.

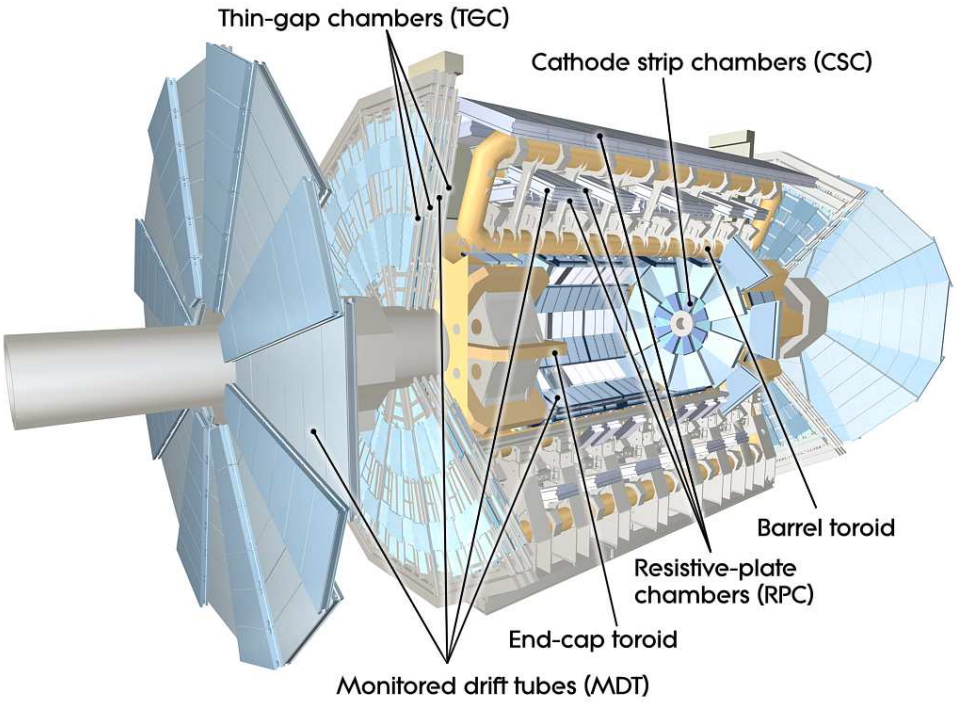

Figure 2.4: The muon system of the ATLAS detector. From Ref. [20].

In the end-caps there are Hadronic End-cap Calorimeters (HEC), using copper plates as absorber material with LAr as the active medium. The coverage of the HEC is $1.5 < |\eta| < 3.2$, which overlaps the covering regions of the tile calorimeter extending to $|\eta| < 1.7$ and the forward calorimeter starting from $|\eta| < 3.1$. It consists of two independent wheels, placed right behind the EM end-cap calorimeters, each wheel divided into two segments in depth. The wheel closest to the interaction point on either side are built from 25 mm parallel copper plates, while those further away are built from copper plates of 50 mm in thickness. The copper plates have a parallel spacing of 8.5 mm, where the LAr is stored in between.

The Forward Calorimeter (FCal) consists of three modules covering the region $3.1 < |\eta| < 4.9$: the one nearest the interaction point, using copper as absorber and is optimized for electromagnetic measurements, while the two others are built from tungsten and measure primarily the energy of hadronic interactions. All three modules use LAr as the active medium. In total they correspond to approximately 10 λ in depth.

The hadronic calorimeters are shown in the outer parts of the illustration in Fig. 2.3, with the energy resolutions given in Fig. 2.6.

2.3.5 The muon spectrometer

The Muon Spectrometer (MS), illustrated in Fig. 2.4, is based on magnetic deflection of muon tracks by large superconducting air-core magnets. A large barrel toroid provides the magnetic bending in the barrel region $|\eta| < 1.4$. For $1.6 < |\eta| < 2.7$ the muons are deflected by two end-cap toroids, one in each end of the barrel toroids. In the transition region, $1.4 < |\eta| < 1.6$, both the barrel and the end-cap toroids will contribute to the muon deflection. These magnets will produce a toroidal magnetic field of approximately 0.5 T and 1 T as experienced by the muon detectors in the central and end-cap regions, respectively. The field is mostly orthogonal to the muon trajectories, minimizing the degrading effect of multiple scattering on the energy

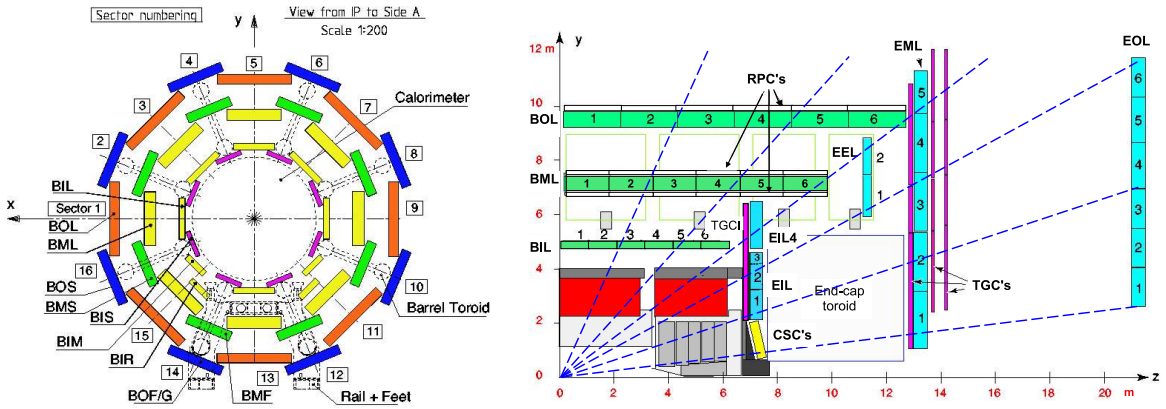

(a) (b)

Figure 2.5: The muon spectrometer as seen in (a) the transverse plane: 3 coaxial layers (inner, middle and outer) with 16 sectors, of which there are 8 large (odd-numbered) and 8 small (even-numbered); and (b) the rz-plane: showing the barrel (B) and end-cap (E) stations of the MDTs along with the CSCs in the forward region. The straight dashed lines indicate trajectories of muons with infinitely high p_{T} (no curvature), which would typically traverse three muon stations. From Ref. [20].

resolution.

In the barrel region the chambers which measure the muon tracks are placed in three cylindrical layers centered around the beam axis, while for the transition and end-cap regions the chambers are installed in three plane layers perpendicular to the beam line. Precision measurements of the track coordinates, in the principal bending direction of the magnetic field, are done by Monitored Drift Tubes (MDT) over most of the η range. At large pseudorapidities, $2 < |\eta| < 2.7$, Cathode Strip Chambers (CSC) with higher granularity are used to withstand the demanding rate and background conditions. The configuration of the MDT and CSC layers is shown in Fig. 2.5. Very high precision has to be maintained in the alignment of the different muon chamber layers. To this end precision mechanical assembly techniques have been used, along with optical alignment systems monitoring the relative positions both within and between muon chambers.

The muon system also has a trigger system covering the range $|\eta| < 2.4$, consisting of Resistive Plate Chambers (RPC) in the barrel and Thin Gap Chambers (TGC) in the end-cap regions. The positioning of these trigger chambers is illustrated in Fig. 2.7. The muon trigger chambers have three functions: provide bunch-crossing identification, provide well-defined p_{T} thresholds, and measure the muon coordinate in the direction orthogonal to that determined by the precision-tracking chambers. The p_{T} resolution and η coverage of the MS is given in Fig. 2.6.

2.3.6 The trigger system

The LHC is designed to provide a collision rate of 40 MHz, which corresponds to 25 ns between subsequent bunch-crossings. The trigger system's task is to select only the events which contain features of interest, out of the enormous amount of information measured by the detectors. It consists of three trigger levels of different complexities. The Level-1 (L1) trigger, which is hardware-based, and the Level-2 (L2) trigger and event filter, which are software-based, and collectively referred to as High-Level Triggers (HLT).

The L1 trigger constitutes the lowest level, which uses reduced-granularity information from

Detector component	Required resolution	η coverage	
		Measurement	Trigger
Tracking	$\sigma_{p_T}/p_T = 0.05\%\ p_T \oplus 1\%$	± 2.5	
EM calorimetry	$\sigma_E/E = 10\%/\sqrt{E} \oplus 0.7\%$	± 3.2	± 2.5
Hadronic calorimetry (jets)			
barrel and end-cap	$\sigma_E/E = 50\%/\sqrt{E} \oplus 3\%$	± 3.2	± 3.2
forward	$\sigma_E/E = 100\%/\sqrt{E} \oplus 10\%$	$3.1 < \lvert\eta\rvert < 4.9$	$3.1 < \lvert\eta\rvert < 4.9$
Muon spectrometer	σ_{p_T}/p_T=10% at p_T = 1 TeV	± 2.7	± 2.4

Figure 2.6: The required resolution in energy and transverse momentum, along with the η coverage, corresponding to the different subdetector systems of ATLAS. From Ref. [20].

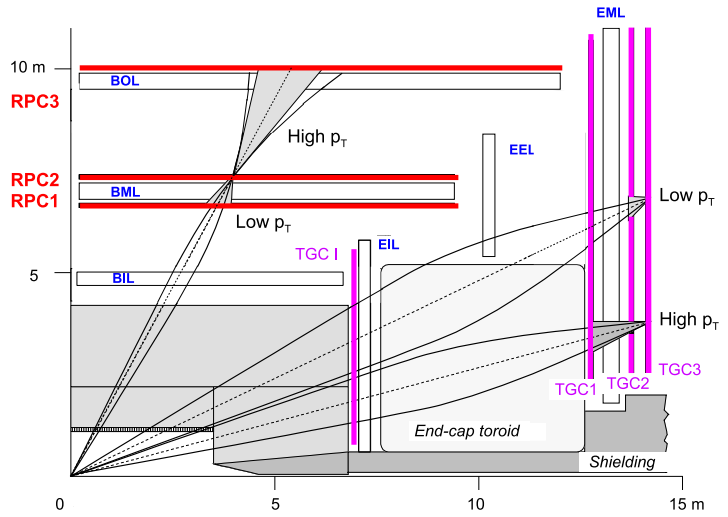

Figure 2.7: The muon trigger chambers (RPCs and TGCs), where RPC2 and TGC3 are chosen to be reference (pivot) layers for momentum measurements. The deviation from straight lines are found by considering hits in RPC2 and RPC3 (RPC1), and TGC3 and TGC1 (TGC2), for high (low) p_{T} muon triggers in the barrel and end-cap regions, respectively. From Ref. [20].

a subset of the detectors to search for signatures of high-p_{T} muons, electrons/photons, jets and τ-leptons (decaying into hadrons), in addition to events with large missing energy ($E_{\mathrm{T}}^{\mathrm{miss}}$) and events with large total transverse energy. The Resistive Plate Chambers (RPC) and Thin-Gap Chambers (TGC) are used to detect high-p_{T} muons, while all calorimeter subsystems are used to select electromagnetic and hadronic clusters, jets, taus, $E_{\mathrm{T}}^{\mathrm{miss}}$ and large total transverse energy. A decision is made in less than 2.5 μs, reducing the acceptance rate to about 75 kHz.

The L2 trigger makes use of the full granularity and precision information from all subdetectors, within Regions-of-Interest (RoI) defined at L1, which are regions in η and ϕ coordinates that contain interesting features. The RoI data, corresponding to about 2 % of the total event data, include information on the type of objects identified, and which criteria or thresholds that have been passed. The L2 selections reduce the trigger rate to about 3.5 kHz, with an average event processing time of approximately 40 ms.

The last stage in the trigger selection is performed by the event filter, which makes use of offline analysis procedures, meaning, with access to information of fully reconstructed objects. With an average event processing time of the order of four seconds, the event rate is reduced to about 200 Hz, and corresponds to a data size of approximately 1.3 MB per event.

The data acquisition system (DAQ) receives and buffers the event data from the detector-specific readout electronics at the L1 trigger rate. For those events that pass the L2 selection, event-building is performed, and the resulting events are then moved by DAQ to the event filter. The events which pass the final trigger selection, are ultimately moved to permanent event storage.

Chapter 3

The new analysis model in ATLAS for Run 2 at $\sqrt{s} = 13$ TeV

The 2013-2014 shutdown of the LHC provided an opportunity to evaluate the analysis model used by ATLAS in Run 1, as part of a full-scale software and computing upgrade to cope with harsher conditions at higher energies and luminosities. It was found that this model had some limitations, and it was decided to redesign the analysis model for the upcoming run of data-taking.

In the event data model (EDM) used during Run 1, the output from the reconstruction was stored in the AOD (analysis object data) format. This EDM involved an organization of the data which was not readable by the analysis framework ROOT [22], and thereby required the full ATLAS offline software framework Athena [23] to be read and handled properly. ROOT-readable samples called D3PDs (derived physics data formats with a flat n-tuple structure) were produced centrally in ATLAS, but these formats were typically very big ($\sim$ 50 % of the full AOD). This led many users to start a rather chaotic, non-controlled production of simplified and ROOT-readable versions, either from the full AODs or from the D3PDs. Hence, data were duplicated, resulting in the combined size of these intermediate-sized formats taking up about three times the size of the corresponding AOD. This also led to duplication of analysis tools, which had to support the different ROOT-friendly formats.

3.1 The new event data model

The solution to the above-mentioned difficulties was to design a new data format, called xAOD [24], which can be read and handled in both ROOT and Athena. It is produced directly from the reconstruction process, thus providing a ROOT-compatible format without any conversion/production delay, while keeping the structure of the EDM.

The old EDM stored the data as an "array of structures", meaning that each reconstructed particle (or other reconstructed object) was stored as an element in an array, where each element was an object of a class/struct, with its attributes (transverse momentum, mass, etc.) stored as member variables of the object.[1] This was found not to be an optimal solution. The new EDM instead stores the data as a "structure of arrays", while maintaining an interface that appears as an "array of structures". This means that the objects seen by the user usually have no member variables, i.e. are separated from their attributes, where these attributes instead are stored in arrays in a separate "auxiliary store". The organization of data storage in the xAOD format is illustrated in Fig. 3.1.

[1] Object, class and struct refer to expressions in the C++ programming language.

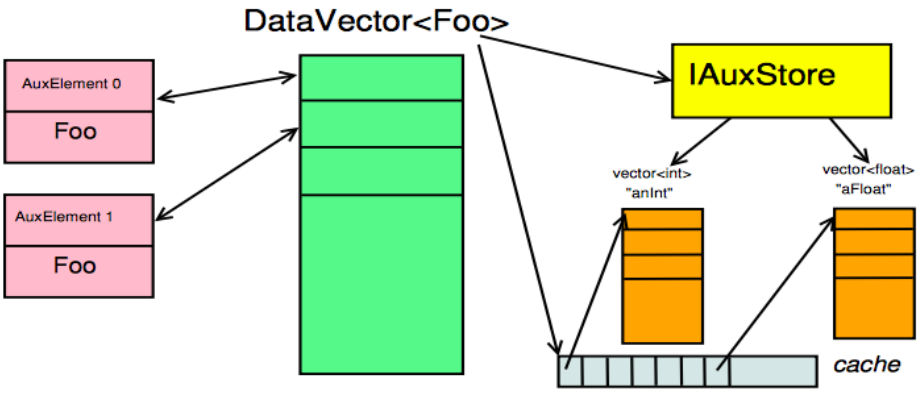

Figure 3.1: Illustration of the separation of objects and their attributes in the xAOD format. The objects, here of an imaginary type "Foo", are stored in a "DataVector", whereas their variables "anInt" and "aFloat" are stored in vectors in the auxiliary "IAuxStore". The "cache" row in the lower right of the figure, reflects that a variable is cached in memory on first lookup, so it does not need to be done each time the variable is accessed. From Ref. [24].

The separation of the objects from their stored attributes makes new and convenient features possible. Each container in the xAOD (collection of a type of objects, such as muons) has a "static" auxiliary store, containing the variables given to the original xAOD, and a "dynamic" auxiliary store, where additional variables can be added by the user. In addition, a "shallow copy" of a container can be made, where only the interface array of objects is copied, while a new "ShallowAuxContainer" with references to the static auxiliary store is created. This makes it possible to change a few variables in the shallow copy, while sharing the storage for the rest of the data. The auxiliary store also makes partial object reading on-demand possible, whereas the old EDM required operation on a whole object at a time.

3.2 The derivation framework

For a specific data analysis only a fraction of the total data in the full xAOD is needed. Thus, intermediate-sized formats containing the relevant objects and variables for specific purposes, are both convenient and necessary to perform an efficient analysis. In order to reduce the duplication of such derived formats experienced in Run 1, and to relieve the users of the time consuming and computationally heavy work of producing these samples, this job will for Run 2 be coordinated centrally in ATLAS. To this end a common software has been developed, called the "derivation framework" [25]. It is implemented in the Athena framework, and is meant to produce derived samples in terabyte-size from the full reconstruction sample with size of order petabyte.

The derivation framework produces reduced versions of the full xAOD, referred to as DxAODs (derived xAODs), where these derived formats maintain the EDM of the xAOD. The removal of data is done by three different operations:

- **Skimming:** removal of whole events, based on features of the event.
- **Thinning:** removal of individual objects within an event, based on features of the object.
- **Slimming:** removal of variables for a given object type, for all objects of that type in all events; not based on features of the objects or events.

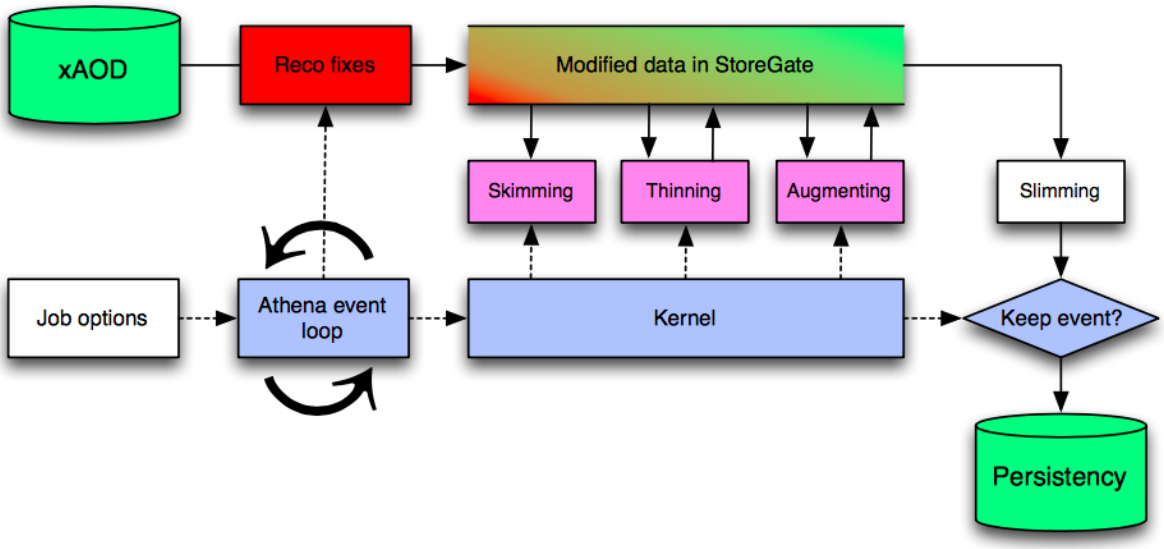

Figure 3.2: The steps performed by the derivation framework. The "kernel" is an algorithm configured for the specific format to be produced, and steers the skimming, thinning and augmenting, but not the slimming, which is done separately. "Persistency" denotes data storage on disk, as opposed to "transient" storage, which is temporary storage in memory. From Ref. [25].

There is also the possibility of **augmentation**, that is to add information which was not there in the original xAOD. This can be done in two ways: (i) adding entirely new containers of reconstructed objects from the information stored in the primary xAOD, typically for jets and missing energy containers, and (ii) adding new variables to existing objects, called decoration.

The framework provides an interface and tools for users to implement the selection or augmentation to the samples. The instructions are given in terms of strings, which are parsed at the beginning of the job and creates a virtual machine to perform the commands. Names of containers, objects and variables in the xAOD can be used, with support for operators, unary mathematical functions and constants.

The derivation framework also contain built-in lists of variables needed to perform combined performance operations on reconstructed objects, such as smearing, scaling, selection and calibration. This ensures that the derived formats keep the information necessary to apply such operations in the specific analysis the format is targeted for.

Based on the practice in Run 1, it has been estimated that approximately 100 derived formats will be needed for Run 2 analyses. A requirement has been put on the total size of the derived samples, that it does not exceed the size of the full xAOD, i.e. that each derived sample on average should not be larger than 1 % of the full xAOD. An additional constraint is set on the turn-around time of the production of these samples, which should only take a few days, especially with the periods of data-taking in mind.

As the derivation framework is implemented in Athena, it is well suited to apply fixes at the reconstruction level, produce multiple output formats when accessing a single input file (referred to as train production) and provide monitoring tools for output format size, overlaps and CPU usage.

The steps performed by the derivation framework are shown in Fig. 3.2.

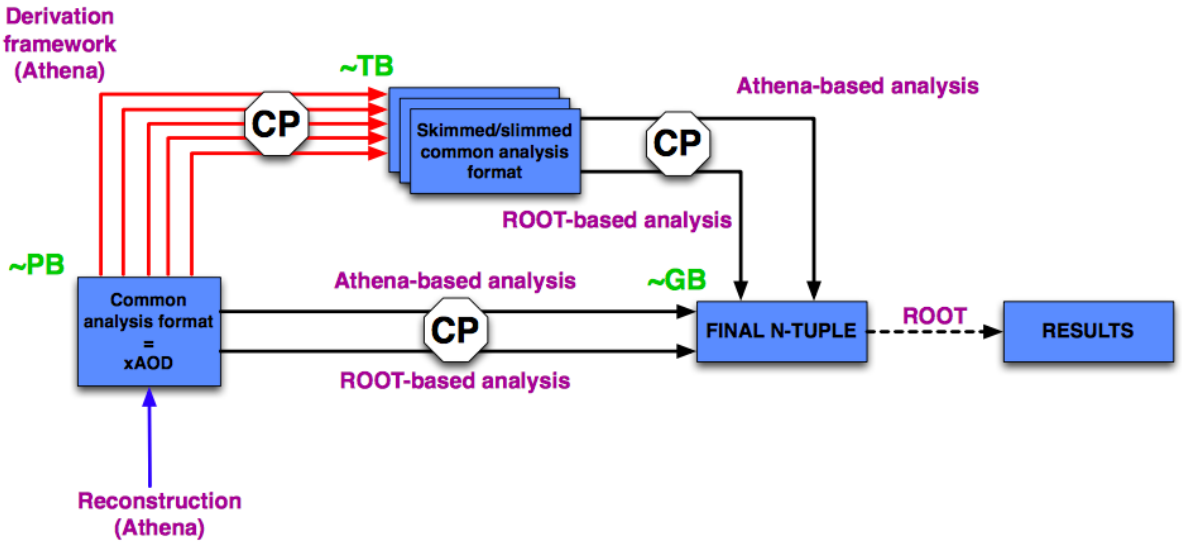

Figure 3.3: The analysis model in ATLAS for Run 2. "CP" denotes application of combined performance group recommendations, and "final n-tuple" represents a ROOT format typically produced by the user for the last stage of the analysis. From Ref. [25].

3.3 Performance

The new EDM is an important contributor to the overall speedup experienced by the ATLAS reconstruction of about three times that in Run 1 [24]. Also the auxiliary store implementation has in dedicated tests been shown to be 25 % to three times faster than the corresponding storage implementation in the previous run. The size of analysis data for 25 interactions per bunch crossing is approximately 240 kB/event, which is similar to Run 1 and within the budget of 250 kB/event.

The derivation framework has successfully provided derived formats for the Run 2 preparations, and the derivation production workflow has been fully integrated in the new ATLAS production system (ProdSys2) [26]. With 60 derived formats defined and 20 under development, a large fraction of these satisfy the aim of taking up less than 1 % of the size of the full xAOD, where the total size of the derived samples is just below the size of the input. The overlaps between the different derived formats have also been shown in most cases not to be excessive.

Two different derived formats have been considered for the analyses of this thesis; one requested by the SM working group (called STDM3), and another format requested by the exotics working group (called EXOT0). Both formats have been used successfully in the analyses, and provided samples which are more convenient to handle compared to the full xAODs. This is much due to the samples' smaller size, which makes them easier to download and handle on a local machine, and can also shorten the computation time drastically. The possibility of adding information to the samples, is another very useful feature. This has made it possible to e.g. add support for combined performance tools to the derived samples, even though these were not made ready for the production of the xAODs.

The data flow in the new analysis model is illustrated in Fig. 3.3.

Chapter 4

8 TeV analysis

The objective for this analysis is to search for resonances in the dimuon invariant mass ($m_{\mu\mu}$) spectrum, which deviates from the expected background of Standard Model processes. Many theories that go beyond the SM predict new particles that can decay to dimuons in the final state, which makes it a promising channel to search for new physics. The signal can be fully reconstructed, since no missing energy, e.g. in terms of neutrinos, is expected. In addition, looking at the full invariant mass line shape makes the search robust against uncertainties in the background estimates at high mass [19]. If the shape information is not used in the analysis, the uncertainty in the background estimate will be more likely to mask a potential signal. The shape-based method is also more sensitive to a signal with a low-mass tail arising from off-shell production (contribution from virtual particle production to the resonance), due to the steeply falling parton distribution function (PDF) for the two colliding partons at large momentum fractions, Bjorken x, out of the total proton momentum. The different theoretical models motivating the search in this channel predict resonances with different widths and line shapes, arising from particles with different intrinsic spin. This search is meant to be model independent, i.e. looking for any deviations from the expected background, not focusing on a specific theoretical model.

Since the data used in this analysis have already been thoroughly analyzed and published in Ref. [19], which include exclusion limits on mass for a number of different theoretical models, the focus of the analysis will be to handle both data and simulations in the new event data model (EDM) for use in Run 2, rather than to perform a full statistical analysis. It is important to verify that the new EDM is handling the data properly, and can be used to produce reasonable results for the analysis of the 13 TeV data. The analysis results obtained with the new EDM will then be compared to the published results from the old EDM, and thus check whether the new model is able to provide corresponding results.

4.1 Event and muon selection

When analyzing experimental or simulated data, events and single muons are kept or discarded based on a set of requirements. This is done in order to secure good acceptance and efficiency for the signal of interest, and to minimize the contribution from background, i.e. from the processes we are not looking for. In addition, an efficient event selection will give smaller output files and reduce computation time.

The list of selections applied to the 8 TeV samples are listed below, followed by a more elaborate explanation of what they comprise and how they were applied.

Event level:

- Good Runs List
- Event cleaning
- Emulated triggers: EF_mu24i_tight or EF_mu36_tight
- ≥ 1 primary vertex, with ≥ 3 tracks and $|z_{\mathrm{PV}}| < 200$ mm
- ≥ 2 combined muons

Muon level:

- $p_{\mathrm{T}} > 25$ GeV
- $|\eta| < 2.5$
- Quality: medium
- ID hits: Muon Combined Performance requirements on ID hits
- MS hits: Muon Combined Performance requirements on MS hits
- Transverse impact parameter: $|d_0| < 0.2$ mm
- Longitudinal impact parameter: $|z_0| < 1$ mm
- Isolation: $\sum_{\mathrm{trk}} p_{\mathrm{T}}^{\mathrm{trk}}(\Delta R < 0.3)/p_{\mathrm{T}}^{\mu} < 0.05$

Dimuon level:

- Dimuon candidate with the highest p_{T} scalar sum
- Muons in the pair have opposite-sign charge

4.1.1 Event level

For experimental data, the event has to be in the Good Runs List (GRL) chosen for the analysis. This is a list containing information about the quality of luminosity blocks in each run of data taking. If the data quality is flagged as good enough to be included in an analysis, based on detector performance, among other aspects, the luminosity block is characterized as good, otherwise it is labeled bad. Only events produced in good luminosity blocks are kept for the analysis. The GRL used in this analysis is listed in the appendix.

To avoid throwing away entire luminosity blocks, if there are only a few problematic events, there are three flags set for each event in the 2012 data samples. These are indicating malfunction in the liquid argon and tile calorimeter systems, in addition to incomplete events. These flags are checked for each event, and those considered as problematic, are not included in the analysis.

The triggers used for the official ATLAS analysis at 8 TeV were EF_mu24i_tight and EF_mu36_tight. These are Event Filter (EF) triggers corresponding to a single isolated muon with $p_{\mathrm{T}} > 24$ GeV and a single muon with $p_{\mathrm{T}} > 36$ GeV and without any isolation requirement, respectively. The event must pass at least one of these triggers, where the latter is chosen to account for small inefficiencies in the isolation estimation of the former. Tight refers to a requirement of $p_{\mathrm{T}} > 15$ GeV at the L1 hardware trigger level. Since the xAOD samples considered in this analysis were lacking trigger information (less than a month before delivering this thesis),

the trigger selection tools could not be applied to select muons that have actually been triggered. Instead, the triggers were emulated by performing the corresponding offline cuts in the analysis code. More information about the trigger emulation is given at the end of this section.

The event is required to have at least one reconstructed primary vertex, with more than two tracks associated with it. The primary vertex of an event is chosen to be the reconstructed vertex with the highest $\sum p_{\mathrm{T}}^2$, where the sum includes the p_{T}^2 of all tracks belonging to the vertex. More than one primary vertex may be present in the recorded event due to pile-up. To suppress background from cosmic rays, the primary vertex is required to have an absolute z-position, $|z_{\mathrm{PV}}|$, of less than 200 mm w.r.t. the beamspot, i.e. the nominal interaction point.

The muon tracks are first reconstructed separately in the ID and MS, and then put together in a combined fit to give what we call a combined muon. At least two combined muons are required for the event to pass the selection.

Trigger emulation

Due to the fact that the 8 TeV data were originally processed with the EDM used for Run 1, and that this analysis is performed in the new EDM to be used for Run 2, the available data samples, analysis tools and functionality for use with old samples in the new EDM are somewhat limited. The data samples considered for the 8 TeV analysis lack trigger information, and the standard trigger decision tools could therefore not be used to select events that passed the real trigger selection. To mimic the behavior of the trigger system, the cuts and selections that are possible to make, based on the information available in the samples, are then applied.

For a single muon to pass the emulated trigger selection of EF_mu24i_tight, it must satisfy the following requirements [37]:

- combined (ID and MS),
- $p_{\mathrm{T}} > 24$ GeV, and
- isolated:

$$\frac{\sum_{\mathrm{trk}} p_{\mathrm{T}}^{\mathrm{trk}}}{p_{\mathrm{T}}^{\mu}} < 0.12, \tag{4.1}$$

  where p_{T}^{μ} is the transverse momentum of the muon, and the sum is over the p_{T} of all tracks, except the muon itself, having $p_{\mathrm{T}} > 1$ GeV and being within a cone of $\Delta R = \sqrt{(\Delta\eta)^2 + (\Delta\phi)^2} = 0.2$ from the muon; and satisfying

$$|z_0(\text{ID track}) - z_0(\text{muon})| < 6 \text{ mm}. \tag{4.2}$$

The requirement on z_0 is to reduce the contribution from pile-up. For the p_{T} sum, the requirements are checked and the sum is calculated by looping over all inner detector track objects, rather than using the "ptcone20" variable found in the datasets.

The emulation of EF_mu36_tight is a lot simpler, and has only two requirements on the muons [37]:

- combined, and
- $p_{\mathrm{T}} > 36$ GeV.

Both the trigger names end with "tight", which refers to a requirement of $p_{\mathrm{T}} > 15$ GeV at the L1 level, which is the first and less complex trigger level where the selection is made by hardware. Muons that pass the higher level triggers have also passed the L1 trigger, so apart from being out of reach, the tight requirement should not be necessary to consider for emulation at the analysis level.

4.1.2 Muon level

When an event has passed the event selection, a loop over single muons in the event is performed. To pass the single muon selection, the muon needs to fulfill a number of criteria.

The muon is required to be combined and have a transverse momentum $p_{\mathrm{T}} > 25$ GeV.

The Muon Combined Performance (MCP) group in ATLAS gives guidelines on how to select "good" muons, taking detector performance and resolution, among other aspects, into account. The group also provides an official tool to select muons based on how many and which detector layers they hit, the "quality" of the muon, and so on, where in some cases one can choose how strict one wants the selections to be. This tool, called the MuonSelectionTool, has been used to select muons that fullfill certain requirements in the inner detector and muon spectrometer. The default values of the muon selection tool were used for η and muon quality; $|\eta| < 2.5$, and medium quality. The latter means that the muon in question must have caused at least 3 hits in at least 2 MS precision layers (MDT or CSC), or in the case of at least 3 hits in only 1 of the precision layers, the number of traversed precision layers with holes and no hits must at most be 1.

The requirements on inner detector hits are:

- Number of pixel hits + number of dead pixel sensors crossed ≥ 1
- Number of SCT hits + number of dead SCT sensors crossed ≥ 5
- Number of pixel holes crossed + number of SCT holes crossed $le2$
- If $0.1 < |\eta| \leq 1.9$: number of TRT hits + number of outliers ≥ 6, with outlier fraction $<$ 0.9 (90 %)

The MuonSelectionTool is also applied to select muons based on hits in the muon spectrometer, where at least 3 hits in each of 3 different MS layers (called 3-station muons) are required.

The absolute value of the transverse impact parameter d_0 of the muon track, w.r.t. the primary vertex, is required to be less than 0.2 mm, while the longitudinal impact parameter z_0 (along the beam-axis) must be within 1 mm w.r.t. the primary vertex. This is done to suppress the contribution from cosmic rays.

Muons are sometimes produced in jets, which arise from hadrons such as b and c quarks, and from decays of pions and kaons in flight. The hadrons in a jet can decay to give real muon, or a jet can trick the reconstruction into building fake muons. Since a jet will show up in the detectors as a cone of tracks, we can suppress the contribution from jets to the muon signal by requiring that the muon track is isolated. In this case this is done by summing the p_{T} of all tracks, except the muon track itself, with $p_{\mathrm{T}} > 1$ GeV within a cone of $\Delta R = \sqrt{(\Delta\eta)^2 + (\Delta\phi)^2} = 0.3$ from the muon track, and demanding that the ratio of $\sum_{\mathrm{trk}} p_{\mathrm{T}}^{\mathrm{trk}}$ to the muon p_{T} is less than 0.05. The p_{T} sum of all the inner detector tracks fulfilling these criteria, is obtained from a variable belonging to the muon objects in the datasets, called "ptcone30".

4.1.3 Dimuon level

One dimuon candidate is chosen for each event, out of the muons that have passed the single muon selection described above. The pair of muons with the highest transverse momentum scalar sum, where these two muons must have electric charge of opposite sign, is chosen as the dimuon candidate for the event.

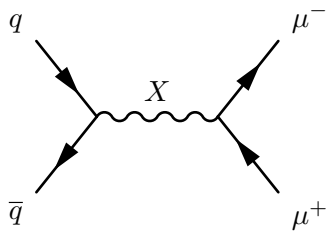

Figure 4.1: Example of a process which produces a neutral boson, X, in the intermediate state, and gives a dimuon final-state.

4.2 Experimental data

The data considered in this analysis consist of events where the LHC operated with stable beams and all relevant subsystems of ATLAS were operational. The events were produced by pp collisions at $\sqrt{s} = 8$ TeV during period B of data-taking in 2012. This corresponds to an integrated luminosity of about 5.1 fb^{-1}, calculated by the ATLAS luminosity calculator, where the GRL listed in the appendix and the two single muon triggers used in this analysis are accounted for. In total, 20.5 fb^{-1} of data was recorded in the dimuon channel during the 8 TeV runs in 2012, but only period B has been converted to the new EDM, i.e. the xAOD format, and hence was the only period that could be consider for this analysis, making use of the new analysis framework for Run 2.

In order for an event to be recorded, it needs to fire at least one of the many triggers that are available in ATLAS. This analysis intends to use events that passed at least one of two muon EF-triggers with p_{T}-thresholds of 24 GeV and 36 GeV, where the former has an isolation requirement. As mentioned earlier, the trigger information was not present in the 8 TeV data samples, and the triggers were instead emulated at the analysis level.

4.3 Background estimation

This analysis is concerned with search for new heavy bosons that may be produced in interactions such as $q\bar{q} \to X \to \mu^+\mu^-$, illustrated in Fig. 4.1, where X can represent an undiscovered particle or any other particle allowed by conservation laws. Even though we know the momentum of the colliding protons quite accurately, the quarks and anti-quarks that make up the protons can each take a wide range of momenta, and it is the quarks that go into the mentioned interaction. Hence, many particles and processes of different masses/energies can take the place of X, and by considering each event separately we can not with certainty determine which intermediate particle or particles decayed to the two muons measured in the detector. The distribution of signals that are identical in signature, but are coming from particles or processes we are not interested in, are referred to as background signals.

To estimate the background from known particles and processes, simulated Monte Carlo (MC) samples are considered for the most important contributions to the dimuon channel in the search region. The particles generated in these samples are in addition going through a full simulation of interactions with the ATLAS detector and its response to these interactions [27], based on GEANT4 [28], to make the reconstructed objects (particles) in the samples appear very much alike the real particles observed in experiments. The goal is to obtain an invariant mass distribution that matches the experimental data for mass regions lower than where one expects to find a new heavy particle, and which can be used to separate a potential resonance, caused by a new particle, from the expected background.

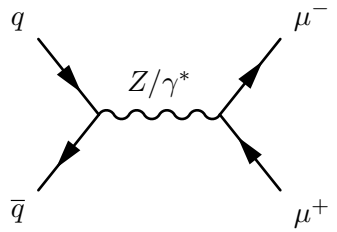

Figure 4.2: The Drell-Yan background process.

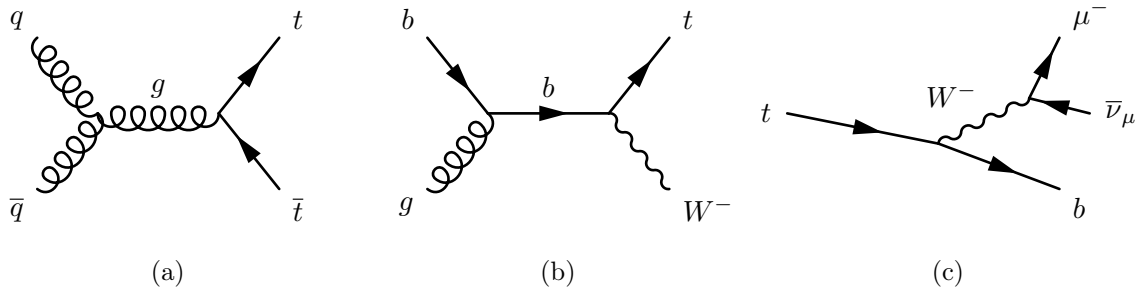

Figure 4.3: Examples of top quark background processes; (a) $t\bar{t}$, (b) single top in the Wt channel and (c) the subsequent decay of a top quark giving a muon in the final-state.

4.3.1 Processes

The most important background for high-mass dimuon search is the Drell-Yan process, $q\bar{q} \rightarrow Z/\gamma^* \rightarrow \mu^+\mu^-$, shoen in Fig. 4.2, where the intermediate particles produced in the $q\bar{q}$-interaction are the electrically neutral Z^0, with rest mass $m_Z = 91.2$ GeV, and the massless photon, γ. The star indicates that the photon being produced is a virtual (non-physical) particle, which is allowed to occur in such short-time processes due to Heisenberg's uncertainty relation, and is produced "off-shell", meaning with an unphysical mass. The Z can also be produced off-shell, and contributes all the way up to the highest dimuon invariant masses coming from the Drell-Yan process.

The second most significant background is coming from processes where a $t\bar{t}$-pair is produced. This can happen through many different kinds of interactions, e.g. $q\bar{q} \rightarrow g \rightarrow t\bar{t}$ or $gg \rightarrow g \rightarrow t\bar{t}$, where g denotes a gluon. The $t\bar{t}$-pair can further produce a $\mu^+\mu^-$-pair, where the top quark can produce a bottom quark along with a W^+ by $t \rightarrow b + W^+$, and the W boson can decay to an anti-muon and a muon-neutrino through $W^+ \rightarrow \mu^+ + \nu_\mu$. If the anti-top quark decays in the same way, except that all particles are interchanged by their antiparticles, we end up with two muons with opposite charges in the final state.

Another, and less significant, contribution from top quarks is also considered, namely from single-top production in the Wt-channel, e.g. $b + g \rightarrow b \rightarrow W + t$. The top quark will then most likely decay to a b-quark and a W, giving two W bosons in total in the event, where each can decay to a muon and a neutrino.

There are also contributions from diboson production to the background, i.e. interactions producing two bosons, which further can decay to muons. This can happen by $q + \bar{q}' \rightarrow \gamma/Z/W \rightarrow W/Z + W/Z$, where the prime represents that the initial state quarks have different flavor in the case of a W in the intermediate state. The final state can give either WW, WZ or ZZ. The Z can then decay to a $\mu^+\mu^-$-pair, and the W can produce a muon as mentioned above, which would give more than two muons in the event.

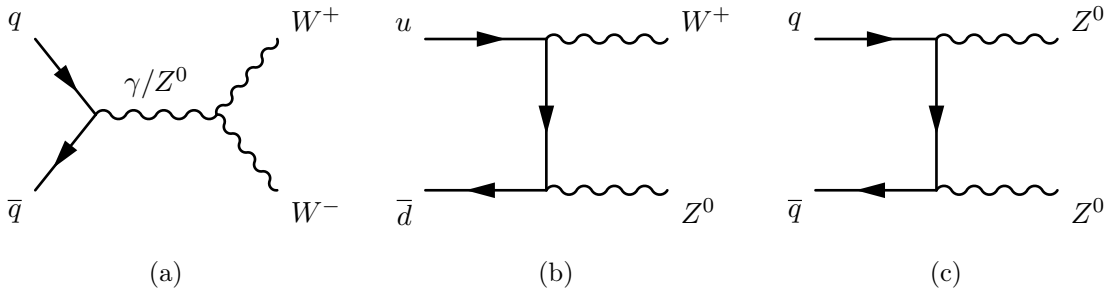

Figure 4.4: Examples of diboson production; (a) WW, (b) WZ and (c) ZZ.

Table 4.1: Information on the generators used to produce the simulated samples.

Process	Generator	Parton shower	PDF
Drell-Yan	POWHEG	PYTHIA 8.170	CT10
$t\bar{t}$, Wt	POWHEG	PYTHIA 6.426.2	CTEQ6L1
Diboson	POWHEG	PYTHIA 8.165	CT10
Z'	PYTHIA 8.163	PYTHIA 8.163	MSTW2008LO

There can in addition be contributions from jets to the background. This includes direct production of dijets in the pp collisions via the strong interaction, and subsequent decays of dibosons into quarks, which will then hadronize to give jets. Hadrons in the jets then have the possibility to produce muons through the electromagnetic interaction, or through decays by the weak interaction. Jets can also trick the reconstruction into building fake muon tracks. The dijet background to the dimuon channel was in the 8 TeV publication estimated from data, by reversing the isolation requirement on the variable $\sum_{\text{trk}} p_{\text{T}}^{\text{trk}}(\Delta R < 0.3)/p_{\text{T}}^{\mu}$ applied in the muon selection. This means to look at the contribution from muons passing all selection criteria, but in this case requiring the isolation fraction to be > 0.05 instead of < 0.05. The full treatment is explained in Ref. [29]. It was found that the contribution from dijets to the background was negligible, and was not considered for the publication. Hence, it is not included in this thesis either.

4.3.2 Monte Carlo samples

All background estimation included in this analysis is based on Monte Carlo (MC) simulation of the relevant processes, described in the previous section. These MC samples are provided centrally by ATLAS. The generators and parton distribution functions (PDFs) used to simulate the background and the Z' signal samples, are listed in Table 4.1.

The Drell-Yan sample has been generated with the POWHEG generator [30], at next-to-leading order (NLO) in perturbation theory, where PYTHIA 8 [31] was used for simulating parton showering and hadronization, with the PDF CT10 [32]. It contains simulation of the process $Z/\gamma^* \to \mu^+\mu^-$, with dimuon invariant masses larger than approximately 60 GeV.

Table 4.2: Information on the simulated Drell-Yan and top quark samples.

Process	MC run	σ_{gen} [pb]	ϵ_{F} [%]	N_{evts}
$Z/\gamma^* \to \mu\mu$	147807	1109.9	100.000	19,973,400
$t\bar{t} \to lX$	117050	210.85	54.298	29,865,600
$Wt \to X$	110140	20.461	100.000	4,992,100

The top quark samples, namely $t\bar{t}$ and single top in the Wt-channel, have also been simulated at NLO with the POWHEG generator, but made use of PYTHIA 6 [33] along with the CTEQ6L1 PDF [34], at leading order (LO) in perturbation theory, for parton showering. The simulated top quark and Drell-Yan samples are summarized in Table 4.2. For the $t\bar{t}$-sample, a lepton filter has been applied on the generator level, requiring at least one lepton per event coming from a W boson, which in turn has come from a top quark, for an event to be stored. Since a W also can decay to hadrons, the cross-section of leptonic production from $t\bar{t}$-processes, in the generated sample, will be too high compared to the real cross-section of $t\bar{t}$ to leptons. A filter efficiency, ϵ_{F}, of 54.298 %, is given for the sample, which can be used to correct the cross-section stated by the generator, σ_{gen}, back to the real cross-section for the process: $\sigma_{\mathrm{real}} = \epsilon_{\mathrm{F}} \times \sigma_{gen}$.

The Drell-Yan and top background samples considered for this 8 TeV analysis, are derivation samples (DxAODs called STDM3) produced by the SM working group. Even though this work is concerned with exotic searches, these derived samples, made for analyses of SM processes, still contain the sufficient objects and information needed in this case. The cuts which have been made in the derivation process, ensure that these samples contain events with at least 2 muons with $p_{\mathrm{T}} > 15$ GeV and $|\eta| < 2.6$. These cuts are looser than the ones applied in the analysis, and thereby will all the muons which pass the event selection in the analysis also have passed the selection in the production of the samples.

For the diboson background, the ZZ- and and the WW-samples have been generated with one specific final state per sample. The ZZ-samples include the processes $ZZ \rightarrow 2l + 2l'$, $ZZ \rightarrow 4l$ and $ZZ \rightarrow ll\nu\nu$, where $l = e^{\pm}, \mu^{\pm}, \tau^{\pm}$, the prime denotes a different lepton flavor than the unprimed lepton, and where the combinations of leptons and neutrinos satisfy the conservation laws on quantum numbers. In these samples the dileptons have been produced with invariant masses of $m_{ll} > 4$ GeV, and for those that contain four leptons, there has in addition been applied a dilepton filter of $p_{\mathrm{T}} > 5$ GeV. The 8 TeV publication by ATLAS also used diboson samples with lepton filters, i.e. not requiring any contribution from hadrons.

The WW-samples contain the processes $W^+W^- \rightarrow ll\nu\nu$, where the leptons may or may not be of the same flavor. No filters have been applied for these samples.

For the WZ-samples one set of samples has been produced for $W^+Z \rightarrow 3l + X$, where dilepton filters of $p_{\mathrm{T}} > 5$ GeV and $|\eta| < 2.7$ have been applied, and X denotes any other particles coming out of the event generation. Another set of samples has been produced for $W^-Z \rightarrow 3l + X$.

All diboson samples have been generated at NLO with POWHEG and PYTHIA 8, with the CT10 PDF. Information on the simulated diboson samples is given in Table 4.3.

In addition, all background samples, i.e. the Drell-Yan, top and diboson samples, have made use of PHOTOS [35] for handling final-state photon radiation, and GEANT for simulation of the particles' interactions with the ATLAS detector.

Information on how the MC samples have been produced, along with their cross-sections, number of events, etc., have been found in the ATLAS Metadata Interface (AMI)[1].

4.4 Z' signal samples

There have also been produced Monte Carlo-simulated samples for Z' signals, based on theoretical models. Signal samples based on the sequential Standard Model (SSM) Z', which is basically a heavier copy of the SM Z-boson, with similar couplings to the SM fermions, have been considered as benchmark for this analysis. The samples have been generated with PYTHIA 8 and the MSTW2008LO PDF [36], at leading order in perturbation theory. They contain simulated

[1] Access to this information is restricted to members of the ATLAS collaboration.

Table 4.3: Information on the simulated diboson samples.

Process	MC run	σ_{gen} [pb]	ϵ_{F} [%]	N_{evts}
$W^+W^- \to \mu e + X$	126939	0.597260	100.000	399,700
$W^+W^- \to \tau e + X$	126930	0.597490	100.000	399,300
$W^+W^- \to e\mu + X$	126931	0.597570	100.000	399,800
$W^+W^- \to \mu\mu + X$	126932	0.597400	100.000	199,800
$W^+W^- \to \mu\mu + X$	126933	0.597440	100.000	399,700
$W^+W^- \to e\tau + X$	126934	0.597190	100.000	399,700
$W^+W^- \to \mu\tau + X$	126935	0.597670	100.000	400,000
$W^+W^- \to \tau\tau + X$	126936	0.597440	100.000	200,000
$ZZ \to 2e + 2\mu$	126938	0.17561	82.791	299,800
$ZZ \to 2e + 2\tau$	126939	0.17535	58.245	299,800
$ZZ \to 4\mu$	126940	0.076848	91.176	299,600
$ZZ \to 2\mu + 2\tau$	126941	0.17542	58.861	299,700
$ZZ \to 4\tau$	126942	0.076850	10.524	100,000
$ZZ \to \mu\mu\nu\nu$	126950	0.054310	100.000	99,900
$ZZ \to \tau\tau\nu\nu$	126951	0.054310	100.000	100,000
$W^-Z \to e^- + e^+e^- + X$	129477	1.568	29.374	99,800
$W^-Z \to e^- + \mu^+\mu^- + X$	129478	0.930860	35.103	100,000
$W^-Z \to e^- + \tau^+\tau^- + X$	129479	0.174970	16.735	99,900
$W^-Z \to \mu^- + e^+e^- + X$	129480	1.366	29.249	100,000
$W^-Z \to \mu^- + \mu^+\mu^- + X$	129481	0.952110	35.114	100,000
$W^-Z \to \mu^- + \tau^+\tau^- + X$	129482	0.174970	16.841	100,000
$W^-Z \to \tau^- + e^+e^- + X$	129483	1.367	14.262	98,800
$W^-Z \to \tau^- + \mu^+\mu^- + X$	129484	0.930940	18.219	100,000
$W^-Z \to \tau^- + \tau^+\tau^- + X$	129485	0.172140	5.9467	100,000
$W^+Z \to e^+ + e^+e^- + X$	129486	0.962000	29.631	99,900
$W^+Z \to e^+ + \mu^+\mu^- + X$	129487	0.629320	35.307	96,000
$W^+Z \to e^+ + \tau^+\tau^- + X$	129488	0.112800	15.913	99,900
$W^+Z \to \mu^+ + e^+e^- + X$	129489	0.930360	29.645	100,000
$W^+Z \to \mu^+ + \mu^+\mu^- + X$	129490	0.644790	35.389	100,000
$W^+Z \to \mu^+ + \tau^+\tau^- + X$	129491	0.112800	15.983	99,900
$W^+Z \to \tau^+ + e^+e^- + X$	129492	0.930440	14.748	100,000
$W^+Z \to \tau^+ + \mu^+\mu^- + X$	129493	0.629420	18.691	100,000
$W^+Z \to \tau^+ + \tau^+\tau^- + X$	129494	0.111100	5.6674	99,900

Table 4.4: Information on the simulated Z' signal samples.

Process	MC run	σ_{gen} [pb]	N_{evts}
SSM $Z' \to \mu\mu$, $m_{Z'} = 1.5$ TeV	158027	0.019420	24,000
SSM $Z' \to \mu\mu$, $m_{Z'} = 2$ TeV	158028	0.003448	23,500
SSM $Z' \to \mu\mu$, $m_{Z'} = 2.5$ TeV	158029	0.000747	24,000

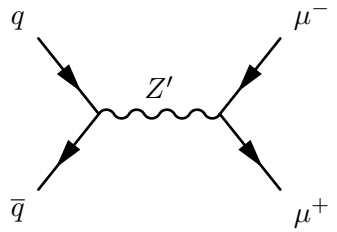

Figure 4.5: Feynman diagram of the process simulated in the Z' signal samples.

signals of the process $Z' \to \mu^+\mu^-$, illustrated in Fig. 4.5 at three different pole-masses for the Z': 1.5, 2 and 2.5 TeV. The signal samples are summarized in Table 4.4.

Such signal samples can be used to study detector acceptance and analysis efficiencies for model-specific searches, and also in statistical analyses for setting exclusion limits on the mass of the corresponding particles. In this analysis they are only considered as references to what a potential signal might look like in the invariant mass spectrum.

4.5 Comparison of data and estimated background

The experimental data is compared to the summed contribution from all the considered SM background processes. The different Monte Carlo samples are scaled according to their relative contribution to the total estimate. This can be done by normalizing each sample to its corresponding integrated luminosity, and then multiply it with the integrated luminosity of the experimental data.

The corresponding integrated luminosity of a sample is given by $L_{\text{MC}} = N_{\text{evts}}/\sigma_{\text{MC}}$, where N_{evts} is the number of events in the full xAOD (before any cuts applied to reduce the size of the sample, e.g. for production of DxAODs), and σ_{MC} is the cross-section for the process considered in the sample. For simulated samples without any filters applied, σ_{MC} is equal to the cross-section reported by the generator, σ_{gen}. On the other hand, if the sample has been filtered in some way, one needs to account for the filter efficiency, ϵ_{F}, in order to get the correct cross-section for the normalization. This is found by $\sigma_{\text{MC}} = \epsilon_{\text{F}} \times \sigma_{\text{gen}}$.

4.5.1 Invariant mass distribution

The resulting invariant mass distribution of the experimental data compared to the estimated background, is shown in Fig. 4.6a. Overlaid are also simulated SSM Z' signals for three different pole-masses, which are added for reference, to show what one expects new resonances to look like, if they were to come from an SSM Z'. The lower part of the figure shows a plot of the ratio of number of events observed in the data divided by the expected number of events from SM background processes. The error bars on the data points and the grey filled area in the ratio plot, show the statistical error of the data and estimated background, respectively. These statistical errors are calculated by a function in ROOT, and represent the square-root of the

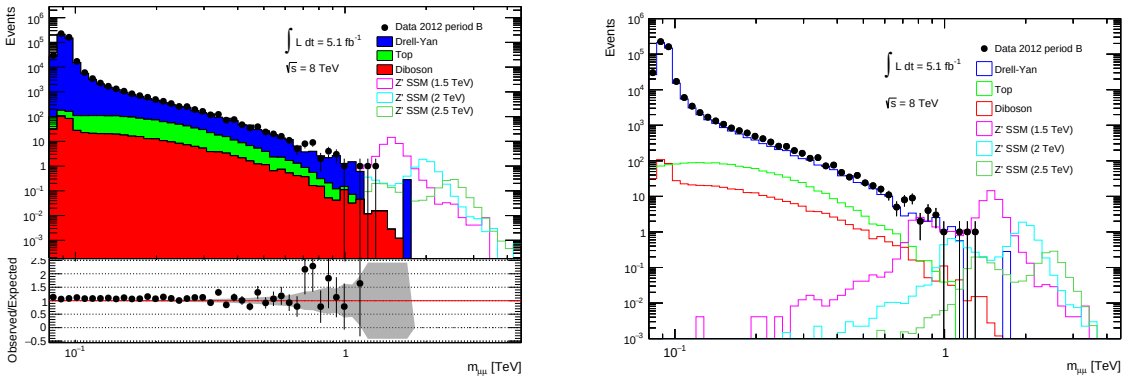

(a) (b)

Figure 4.6: Dimoun invariant mass distributions of data compared to (a) the stacked sum of backgrounds and (b) each background process plotted separately to show their relative contributions to the total estimate. Simulated Z'_{SSM} signals are overlaid. The error bars denote the statistical uncertainty of the data points, while the grey filled area denotes the statistical uncertainty of the stacked backgrounds.

sum of squared weights of samples contributing for each bin in the histogram. The bin width of the histogram is constant in $\log m_{\mu\mu}$, as was chosen in the ATLAS publication on dilepton resonance search at 8 TeV [19]. This paper states that this binning was chosen such that a possible signal peak would span multiple bins, and that the shape would not be impacted by statistical fluctuations at high mass. The y-axis shows the number of dimuon candidates passing the selection criteria, where only one dimuon candidate is selected per event, namely the one with the highest $m_{\mu\mu}$.

The expected background from SM processes seems to be in good agreement with the observed data, in the regions with considerable statistics. Up to about 300 GeV, the data is within 10 % of the background expectations. At higher mass, the fluctuations get bigger, but so do the statistical uncertainties. There are two distinct outliers in the region 700-800 GeV, but these data-points correspond to about 10 events, which gives low statistical significance. The error bars for these data-points are also within the uncertainty of the background, though barely, which makes it possible to argue that they are merely statistical fluctuations of insufficient significance. The four data-points with the highest invariant masses, at around 1-1.2 TeV, hold only one dimuon candidate each.

Fig. 4.6b shows a plot where each of the three groups of background processes, namely the Drell-Yan, top quark and diboson contributions, are not summed (stacked), but are plotted separately to give a clearer view of the relative contribution from each background process. We can see that the Drell-Yan process is by far the most important contribution to the background in the plotted invariant mass range (> 80 GeV). It follows the line shape and magnitude of the data closely for the whole spectrum, and is, naturally, especially contributing around the Z-peak compared to the other processes. The second most important background process, except maybe at the Z-peak where dibosons contribute slightly more, comes from the $t\bar{t}$ and Wt-production. These processes do not give a peak at the Z-mass, because the measured muons coming from such top quark processes are uncorrelated and will not have had Z bosons in the intermediate state, in contrast to the background from Drell-Yan and dibosons. The contribution from diboson production is also significant to the background for dimuon final states, but as we can see from the plot, it is, except at the Z-peak, less important than the top quark contribution for the

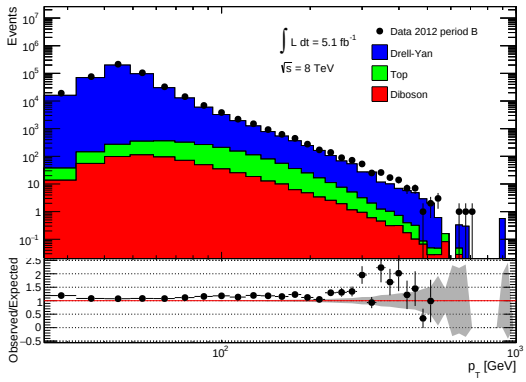

(a) Leading muon.

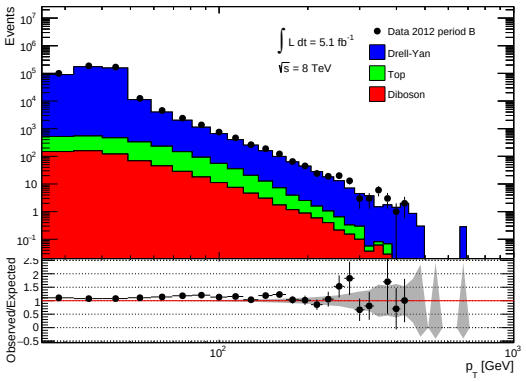

(b) Subleading muon.

Figure 4.7: Transverse momentum of the leading and subleading muons of the dimuon candidates. The error bars denote the statistical uncertainty of the data points, while the grey filled area denotes the statistical uncertainty of the stacked backgrounds.

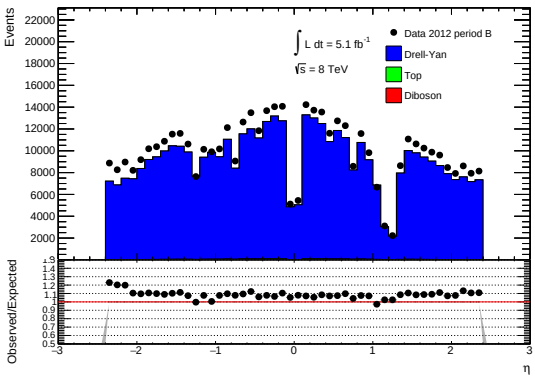

(a) Leading muon.

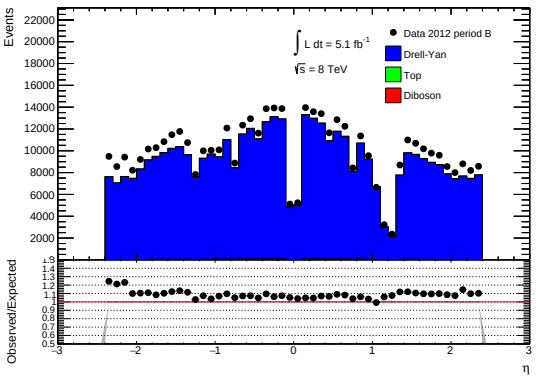

(b) Subleading muon.

Figure 4.8: Pseudorapidity of the leading and subleading muons of the dimuon candidates. The error bars denote the statistical uncertainty of the data points, while the grey filled area denotes the statistical uncertainty of the stacked backgrounds.

region up to about 1 TeV, where the two seem to be of more equal importance.

4.5.2 Kinematic properties

The observed transverse momentum (p_{T}) distributions for the leading muon, the one with the highest p_{T}, and the subleading muon, the one with the lowest p_{T} in the dimuon candidate, is compared to the total sum of estimated background contributions, in Figs. 4.7a and 4.7b, respectively. The behavior of the data seem to be well explained by the simulated samples up to about 110-120 GeV, from where the statistics start to get low. Both plots show a peak at 40-50 GeV, which is around half the mass of the Z boson. This probably means that both muons in the pair have similar p_{T} and carry around half of the energy of the intermediate Z each, from which they most likely have been produced. As expected, both the maximum and mean value of the p_{T}-distributions seem to be higher for the leading muons than for the subleading.

Figs. 4.8a and 4.8b show the compared data and background distributions of the pseudorapidities (η) of the leading and subleading muons, respectively. The distinct drops in the

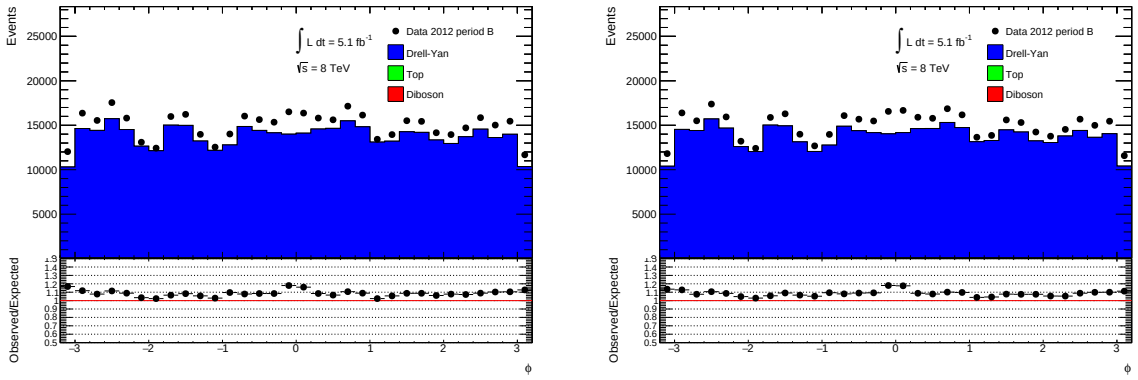

(a) Leading muon.

(b) Subleading muon.

Figure 4.9: ϕ-distributions of the leading and subleading muons of the dimuon candidates.

distributions close to η values of 0 and 1.2, are caused by "cracks" in the muon detector coverage, where η of 1.2 is close to the transition region between the barrel and the end-cap. Such drops may also be caused by non-operational detector layers, which may explain the asymmetry of the drops in entries near η values of 1.2 and -1.2. The shape of the observed η-distributions are in good agreement with the expectations, but are consequently lying about 10 % above the background. The data and background thus seem to differ by a factor, which may be corrected by applying higher-order corrections to the generator cross-sections, pile-up and event weights, among others, in a more detailed analysis like the one performed in the 8 TeV publication, as discussed in Sec. 4.6.

The corresponding ϕ-distributions for leading and subleading muons are shown in Figs. 4.9a and 4.9b The plots should show eight "dips" in the distributions, because of the eight toroid magnets situated equidistantly around the whole 2π ϕ range. This is not completely the case in these plots, where only five of these are prominent. The data and background show the same behavior, except close to $\phi = 0$, where the background has less entries than the neighboring bins, while the opposite is the case for the data. However, the magnitude of the fluctuation is not larger than the overall deviation of the data from the background, and could thus be a fluctuation that would disappear in a more detailed analysis. Similar to the η-distributions, the data points lie consistently above the background also in the ϕ-plots, which probably have the same explanations as mentioned for η.

4.6 Comparison with the ATLAS publication at $\sqrt{s} = 8$ TeV

This analysis has been based on the published analysis regarding search for high-mass dilepton resonances with the ATLAS detector, at a center-of-mass energy of $\sqrt{s} = 8$ TeV and with an integrated luminosity of 20.5 fb^{-1} in the dimuon channel [19]. However, since this analysis is carried out in the new event data model for use in Run 2, and with limited time available, there are some differences between the two approaches. In this section, these two analyses will be compared, and differences and similarities will be discussed. The support note[2] for the publication has been used to get additional information.

[2]Source: `https://cds.cern.ch/record/1564935/files/ATL-COM-PHYS-2013-1033.pdf?` (access limited to members of the ATLAS collaboration)

4.6.1 Data and Monte Carlo samples

As a result of performing this analysis in the new EDM, a number of samples, dataset information and tools used in the published analysis have not been made available for the new format, or are still work in progress. This has been the case for many of the data and MC samples used in the official analysis. Only data from period B in 2012 is available in the xAOD format, corresponding to about 25 % of the total amount of data taken during the 8 TeV run. For the background samples, only the unbinned Drell-Yan sample has been reprocessed into xAOD, out of the samples considered in the publication. Thus, other samples, produced with different generators, were used instead, but seem to cover the same processes, though with lower statistics.

In the published analysis, binned Drell-Yan samples were generated both for background estimation, but also for the SSM Z' signal, which were reweighted to give the correct shape for the resonances. The signal samples considered for this thesis are unbinned samples, which do not need reweighting to match the theoretical line shape of the resonances. The reweighted binned signal samples, however, have higher statistics, and are hence better suited for use in a statistical analysis, e.g. in setting mass-limits. Since a statistical study is not considered in this thesis, the unbinned samples are sufficient in this case.

To increase the statistics at higher invariant masses, additional simulated samples were also generated for the WW, WZ and ZZ processes. These were "fast simulations", meaning that the events were not fully simulated, but e.g. use a parametrization of the calorimeter response, and other approximations, to make the simulations less time consuming. Two samples were generated for each of the mentioned diboson contributions, one including at least one dimuon pair with a true invariant mass between 400 and 1000 GeV, and one with true invariant masses above 1000 GeV. For the $t\bar{t}$ process, a fit to the line shape of the simulated sample was obtained, to extrapolate the expected number of events from this process to higher masses. These procedures were not considered for the anlysis in this thesis, since the samples were not available in the xAOD format, and adding the extrapolation to the $t\bar{t}$ process was not considered worthwhile w.r.t. the focus of the thesis.

The trigger information has not been available in the 8 TeV samples, and the alternative approach of emulating this selection has been performed instead, as explained in Sec. 4.1.1.

4.6.2 Higher-order corrections to cross-sections

The Monte Carlo-simulated samples are typically generated using cross-sections correct to leading order (LO) or next-to-leading order (NLO) in perturbation theory. In the published analysis, there were carried out separate cross-section calculations to higher order, which were used to correct the cross-sections reported by the generators in terms of K-factors. For a correction from NLO to NNLO (next-to-next-to-leading order) the K-factor is given by $K_{\mathrm{NNLO}} = \sigma_{\mathrm{NNLO}}/\sigma_{\mathrm{NLO}}$, where σ_{NNLO} and σ_{NLO} are the cross-sections at NNLO and NLO, respectively.

The corrections to the Drell-Yan cross-section were applied in terms of mass-dependent K-factors, where the higher-order cross-section is dependent on mass. QCD corrections to NNLO were applied to the NLO cross-section of the generated POWHEG sample, along with corrections from electroweak process, photon-induced background ($\gamma\gamma \to \mu^+\mu^-$) and from real W/Z radiation (a final-state charged muon radiates a real W or Z). The K-factors used for dimuon invariant masses of 1, 2 and 3 TeV, were calculated to be 1.07, 1.10 and 1.14, respectively.

For the top quark and diboson samples, there was calculated a single higher-order cross-section for each sample, i.e. mass-independent corrections to the generator cross-sections, where the top samples were corrected from NLO to NNLO and the diboson samples from LO to NLO. Because the diboson samples considered in this thesis are generated at NLO, they are already at the same order as the corrected samples in the publication. The $t\bar{t}$ samples in the two

analyses, however, are produced by different generators, and it is not obvious that the higher-order correction calculated for the sample in the published analysis, is applicable to the one used in this thesis, due to filters applied to the samples, etc. Hence, higher-order corrections are not considered for the $t\bar{t}$ sample, nor is it for the Wt sample, because of its relatively low contribution in the first place.

4.6.3 Muon selection

To ensure good resolution on the measurement of muon momentum, the muons are in both analyses required to cause at least three hits in three muon detector layers (stations), which are referred to as three-station muons. The published analysis is even more stringent, in also requiring one phi hit in two different RPC/TGC/CSC layers (the trigger chambers), no hits in the BEE or BIS78 MDT chambers, and for each muon, that the difference between the standalone p_{T} measurements from the ID and MS must not exceed five times the sum in quadrature of the standalone uncertainties. Such muons have a p_{T} resolution at 1 TeV ranging from 19 % to 32 %, depending on η. In addition, muons which did not pass the three-station requirements, but instead fulfilled $|\eta| < 1.05$, made at least five hits in each of the inner and outer barrel MDT layers and at least one hit in one of the RPC trigger layers, were also selected, and referred to as two-station muons. The corresponding p_{T} difference significance should not exceed three times the sum in quadrature of the standalone uncertainties, in this case. These muons have slightly worse p_{T} resolution compared to the three-station muons, but increase the acceptance by a few percent at high mass.

The reason for the simpler three-station muon selection in this thesis, is that the muon selection tool for use in the new EDM has not implemented all the features that was available in the previous EDM (yet), and that the trigger decision information in the samples are lacking. The additional two-station muon selection is not considered, since it is not implemented in the muon selection tool, and that it makes the selection more complicated, with a relatively low gain in the total acceptance and efficiency.

In this thesis, the two muons with the highest p_{T} scalar sum and with opposite charge, are chosen to form the dimuon candidate for each event. The official analysis, however, has two ways of selecting dimuon candidates. If there are two three-station muons with opposite charge in an event, they are said to pass the "primary (or tight) dimuon selection". If there is no "primary dimuon candidate", but there are one three-station and one two-station muon with opposite charge in the event, they are said to pass the "secondary (or loose) dimuon selection". In both cases, if there are more than one dimuon candidate in the event, the one with the highest p_{T} scalar sum is chosen. The product of acceptance (due to detector geometry) and efficiency (level of correct particle identification) was estimated to be 46 % in the dimuon channel, at a Z'_{SSM} mass of 2 TeV, where about 42 % came from the primary dimuon selection and about 4 % from the secondary dimuon selection.

4.6.4 Momentum resolution and smearing

The muon momentum resolution in the ID and MS, at high transverse momentum, can be parametrized as

$$\frac{\sigma(p_{\mathrm{T}})}{p_{\mathrm{T}}} = P_1 \oplus P_2 \cdot p_{\mathrm{T}}, \tag{4.3}$$

where $\sigma(p_{\mathrm{T}})$ is the standard deviation of the p_{T} resolution, and P_1 and P_2 are resolution parameters related to multiple scattering and intrinsic curvature resolution, respectively. The expression is dominated by P_2 at very high p_{T}. An MCP tool can be used to correct the muon

p_{T} in MC to look like the muon p_{T} in data. A Gaussian smearing of the p_{T} measurements in the ID and MS are then performed in terms of

$$\delta(q/p_{\mathrm{T}}) = S_1 \cdot g_1 \cdot (q/p_{\mathrm{T}}) + S_2 \cdot g_2, \tag{4.4}$$

where q is the charge of the particle responsible for the track, g_1 and g_2 are random Gaussian variables with zero mean and unit rms, and S_1 and S_2 are smearing constants. The quadratic differences in the resolution parameters, between data and simulation, are used to determine these smearing constants, given by $S_i = P_i^{\mathrm{data}} \ominus P_i^{\mathrm{MC}}$.

These corrections were for the published analysis shown to have an effect of about 1 % on the invariant mass estimates, and are hence considered small enough to be neglected for the thesis analysis.

4.6.5 Systematic uncertainties

Since this thesis is concerned with already analyzed data, which is only a subset of that considered in the publication, the focus is on data-handling in the new EDM, in addition to preparation for Run 2, and hence a detailed statistical analysis is not carried out in this case. The publication, on the other hand, performed a full statistical analysis to set mass-limits on new particles for several theoretical models, since no new resonances were found in the search. To make the analysis insensitive to the uncertainty on the measurement of the integrated luminosity, and other mass-*independent* systematic uncertainties, the estimated backgrounds were normalized to the data in the region of the Z peak (80-110 GeV). The scale factor was found to be 0.98 for the dimuon channel. This normalization procedure is not done in this thesis, since a full statistical analysis is not performed, but the corresponding scale factor has been calculated to be approximately 1.05. The scale factor is calculated by integrating the number of entries in the histogram bins from 80 to 110 GeV, for both data and background, and dividing the contribution from data by the contribution from the backgrounds, in the normalization region. A mass-independent systematic error of 4 % was assigned to the signal expectation, due to NNLO corrections to the Drell-Yan cross-section in the normalization region. Systematic uncertainties found to be less than 3 % on the observed number of events for all $m_{\mu\mu}$, were neglected by the publication, which argued that such uncertainties had negligible impact on the search.

Mass-*dependent* uncertainties comprise theoretical and experimental effects on both signal and background, which are correlated across all $m_{\mu\mu}$ bins in the search region. Theoretical mass-dependent uncertainties were only applied to the Drell-Yan background expectation. These are uncertainties due to higher-order corrections to the Z/γ^* cross-section, including variation and choice of PDF, uncertainties in the calculation of the strong coupling, α_{s}, and electroweak and photon-induced corrections. An experimental uncertainty on the beam energy was estimated to be 0.65 %. The effect of this uncertainty on the background was only considered for the dominant Drell-Yan process, which was found to be 3 % for high dimuon masses. The effect was found to be less than 1 % for the signals considered, and was hence deemed negligible.

Muons with large energy loss due to bremsstrahlung in the outer part of the calorimeter, may interfere with the muon reconstruction in the MS, and give rise to inefficiencies. Such events are, however, rare, and the corresponding systematic uncertainty is small enough to be neglected in the mass range considered. The combined uncertainty on the trigger and reconstruction efficiencies was found to be negligible. Still, residual misalignment in the MS affect the steeply falling background, and the line shape of signals, at high dimuon mass. This uncertainty on the resolution was estimated to be 3 % at $m_{\mu\mu} = 2$ TeV and 8 % at $m_{\mu\mu} = 3$ TeV for the background estimate, and to be negligible for signal. The mass-dependent systematic uncertainties considered in the publication, are listed in Figs. 4.10a and 4.10b for dilepton invariant masses of 2 and 3 TeV, respectively.

Source ($m_{\ell\ell} = 2$ TeV)	Dielectrons		Dimuons	
	Signal	Background	Signal	Background
Normalization	4%	N/A	4%	N/A
PDF variation	N/A	11%	N/A	12%
PDF choice	N/A	7%	N/A	6%
α_s	N/A	3%	N/A	3%
Electroweak correction	N/A	2%	N/A	3%
Photon-induced correction	N/A	3%	N/A	3%
Beam energy	<1%	3%	<1%	3%
Resolution	<3%	<3%	<3%	3%
Dijet and W + jets	N/A	5%	N/A	N/A
Total	4%	15%	4%	15%

(a)

Source ($m_{\ell\ell} = 3$ TeV)	Dielectrons		Dimuons	
	Signal	Background	Signal	Background
Normalization	4%	N/A	4%	N/A
PDF variation	N/A	30%	N/A	17%
PDF choice	N/A	22%	N/A	12%
α_s	N/A	5%	N/A	4%
Electroweak correction	N/A	4%	N/A	3%
Photon-induced correction	N/A	6%	N/A	4%
Beam energy	<1%	5%	<1%	3%
Resolution	<3%	<3%	<3%	8%
Dijet and W + jets	N/A	21%	N/A	N/A
Total	4%	44%	4%	23%

(b)

Figure 4.10: Summary of the mass-dependent systematic uncertainties on the expected number of events, at dilepton masses of (a) $m_{ll} = 2$ TeV and (b) $m_{ll} = 3$ TeV, where N/A indicates that the uncertainty is not applicable. Uncertainties < 3 % for all values of m_{ee} and $m_{\mu\mu}$ are neglected. Correspond to Tables III and IV in Ref. [19].

4.6.6 Invariant mass distribution

Since the publication at $\sqrt{s} = 8$ TeV corresponded to an integrated luminosity of 20.5 fb^{-1}, while the analysis in this thesis corresponds to about 1/4 of this, namely 5.1 fb^{-1}, the invariant mass spectra from these analyses are not directly comparable. Hence, previously published results from ATLAS are also considered. In Figs. 4.11a [38] and 4.11b [39] the dimuon invariant mass distributions from the publication of $\sqrt{s} = 7$ TeV data with an integrated luminosity of 5.0 fb^{-1}, and the preliminary results of data taken at $\sqrt{s} = 8$ TeV with an integrated luminosity of 6.1 fb^{-1}, which was presented at the "32th International Symposium on Physics in Collision" conference in September 2012, are shown, respectively. The 7 TeV results correspond to approximately the same integrated luminosity as the data considered in this thesis, but taken during collisions at lower center-of-mass energy. The preliminary conferance results at 8 TeV, on the other hand, are taken at the same center-of-mass energy, but correspond to somewhat higher integrated luminosity, though still much closer to that of this thesis, than the final publication of 8 TeV data.

The event and muon selections for these two last mentioned analyses seem to be almost identical[3] to the final 8 TeV publication. The corresponding invariant mass distributions are very similar, where it is hard to see any differences in the Z/γ^* background, but the $t\bar{t}$ process seem to contribute a bit more to the background at 8 TeV, while the diboson processes seem to contribute slightly less, compared to at 7 TeV. Otherwise, the observed data follow the expected background nicely up to about 500 GeV, in both cases, where the fluctuations w.r.t. the background start to get more prominent. The highest measured dimuon mass is between 1 and 1.5 TeV for both the 7 and 8 TeV data.

In Fig. 4.11c the dimuon invariant mass distribution of the full 8 TeV data taken in 2012 is shown. It is not so easy to judge the relative contribution from each background process to the plots in Figs. 4.11a and 4.11b, because the stacking order is interchanged, in addition to the inclusion of the Wt process to the top quark contribution, for the full 8 TeV data. But what one can note, is that the number of entries has increased significantly in the latter, for all processes and measurements, due to the higher integrated luminosity, where the increase in the number of entries seem to be consistent with the increase in integrated luminosity, by approximately a factor of 4 for both. The highest measured dimuon invariant mass is in this case close to 2 TeV.

[3]The 7 TeV analysis used different triggers: one with a p_{T} threshold of 22 GeV, as reconstructed from the combined ID and MS measurements, and a second one with a p_{T} threshold of 40 GeV, as reconstructed by the MS in the barrel region only.

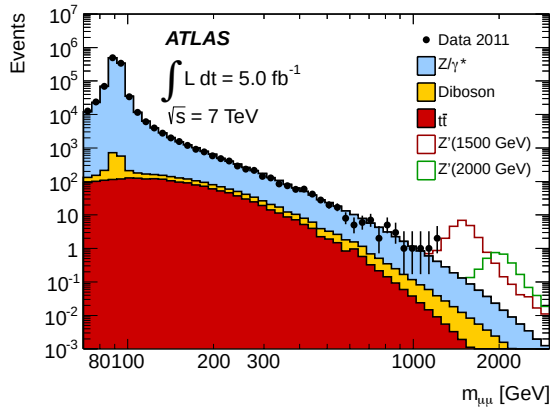

(a) From Ref. [38]

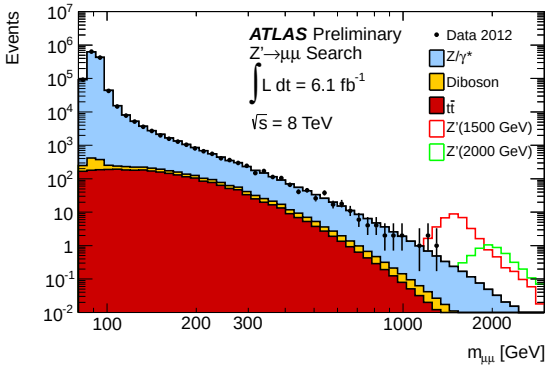

(b) From Ref. [39]

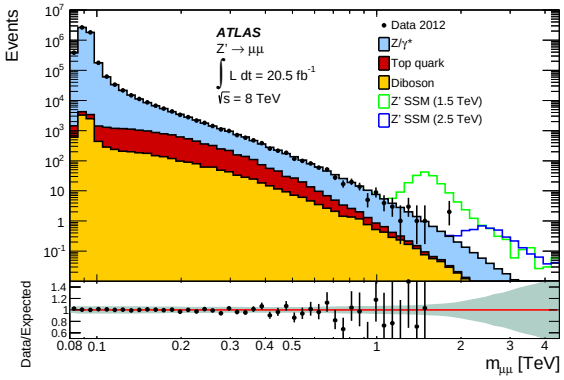

(c) From Ref. [19]

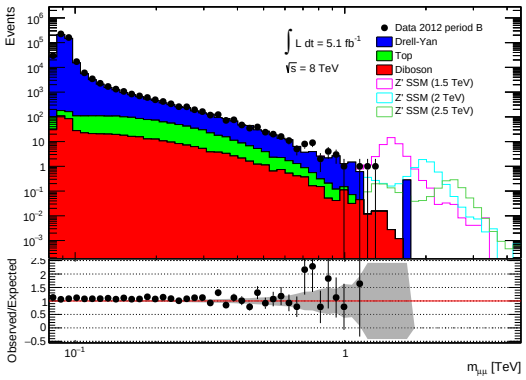

(d)

Figure 4.11: Dimuon invariant mass ($m_{\mu\mu}$) distributions of data compared to the stacked sum of expected background processes, with Z' signals overlaid; at different center-of-mass energies and integrated luminosities. In the three plots taken from ATLAS publications, (a)-(c), the error bars denote *systematic* uncertainties, while in the plot obtained in this thesis, shown in (d), the error bars denote *statistical* uncertainties.

Now, making the comparisons to the corresponding distribution obtained in this thesis, shown in Fig. 4.11d, the relative contributions from the different background processes seem to be approximately the same as in the full 8 TeV data, in Fig. 4.11c. Comparison with the relative contributions to the background in Figs. 4.11a and 4.11b is not trivial, due to the interchange of the stacking order, but because of the similar integrated luminosity, the observed data is more comparable to the two last mentioned plots, at 7 TeV and the preliminary 8 TeV results, respectively. The dimuon candidate with the highest invariant mass is in the analysis of this thesis observed in the region of 1-1.5 TeV, i.e. similar to the plots in Figs. 4.11a and 4.11b. The estimated background is maybe the most visible difference, where the analysis in the new EDM has much less statistics for high dimuon mass for all the considered background processes. Another difference, is that this analysis observes less events containing dimuon candidates, with about 2×10^5 observed events at the Z peak. This is compared to the 7 TeV results, with the most comparable integrated luminosity of 5.1 fb^{-1}, which observed about 5×10^5, and also the preliminary 8 TeV results with 6.1 fb^{-1}, with approximately 6×10^5 observed events at the Z peak. The omission of two-station muons may explain some of this deviation. Even though the two-station muons contribute less than 10 % to the signal selection at masses of order TeV, they may have a larger impact at lower invariant mass.

4.7 Angular distributions

Many different theories predict new neutral bosons, which may show up as new resonances in the dimuon invariant mass spectrum, but depending on the theory, the new particles may have different intrinsic spin. In R-parity violating supersymmetry, a scalar spin-0 sneutrino, $\tilde{\nu}$, can decay to an opposite-charge muon pair [40], and give rise to a new heavy dimuon resonance. A similar resonance can be caused by production of a Z', which is a spin-1 vector boson (see Sec. 1.7). In addition, a resonance may appear from production of a boson of spin-2, such as RS graviton excitations (see Sec. 1.7). If one were to measure such a resonance in the invariant mass spectrum, one would need to perform additional studies to find out which particle was actually produced.

To determine the spin of the new particle, one may look at the angular distribution of the muons contributing to the resonance. That is, to investigate the distribution of angles with which the negative (or the positive) muon is measured compared to one of the incoming quarks (the beam-line), in the center-of-mass frame, i.e. the frame where the intermediate particle is at rest. The angular distribution of the muons is dependent on the spin of the particle which has produced them. Due to the quantum mechanics of spin, some angles are preferred compared to others, depending on the spin of the decaying particle.

A spin-0 particle is called a scalar boson, because it has no direction associated with its spin. The result is that the produced muons have no preferred direction, and will be isotropically distributed.

Unlike a scalar particle, a particle of spin-1 *does* have a direction associated with its spin. Due to discrete helicity states of such a particle, spin aligned along, opposite or perpendicular to its direction of motion, there are certain angles or directions which the muons are more likely to be produced with. The partial cross-section w.r.t. $\cos\theta^*$ for the process[4] $q\bar{q} \to Z' \to \mu^+\mu^-$, where the star denotes the angle measured in the center-of-mass frame, is given by [40]

[4]I did the corresponding calculation for the electroweak case of $q\bar{q} \to \gamma, Z^0 \to l^+l^-$, including interference terms, as part of a project in the course FYS4560, and obtained the same angular dependence for the final-state leptons, since both γ and Z^0 are spin-1 vector bosons.

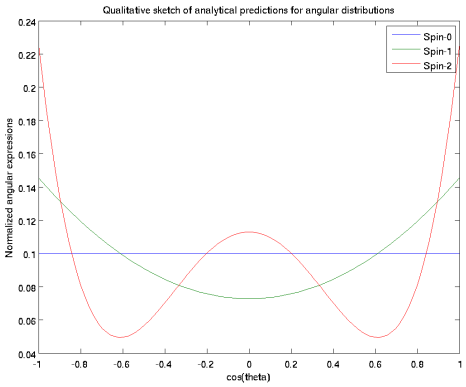

(a) Theoretical expressions for $q\bar{q} \to X \to l^+l^-$, where X denotes a spin-0 scalar, a spin-1 vector and a spin-2 RS graviton, in their respective cases.

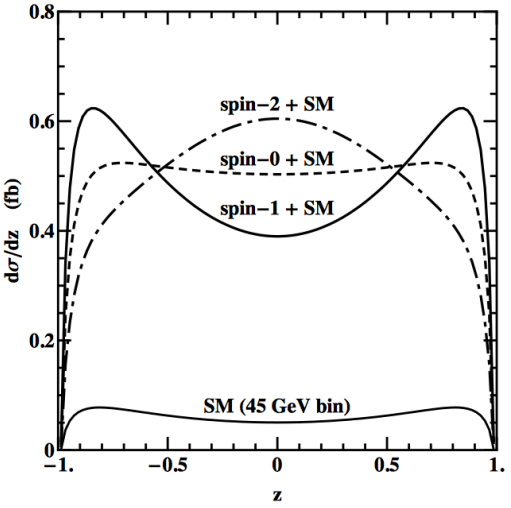

(b) Angular distributions of $pp \to X \to l^+l^-$, when taking detector cuts and different parton contributions into account, where $z \equiv \cos\theta^*$ and X denotes a spin-0 scalar, a spin-1 vector and a spin-2 RS graviton, in their respective cases. From Ref. [40].

Figure 4.12: Angular distributions of leptons in the dilepton center-of-mass system, when produced by bosons of spin-0, spin-1 and spin-2.

$$\frac{\mathrm{d}\sigma}{\mathrm{d}\cos\theta^*} \propto 1 + \cos^2\theta^*. \tag{4.5}$$

A spin-2 particle has five possible spin-alignments, corresponding to the z-component of the spin being 0, ± 1 or ± 2. This gives a more involved situation than for the spin-1 case. One can show that the partial cross-section w.r.t. $\cos\theta^*$, for the interaction $q\bar{q} \to G \to \mu^+\mu^-$, where G is an RS graviton, has the following angular dependence [40]

$$\frac{\mathrm{d}\sigma}{\mathrm{d}\cos\theta^*} \propto 1 - 3\cos^2\theta^* + 4\cos^4\theta^*. \tag{4.6}$$

The corresponding expression for gluon fusion production $gg \to G \to \mu^+\mu^-$, is $\mathrm{d}\sigma/\mathrm{d}\cos\theta^* \propto 1 - \cos^4\theta^*$, given by the same reference.

A visualization of the angular dependences in the three spin cases discussed above, is plotted in Fig. 4.12a. The independence on angle for spin-0 can be seen by the flat line, while for spin-1 and spin-2 there are two and three preferred angles, respectively. The figure shows a qualitative plot of the theoretical expressions given above, and will appear slightly different in real experiments. A more realistic plot of the angular dependences, taking into account the smearing due to the parton distributions, that different partons contribute with different weight to the different channels, and also detector cuts, is shown in Fig. 4.12b.

Fig. 4.13 shows the angular distribution obtained from reconstructed dimuons in the simulated SSM Z' sample, with pole-mass at 2.5 TeV. It clearly shows the same behavior as the spin-1 expectation in Fig. 4.12b. Disregarding the end-ranges where the number of entries go to zero due to the detector cuts and parton contributions mentioned earlier, the rest of the distribution

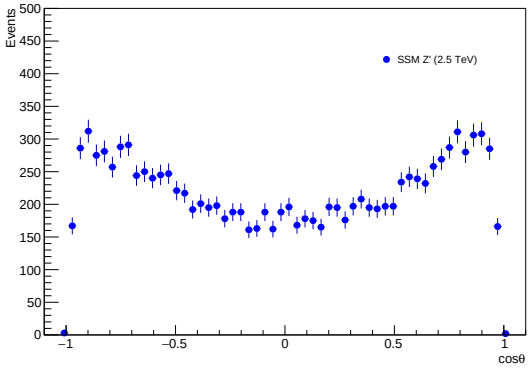

Figure 4.13: Angular distribution of reconstructed dimuons from the SSM Z' signal sample with pole-mass at $m_{\mu\mu} = 2.5$ TeV.

shows that muons are more likely to be produced with angles θ^* close to 0 and π, i.e. $\cos\theta^*$ close to 1 and -1, than with θ^* close to $\pi/2$, i.e. $\cos\theta^*$ close to 0.

The angle θ^* is in Fig. 4.13 given as the angle between the negatively charged muon, μ^-, and the positive z-axis, i.e. parallel to the beam-axis. This is thus the simple case where one does not know whether the angle is taken w.r.t. an incoming quark, anti-quark or a gluon. Hence, a possible forward-backward asymmetry, as is the case for the Z boson due to the parity violating weak interaction, will be washed out for the muons coming from the Z', in this simplified treatment. However, it is still suitable for showing that the muons have been produced by a spin-1 particle.

Studies of the angular distribution of the final-state particles thus provide a way to infer the spin of a new particle causing a resonance in the invariant mass spectrum. However, detailed studies of spin and other quantum numbers of produced resonances are very involved. Due to highly complex distortions imposed by acceptance and efficiency, very complicated corrections have to be calculated and evaluated for their systematic effects, and are therefore beyond the scope of this thesis.

4.8 Summary

A search for resonant deviations from the expected SM background, in the invariant mass spectrum of dimuon final-states, has been performed with the ATLAS detector at the LHC. Data was taken from pp collisions at a center-of-mass energy of $\sqrt{s} = 8$ TeV, during period B in 2012, corresponding to an integrated luminosity of about 5.1 fb^{-1}. The analysis was performed within the new analysis model in ATLAS, developed for Run 2 of data-taking at the LHC. The data was compared to background from SM processes, estimated from Monte Carlo simulated samples, where no significant deviations from the estimated background were found.

The work of this analysis was compared to that of the ATLAS publication on high-mass dilepton resonance search at $\sqrt{s} = 8$ TeV, and integrated luminosity of 20.5 fb^{-1} in the dimuon channel. Comparisons were also made with corresponding ATLAS publications at $\sqrt{s} = 7$ TeV and $\sqrt{s} = 8$ TeV, with integrated luminosities closer to the value considered in the thesis, when the dimuon invariant mass distributions were discussed. The distribution obtained in the thesis was found to match the others in most regards, but with fewer entries than expected in the region of the Z peak, which may partly be caused by neglecting the contribution from two-station muons.

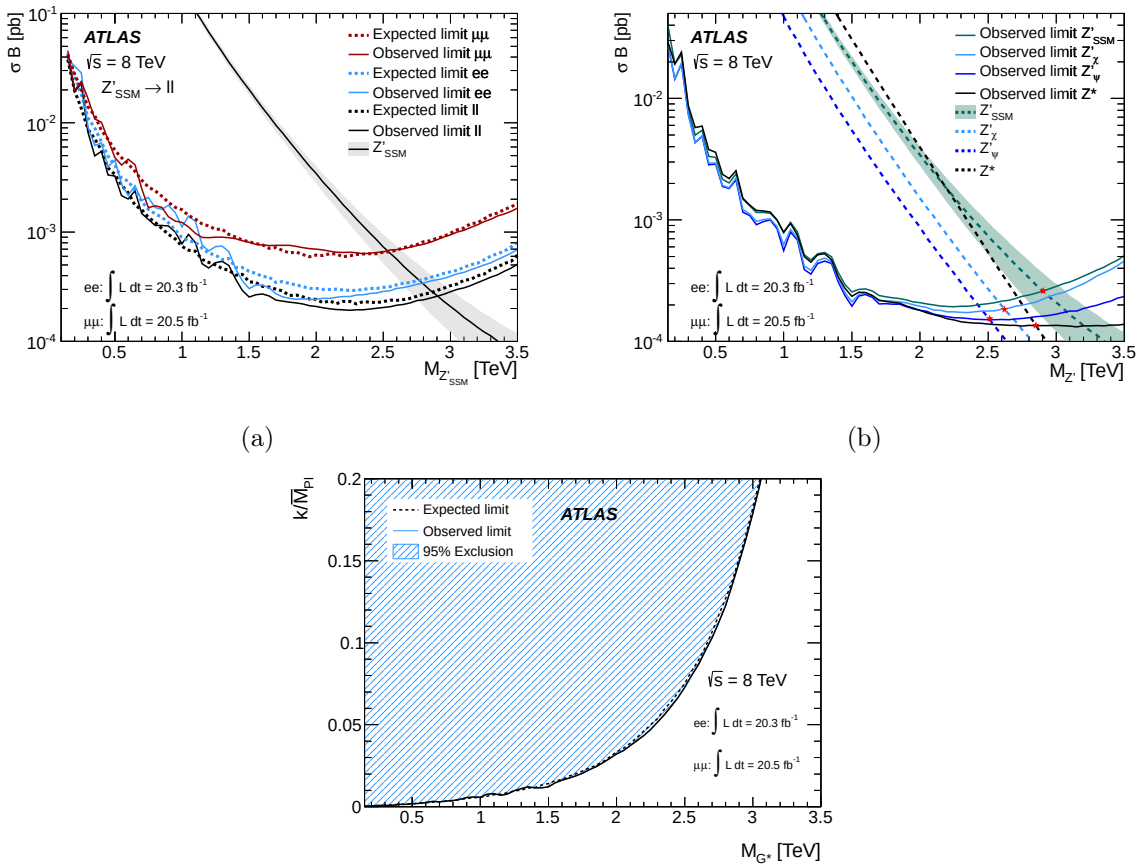

Figure 4.14: Plots of the upper limit of the cross-section times branching ratio at 95 % C.L., as a function of resonance mass, for (a) Z'_{SSM} into dielectrons, dimuons and the two channels combined, (b) in the combined dilepton channel for Z'_{SSM}, the E_6-motivated Z'_ψ and Z'_χ, and Z^*, and (c) for RS graviton excitations, also in the combined dilepton channel. From Ref. [19].

Finally, an outline was given for how angular distributions of the final-state particles can be used to determine the spin of a possible new resonance. This included theoretical expressions for the angular dependence of dileptons produced by bosons of spin-0, spin-1 or spin-2, and a distribution obtained from reconstructed dimuons in one of the simulated Z'_{SSM} samples.

4.9 Experimental limits on new physics

Experimental limits obtained by ATLAS from the dilepton resonance search at $\sqrt{s} = 8$ TeV [19], is shown in Fig. 4.14. In these figures the upper limit on the cross-section times branching ratio at 95 % confidence level (C.L.), is plotted as a function of resonance mass, for Z'_{SSM} into dielectrons, dimuons and the two channels combined in Fig. 4.14a, in the combined dilepton channel for Z'_{SSM}, the E_6-motivated Z'_ψ and Z'_χ, and Z^* in Fig. 4.14b, and for RS graviton excitations in Fig. 4.14c, also this in the combined dilepton channel.

The current lower mass-limits set by ATLAS on dilepton resonances arising from the models considered in Fig. 4.14, are given in Tables 4.15 and 4.16.

Fig. 4.17 shows an event display of the highest invariant mass dimuon event measured by ATLAS during the data-taking at $\sqrt{s} = 8$ TeV. It corresponds to an $m_{\mu\mu}$ of 1.844 TeV.

Model	Width [%]	Observed limit [TeV]	Expected limit [TeV]
Z'_{SSM}	3.0	2.90	2.87
Z'_{χ}	1.2	2.62	2.60
Z'_{ψ}	0.5	2.51	2.46
Z^*	3.4	2.85	2.82

Figure 4.15: Observed and expected lower mass-limits at 95 % C.L. of Z' and Z^* bosons, in the combined dilepton channel. "Width" denotes the fraction of the resonance width compared to the resonance mass. From Ref [19].

$k/\bar{M}_{\mathrm{Pl}}$	0.01	0.03	0.05	0.1	0.2
Observed limit on M_{G^*} [TeV]	1.25	1.96	2.28	2.68	3.05
Expected limit on M_{G^*} [TeV]	1.28	1.95	2.25	2.67	3.05

Figure 4.16: Observed and expected lower mass-limits at 95 % C.L. for RS graviton excitations, with different choices for the warp scale factor k, in the combined dilepton channel. From Ref. [19].

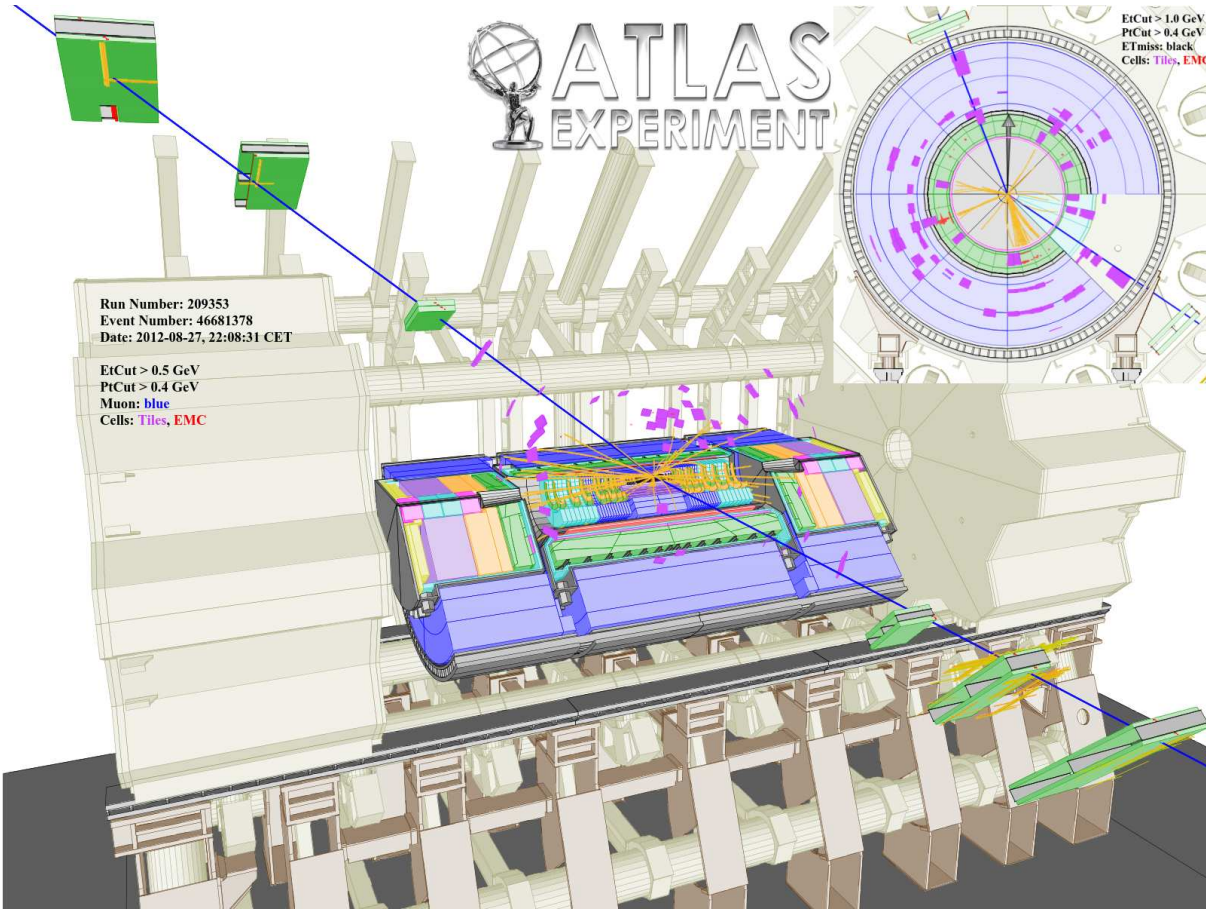

Figure 4.17: An event display of the ATLAS detector, showing the highest invariant mass dimuon event measured by ATLAS in the 2012 data taken at $\sqrt{s} = 8$ TeV. The leading muon has a p_{T} of 653 GeV and an η of 1.25, and the subleading muon has a p_{T} of 646 GeV and an η of -0.85. The invariant mass of the pair is 1844 GeV, i.e. 1.844 TeV.

Chapter 5

13 TeV analysis

The LHC is expected to provide collisions again in June this year (2015), after the first long shut-down period, where machines and equipment have been upgraded to go from a center-of-mass energy of $\sqrt{s} = 8$ TeV at the end of Run 1, to $\sqrt{s} = 13$ TeV for Run 2. Higher collision energy and luminosity provide the possibility of new interactions and other phenomena, which have not been reachable in the previous runs. The collision frequency is planned to be doubled, where the time between bunch crossings will start out at 50 ns, as in Run 1, and then later be halved to 25 ns, which correspond to a frequency of 40 MHz. These new conditions require investigation, in order to find out whether one needs to approach the data-analysis in a different manner compared to Run 1.

The event data model, in which the experimental and simulated data are stored and handled, is also new for this run. This means that the analysis codes need to be re-written in order to access data in the new file format, and to be able to use the new features and tools developed for use with this format. Event selection and cuts must also be re-optimized to accommodate the new conditions.

To prepare for the upcoming data-taking at the higher center-of-mass energy, new Monte Carlo-samples have been generated in order to simulate how the data will look like under the new conditions. As a natural follow-up of the 8 TeV analysis described in the previous section, some of these new simulated samples, which are relevant for dimuon resonance searches, will be looked at.

5.1 Event and muon selection

The selection of events and muons at the higher energy is based on that performed at 8 TeV, with only a couple of changes. There are currently ongoing investigations, performed by researchers working on dilepton analysis within the exotics working group in ATLAS, of how to optimize these selections to the new run. Within the last month before delivery of the thesis, this group has made several changes to the selection for the 13 TeV analysis, compared to what is done in the work of this thesis. These changes include dropping the "2mu14" and "mu24" triggers listed below, in favor of a single muon trigger with a p_{T} threshold of 26 GeV and an isolation requirement, while keeping the "mu50" trigger. The p_{T} cut on single muons is raised to 30 GeV, and each muon track is now going to be matched more closely to its primary vertex, with new significance cuts on impact parameters of the tracks w.r.t. to the vertex. It has also been decided to use an official isolation selection tool, with defined working points for making optimal selections of sufficiently isolated muons.

The selections applied for the work of the thesis are listed below, followed by a more elaborate explanation of the points that differ from the 8 TeV selection. See Sec. 4.1 (from page 41) for

information about the points which are identical to the 8 TeV cuts.

The points which differ from the 8 TeV selections, are underlined. The points which are not marked with any star, do not correspond to any cut applied by the exotic dilepton analysis group at the time of delivery. One star denotes that the corresponding selection is partly the same, while two stars denote that the selection is the same as that applied by this group.

Event level:

- Emulated triggers: HLT_2mu14 or HLT_mu24 or HLT_mu50 *
- ≥ 1 primary vertex, with ≥ 3 tracks and $|z_{\mathrm{PV}}| < 200$ mm
- ≥ 2 combined muons **

Muon level:

- $p_{\mathrm{T}} > 25$ GeV
- $|\eta| < 2.4$ **
- Quality: medium **
- ID hits: Muon Combined Performance requirements for ID hits **
- MS hits: Muon Combined Performance requirements for MS hits **
- $|d_0| < 0.2$ mm
- $|z_0| < 1$ mm
- Isolation: $\sum_{\mathrm{trk}} p_{\mathrm{T}}^{\mathrm{trk}}(\Delta R < 0.3)/p_{\mathrm{T}}^{\mu} < 0.05$

Dimuon level:

- Dimuon candidate with the highest p_{T} scalar sum **
- Muons in the pair have opposite-sign charge **

New triggers have been developed for Run 2, where the names of the highest level triggers have changed from EF (event filter) to HLT (high level trigger). The triggers considered for use in dimuon analysis in the exotics group, were initially the dimuon trigger HLT_2mu14, and the single muon triggers HLT_mu24 and HLT_mu50. The dimuon trigger requires at least two muons with $p_{\mathrm{T}} > 14$ GeV each, for an event to fire this trigger. The two single muon triggers have p_{T} thresholds equal to the numerical value in their names, given in GeV.

Muons are here required to have pseudorapidities within $|\eta| < 2.4$, according to the expected selection in the new run. This corresponds to the coverage of the muon triggers.

5.2 Background estimation

The background processes considered at 13 TeV are in principle the same as for the 8 TeV analysis, where information listed on the twiki page for dilepton analysis within the exotics working group is used for reference[1]. The only difference, at the time of delivery, is that no single-top quark samples (Wt-channel) are mentioned yet for the upcoming run. Hence, only the $t\bar{t}$-process is used to estimate the background from top quarks.

[1] url: `https://twiki.cern.ch/twiki/bin/viewauth/AtlasProtected/DileptonAnalysis2015` (access limited to members of the ATLAS collaboration)

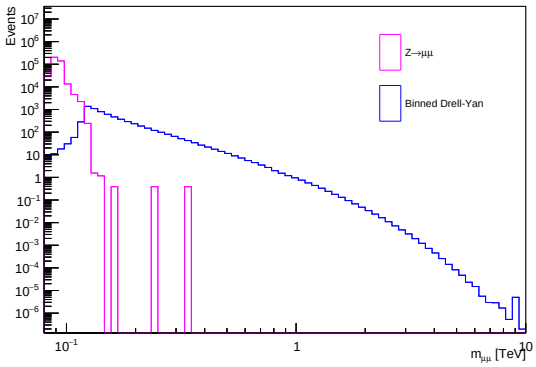

Figure 5.1: Invariant mass distribution of reconstructed (not truth) dimuons from both unbinned and binned Drell-Yan samples. The unbinned Drell-Yan sample ($Z \to \mu\mu$) is stitched to the mass-binned samples by only keeping events where the truth-mass of the Z is below the lowest truth-mass (120 GeV) generated for the mass-binned samples.

Table 5.1: Information on the generators used to produce the simulated samples.

Process	Generator	Parton shower	PDF
Drell-Yan	POWHEG	PYTHIA 8.183	CTEQ6L1
$t\bar{t}$	POWHEG	PYTHIA 6.427.2	CTEQ6L1
Diboson	SHERPA 2.1.1	SHERPA 2.1.1	CT10
Z'	PYTHIA 8.183	PYTHIA 8.183	MSTW2008LO

5.2.1 Monte Carlo samples

The generators and PDFs used to produce the background and signal samples at $\sqrt{s} = 13$ TeV are listed in Table 5.1.

For the Drell-Yan process, there are both so-called "unbinned" and "mass-binned" samples available. The unbinned sample has been generated with a wide range of invariant dimuon masses ($m_{\mu\mu}$), which covers much of the mass region of interest for this search. For the mass-binned samples, the total mass-range of interest is divided into "bins", where each mass-binned sample corresponds to one "bin", generated to give invariant dimuon masses in its given range. The collection of all the mass-binned samples is then a set of complementary "bins", which in total covers the whole mass region of interest. They are produced to give a better background estimate for the Drell-Yan background, with much more statistics than given by the unbinned sample alone. When considered together with the binned samples, the unbinned sample can not be used in its entirety, since that would give an overlap in mass with some of the binned samples, which would lead to "double counting" in such overlapping regions. To avoid this, the truth-information of the generated Z bosons in the unbinned sample is used, to include only events where the Z has a truth-mass of less than 120 GeV, which corresponds to the lower mass-limit of the lowest mass-binned sample. The unbinned sample then covers the $m_{\mu\mu}$-range up to 120 GeV, from where the mass-binned samples take over to give the estimate for higher mass. The reconstructed invariant mass distribution of dimuons for the "stitched" unbinned and binned samples is given in Fig. 5.1.

The Drell-Yan samples, both the binned and unbinned samples, have been generated at NLO with POWHEG, while PYTHIA 8 with the CTEQ6L1 PDF, has taken care of the parton showering and hadronization processes at LO. A summary of these samples is given in Table 5.2

Table 5.2: Information on the simulated Drell-Yan samples.

Process	$m_{\mu\mu}$ [GeV]	MC run	σ_{gen} [pb]	N_{evts}
$Z/\gamma^* \to \mu\mu$		147407	1900.2	4,890,500
$Z/\gamma^* \to \mu\mu$	120-180	203519	17.470	500,000
$Z/\gamma^* \to \mu\mu$	180-250	203520	2.9202	250,000
$Z/\gamma^* \to \mu\mu$	250-400	203521	1.0818	150,000
$Z/\gamma^* \to \mu\mu$	400-600	203522	0.19538	100,000
$Z/\gamma^* \to \mu\mu$	600-800	203523	0.037394	50,000
$Z/\gamma^* \to \mu\mu$	800-1000	203524	0.010604	50,000
$Z/\gamma^* \to \mu\mu$	1000-1250	203525	0.0042578	49,000
$Z/\gamma^* \to \mu\mu$	1250-1500	203526	0.0014218	50,000
$Z/\gamma^* \to \mu\mu$	1500-1750	203527	0.00054520	49,792
$Z/\gamma^* \to \mu\mu$	1750-2000	203528	0.00022990	49,500
$Z/\gamma^* \to \mu\mu$	2000-2250	203529	0.00010387	50,000
$Z/\gamma^* \to \mu\mu$	2250-2500	203530	0.000049394	49,500
$Z/\gamma^* \to \mu\mu$	2500-2750	203531	0.000024452	49,500
$Z/\gamma^* \to \mu\mu$	2750-3000	203532	0.000012487	50,000
$Z/\gamma^* \to \mu\mu$	3000-3500	203533	0.000010027	50,000
$Z/\gamma^* \to \mu\mu$	3500-4000	203534	0.0000029341	49,500
$Z/\gamma^* \to \mu\mu$	4000-4500	203535	0.00000089759	50,000
$Z/\gamma^* \to \mu\mu$	4500-5000	203536	0.00000028069	50,000
$Z/\gamma^* \to \mu\mu$	5000-	203537	0.00000012643	50,000

Table 5.3: Information on the simulated top quark and diboson samples.

Process	MC run	σ_{gen} [pb]	ϵ_{F} [%]	N_{evts}
$t\bar{t}$	110401	695.840	54.316	9,970,500
$WW/WZ/ZZ \to 4l$	200920	1.0467	100.000	1,000,000
$WW/WZ/ZZ \to 2l + 2\nu$	200922	13.820	100.000	4,972,000

Table 5.4: Information on the simulated Z' signal samples.

Process	MC run	σ_{gen} [pb]	N_{evts}
E_6 Z'_χ, $m_{\mu\mu} = 2$ TeV	182920	0.0095960	20,000
E_6 Z'_χ, $m_{\mu\mu} = 3$ TeV	182921	0.00081355	20,000
E_6 Z'_χ, $m_{\mu\mu} = 4$ TeV	182922	0.000095450	20,000
E_6 Z'_χ, $m_{\mu\mu} = 5$ TeV	182923	0.000016605	20,000

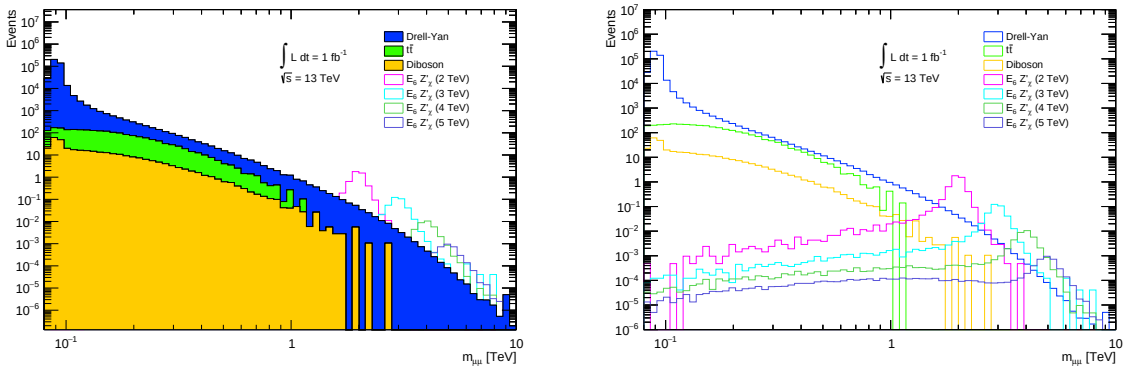

(a) (b)

Figure 5.2: Dimoun invariant mass distributions of data compared to (a) the stacked sum of the backgrounds and (b) each background plotted separately to show their relative contribution to the total estimate. Simulated E_6 Z'_χ signals are overlaid.

The $t\bar{t}$-sample has also been generated with POWHEG at NLO, while for the parton showering PYTHIA 6 has been used with the CTEQ6L1 PDF at LO. A lepton filter has been applied, requiring at least one lepton per event.

SHERPA [41] has handled both the event generation and parton showering for the diboson samples, with the CT10 PDF operating at NLO. Information on the diboson and top samples is given in Table 5.3.

All the background and signal samples considered here are derivation samples (DxAODs called EXOT0), requested by the exotics working group. These derivation samples are specifically made for the kind of search considered in this thesis. The cuts which have been made in the production of these derived samples, ensure that events that contain at least 2 muons with $p_{\mathrm{T}} > 20$ GeV are kept.

5.2.2 Z' signal

At 13 TeV, Z' signal samples based on a grand unification-inspired E_6 model are considered. As for the 8 TeV case, these samples are only used as references to what potential new resonances may look like. Four samples have been produced, each generated with a different pole-mass for the Z'_χ, at 2, 3, 4 and 5 TeV. Information on these signal samples is summarized in Table 5.4. Both the event generation and the parton showering have been taken care of by PYTHIA 8, with the MSTW2008LO PDF at LO.

5.2.3 Invariant mass distribution

The total background estimate of the Drell-Yan, $t\bar{t}$ and diboson processes at $\sqrt{s} = 13$ TeV, with overlaid Z' signals, is shown in Fig. 5.2a. Due to the mass-binned Drell-Yan samples, the contribution from this process to the background is estimated all the way up to dimuon masses of around 10 TeV. The line shape seems smooth up to about 7-8 TeV, where the statistics seem to get lower.

The $t\bar{t}$ and diboson samples run out of statistics at much lower mass; around 1 TeV for the $t\bar{t}$ and around 2 TeV for dibosons. Mass-binned samples for both of these groups of processes will be produced later, to get more statistics and better background estimates for higher mass, but are not available for this work.

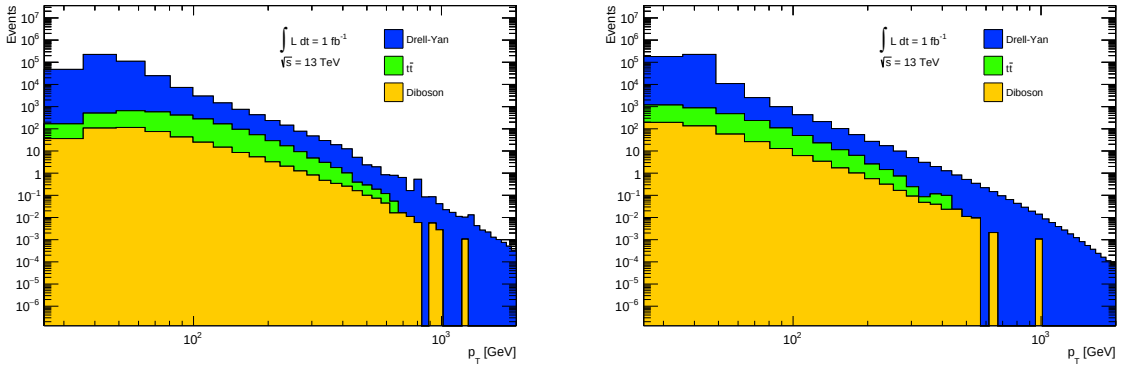

(a) Leading muon.

(b) Sub-leading muon.

Figure 5.3: Transverse momentum of the leading and subleading muons in the dimuon candidates.

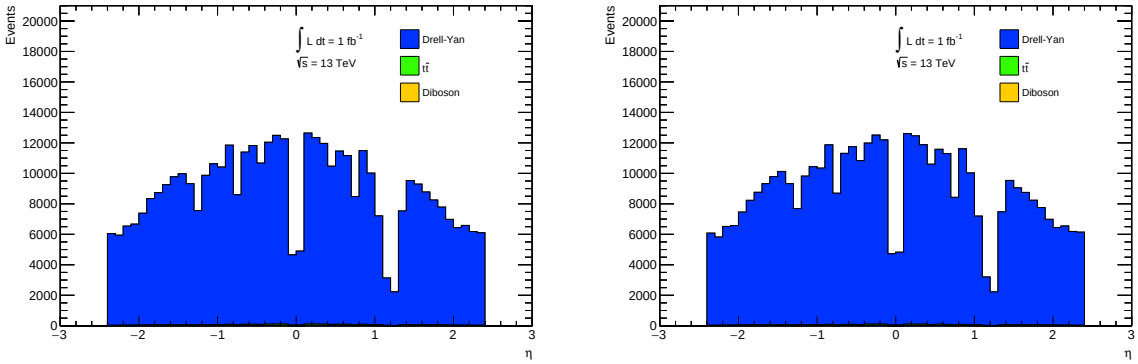

(a) Leading muon.

(b) Subleading muon.

Figure 5.4: Pseudorapidity of the leading and subleading muons in the dimuon candidates.

In Fig. 5.2b the three groups of background processes are not stacked, to show their separate contributions more clearly. Compared to the corresponding invariant mass distribution at $\sqrt{s} = 8$ TeV, shown in Fig. 4.6, the Drell-Yan and diboson show similar behaviour, with approximately the same relative contribution to the total background estimate. The $t\bar{t}$-process, however, seem to be more important at $\sqrt{s} = 13$ TeV compared to $\sqrt{s} = 8$ TeV.

5.2.4 Kinematic properties

The p_{T}-distributions for leading and subleading muons are shown in Figs. 5.3a and 5.3b, respectively. Similar to the corresponding distributions at $\sqrt{s} = 8$ TeV, there is a peak at around half the Z boson mass, due to the Drell-Yan and diboson background processes, where both the leading and subleading muon have taken about half of the total energy of the Z each.

Figs. 5.4a and 5.4b show the pseudorapidities of the leading and subleading muons, respectively, while Figs. 5.5a and 5.5b exhibit the corresponding ϕ-distributions. There are no clear differences between the distributions of the leading and subleading muons, which indicate that the η and ϕ of muons passing the selection criteria are not strongly dependent on the p_{T} of these muons.

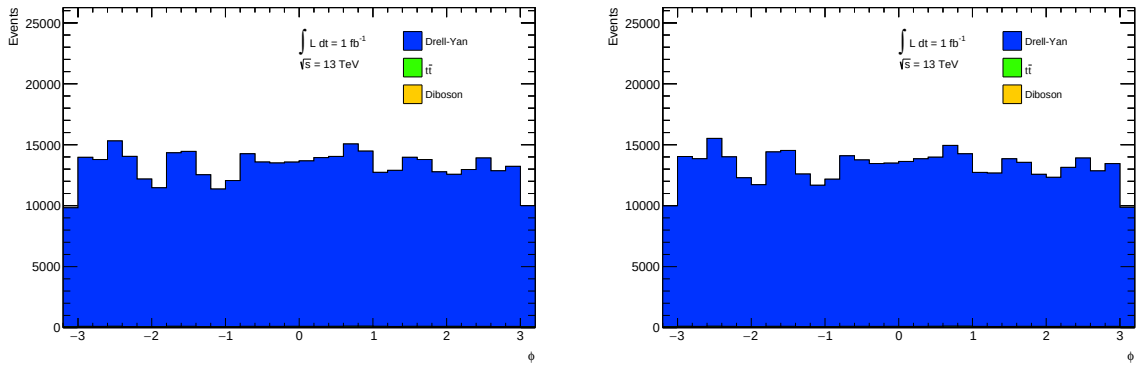

(a) Leading muon.

(b) Subleading muon.

Figure 5.5: ϕ-distributions of the leading and subleading muons in the dimuon candidates.

5.3 Involvement in the exotic dilepton analysis group in ATLAS

As a result of looking into the new 13 TeV samples produced for the new run, it was natural to follow the ongoing work of the group in ATLAS conducting searches for exotic dilepton resonances. The event and muon selections performed in the thesis, along with the samples considered, are based on the information and discussions given in the group's weekly meetings and on its internal twiki page on the web. Approaching the end of my work on the thesis, I presented some of my results from handling the 8 TeV data with the new analysis model, along with my background estimates at 13 TeV, in one of these weekly meetings. I am also listed as co-author on the internal support note, which is going to be the foundation for the upcoming publication of results at $\sqrt{s} = 13$ TeV.

5.4 Summary

As a follow-up to the 8 TeV analysis, new Monte Carlo samples aimed to simulate the new conditions at $\sqrt{s} = 13$ TeV have also been looked at. With event and muon selections similar to those used for the 8 TeV analysis, the SM background has been estimated at the higher energy and luminosity expected in Run 2 at the LHC. The same background processes are considered for 13 TeV, except for the Wt production which, at the time of writing this thesis, was not (yet) considered by the dilepton group performing the corresponding search in ATLAS. In contrast with the 8 TeV analysis, there are mass-binned Drell-Yan samples available for 13 TeV, which have been "stitched" together with the unbinned Drell-Yan sample, to give a background estimate with much higher statistical significance than obtained without such binned samples at 8 TeV.

Conclusions

A search for new resonances in the dimuon invariant mass spectrum, with the ATLAS detector at the LHC, has been performed in this thesis, using data from proton-proton collisions at a center-of-mass energy of $\sqrt{s} = 8$ TeV, taken during period B in 2012 and corresponding to an integrated luminosity of approximately 5.1 fb^{-1}. The analysis was performed in the new analysis model in ATLAS, developed for storage and handling of data in the upcoming run of data-taking at the LHC, scheduled to start in June 2015. The experimental data were compared to the estimated backgrounds, obtained from Monte Carlo simulated samples, which were found to be in relatively good agreement. Hence, no significant deviations from the SM expectations were found. Given that the software for the new analysis model has continuously been under development during the work of this thesis, and that a limited number of data and MC samples for $\sqrt{s} = 8$ TeV have been reprocessed with the new xAOD format, the analysis has been performed completely within the new model, which thereby has been shown to be well functioning in time for Run 2.

New simulated background and signal samples have been produced in ATLAS to prepare for pp collisions at $\sqrt{s} = 13$ TeV. As an extension of the 8 TeV analysis, background estimation with the new 13 TeV samples has also been performed in this thesis, following the ongoing preparations and investigations we conduct for exotic dilepton searches in ATLAS. The most important contribution to the dimuon background in the search region, namely the Drell-Yan process, is estimated with much higher statistics, compared to the 8 TeV analysis of this thesis, due to the inclusion of mass-binned Drell-Yan samples. This gives a higher statistical significance to the background estimate for high masses, where contributions to the $m_{\mu\mu}$ spectrum are obtained all the way up to about 10 TeV. The relative contributions from the Drell-Yan and diboson processes to the total estimate is similar to that obtained for 8 TeV, while the contribution from $t\bar{t}$ is estimated to be somewhat higher for the new conditions.

Sensitivity studies performed in ATLAS show that an integrated luminosity of about 3 fb^{-1} is needed in order to surpass the Run 1 sensitivity in the search for an SSM or E_6 model Z' resonance with a dilepton final-state. This places the exotic dilepton resonance search as one of the "early" Run 2 searches, with the aim of producing first results based on about 2-3 fb^{-1} of ATLAS data collected during pp collisions at $\sqrt{s} = 13$ TeV. Should no new resonance have been discovered in the dimuon channel, after data corresponding to an integrated luminosity of 20 fb^{-1} is collected, preliminary exclusion limits for three selected Z' models have been estimated to be: about 3.1 TeV for the Z'_{ψ}, about 3.4 TeV for the Z'_{χ} and about 3.8 TeV for the Z'_{SSM}.

If a new resonance should be discovered in the dilepton channel, additional detailed studies would be needed in order to determine the origin of the resonance. That would include investigations of its quantum numbers such as spin, which might take a while to conduct due to the complexities of these studies. That is, however, a luxury problem which will have to be dealt with in due time, if we should be so fortunate as to see signs of a new and unknown particle or phenomena.

The startup of Run 2 at the LHC is now right around the corner, and it will be very exciting to see what the first results of the dilepton resonance search will reveal!

Appendices

Appendix A

Data and simulation samples

A.1 8 TeV samples

A.1.1 Experimental data and Good Runs List

Period B 2012

data12_8TeV.periodB.physics_Muons.PhysCont.AOD.repro16_v05

Good Runs List

data12_8TeV.periodB_DetStatus-v61-pro16_DQDefects-00-01-00_PHYS_StandardGRL_All_Good.xml

url: http://atlasdqm.web.cern.ch/atlasdqm/grlgen/All_Good/data12_8TeV.periodB_DetStatus-v61-pro16_DQDefects-00-01-00_PHYS_StandardGRL_All_Good.xml

A.1.2 Simulation

Drell-Yan

mc14_8TeV.147807.PowhegPythia8_AU2CT10_Zmumu.merge.DAOD_STDM3.e1852_s1896_s1912_r5591_r5625_p1796

Top

mc14_8TeV.117050.PowhegPythia_P2011C_ttbar.merge.DAOD_STDM3.e1727_s1933_s1911_r5591_r5625_p1796
mc14_8TeV.110140.PowhegPythia_P2011C_st_Wtchan_incl_DR.merge.DAOD_STDM3.e1743_s1933_s1911_r5591_r5625_p1796

Diboson

WW

mc14_8TeV.126929.PowhegPythia8_AU2CT10_WpWm_me.merge.AOD.e1280_s1933_s1911_r5591_r5625
mc14_8TeV.126930.PowhegPythia8_AU2CT10_WpWm_te.merge.AOD.e2348_s1933_s1911_r5591_r5625
mc14_8TeV.126931.PowhegPythia8_AU2CT10_WpWm_em.merge.AOD.e1280_s1933_s1911_r5591_r5625
mc14_8TeV.126932.PowhegPythia8_AU2CT10_WpWm_mm.merge.AOD.e1280_s1933_s1911_r5591_r5625
mc14_8TeV.126933.PowhegPythia8_AU2CT10_WpWm_tm.merge.AOD.e2348_s1933_s1911_r5591_r5625
mc14_8TeV.126934.PowhegPythia8_AU2CT10_WpWm_et.merge.AOD.e2348_s1933_s1911_r5591_r5625
mc14_8TeV.126935.PowhegPythia8_AU2CT10_WpWm_mt.merge.AOD.e2348_s1933_s1911_r5591_r5625
mc14_8TeV.126936.PowhegPythia8_AU2CT10_WpWm_tt.merge.AOD.e2348_s1933_s1911_r5591_r5625

ZZ

mc14_8TeV.126938.PowhegPythia8_AU2CT10_ZZ_2e2mu_mll4_2pt5.merge.AOD.e1280_s1933_s1911_r5591_r5625
mc14_8TeV.126939.PowhegPythia8_AU2CT10_ZZ_2e2tau_mll4_2pt5.merge.AOD.e2372_s1933_s1911_r5591_r5625
mc14_8TeV.126941.PowhegPythia8_AU2CT10_ZZ_2mu2tau_mll4_2pt5.merge.AOD.e2372_s1933_s1911_r5591_r5625
mc14_8TeV.126940.PowhegPythia8_AU2CT10_ZZ_4mu_mll4_2pt5.merge.AOD.e1280_s1933_s1911_r5591_r5625
mc14_8TeV.126942.PowhegPythia8_AU2CT10_ZZ_4tau_mll4_2pt5.merge.AOD.e2372_s1933_s1911_r5591_r5625
mc14_8TeV.126950.PowhegPythia8_AU2CT10_ZZllnunu_mm_mll4.merge.AOD.e1280_s1933_s1911_r5591_r5625
mc14_8TeV.126951.PowhegPythia8_AU2CT10_ZZllnunu_tt_mll4.merge.AOD.e2372_s1933_s1911_r5591_r5625

WZ

mc14_8TeV.129477.PowhegPythia8_AU2CT10_WZ_Wm11Z11_mll0p250d0_2LeptonFilter5.merge.AOD.e1300_s1933_s1911_r5591_r5625
mc14_8TeV.129478.PowhegPythia8_AU2CT10_WZ_Wm11Z13_mll0p4614d0_2LeptonFilter5.merge.AOD.e1300_s1933_s1911_r5591_r5625
mc14_8TeV.129479.PowhegPythia8_AU2CT10_WZ_Wm11Z15_mll3p804d0_2LeptonFilter5.merge.AOD.e2372_s1933_s1911_r5591_r5625
mc14_8TeV.129480.PowhegPythia8_AU2CT10_WZ_Wm13Z11_mll0p250d0_2LeptonFilter5.merge.AOD.e1300_s1933_s1911_r5591_r5625
mc14_8TeV.129481.PowhegPythia8_AU2CT10_WZ_Wm13Z13_mll0p4614d0_2LeptonFilter5.merge.AOD.e1300_s1933_s1911_r5591_r5625
mc14_8TeV.129482.PowhegPythia8_AU2CT10_WZ_Wm13Z15_mll3p804d0_2LeptonFilter5.merge.AOD.e2372_s1933_s1911_r5591_r5625
mc14_8TeV.129483.PowhegPythia8_AU2CT10_WZ_Wm15Z11_mll0p250d0_2LeptonFilter5.merge.AOD.e2372_s1933_s1911_r5591_r5625
mc14_8TeV.129484.PowhegPythia8_AU2CT10_WZ_Wm15Z13_mll0p4614d0_2LeptonFilter5.merge.AOD.e2372_s1933_s1911_r5591_r5625
mc14_8TeV.129485.PowhegPythia8_AU2CT10_WZ_Wm15Z15_mll3p804d0_2LeptonFilter5.merge.AOD.e2372_s1933_s1911_r5591_r5625
mc14_8TeV.129486.PowhegPythia8_AU2CT10_WZ_W11Z11_mll0p250d0_2LeptonFilter5.merge.AOD.e1300_s1933_s1911_r5591_r5625
mc14_8TeV.129487.PowhegPythia8_AU2CT10_WZ_W11Z13_mll0p4614d0_2LeptonFilter5.merge.AOD.e1300_s1933_s1911_r5591_r5625
mc14_8TeV.129488.PowhegPythia8_AU2CT10_WZ_W11Z15_mll3p804d0_2LeptonFilter5.merge.AOD.e2372_s1933_s1911_r5591_r5625
mc14_8TeV.129489.PowhegPythia8_AU2CT10_WZ_W13Z11_mll0p250d0_2LeptonFilter5.merge.AOD.e1300_s1933_s1911_r5591_r5625
mc14_8TeV.129490.PowhegPythia8_AU2CT10_WZ_W13Z13_mll0p4614d0_2LeptonFilter5.merge.AOD.e1300_s1933_s1911_r5591_r5625
mc14_8TeV.129491.PowhegPythia8_AU2CT10_WZ_W13Z15_mll3p804d0_2LeptonFilter5.merge.AOD.e2372_s1933_s1911_r5591_r5625
mc14_8TeV.129492.PowhegPythia8_AU2CT10_WZ_W15Z11_mll0p250d0_2LeptonFilter5.merge.AOD.e2372_s1933_s1911_r5591_r5625
mc14_8TeV.129493.PowhegPythia8_AU2CT10_WZ_W15Z13_mll0p4614d0_2LeptonFilter5.merge.AOD.e2372_s1933_s1911_r5591_r5625
mc14_8TeV.129494.PowhegPythia8_AU2CT10_WZ_W15Z15_mll3p804d0_2LeptonFilter5.merge.AOD.e2372_s1933_s1911_r5591_r5625

Z' signal

mc14_8TeV.158027.Pythia8_AU2MSTW2008LO_Zprime_mumu_SSM1500.merge.AOD.e1242_s1933_s1911_r5591_r5625
mc14_8TeV.158028.Pythia8_AU2MSTW2008LO_Zprime_mumu_SSM2000.merge.AOD.e1242_s1933_s1911_r5591_r5625
mc14_8TeV.158029.Pythia8_AU2MSTW2008LO_Zprime_mumu_SSM2500.merge.AOD.e1242_s1933_s1911_r5591_r5625

A.2 13 TeV samples

A.2.1 Simulation

Drell-Yan

Unbinned

mc14_13TeV.147407.PowhegPythia8_AZNLO_Zmumu.merge.DAOD_EXOT0.e3059_s1982_s2008_r5787_r5853_p1846

Mass-binned

mc14_13TeV.203519.PowhegPythia8_AZNLOCTEQ6L1_DYmumu_120M180.merge.DAOD_EXOT0.e3150_s1982_s2008_r5787_r5853_p1846
mc14_13TeV.203520.PowhegPythia8_AZNLOCTEQ6L1_DYmumu_180M250.merge.DAOD_EXOT0.e3150_s1982_s2008_r5787_r5853_p1846
mc14_13TeV.203521.PowhegPythia8_AZNLOCTEQ6L1_DYmumu_250M400.merge.DAOD_EXOT0.e3150_s1982_s2008_r5787_r5853_p1846
mc14_13TeV.203522.PowhegPythia8_AZNLOCTEQ6L1_DYmumu_400M600.merge.DAOD_EXOT0.e3150_s1982_s2008_r5787_r5853_p1846
mc14_13TeV.203523.PowhegPythia8_AZNLOCTEQ6L1_DYmumu_600M800.merge.DAOD_EXOT0.e3150_s1982_s2008_r5787_r5853_p1846
mc14_13TeV.203524.PowhegPythia8_AZNLOCTEQ6L1_DYmumu_800M1000.merge.DAOD_EXOT0.e3150_s1982_s2008_r5787_r5853_p1816
mc14_13TeV.203525.PowhegPythia8_AZNLOCTEQ6L1_DYmumu_1000M1250.merge.DAOD_EXOT0.e3150_s1982_s2008_r5787_r5853_p1846
mc14_13TeV.203526.PowhegPythia8_AZNLOCTEQ6L1_DYmumu_1250M1500.merge.DAOD_EXOT0.e3150_s1982_s2008_r5787_r5853_p1846
mc14_13TeV.203527.PowhegPythia8_AZNLOCTEQ6L1_DYmumu_1500M1750.merge.DAOD_EXOT0.e3150_s1982_s2008_r5787_r5853_p1846
mc14_13TeV.203528.PowhegPythia8_AZNLOCTEQ6L1_DYmumu_1750M2000.merge.DAOD_EXOT0.e3150_s1982_s2008_r5787_r5853_p1846
mc14_13TeV.203529.PowhegPythia8_AZNLOCTEQ6L1_DYmumu_2000M2250.merge.DAOD_EXOT0.e3150_s1982_s2008_r5787_r5853_p1846
mc14_13TeV.203530.PowhegPythia8_AZNLOCTEQ6L1_DYmumu_2250M2500.merge.DAOD_EXOT0.e3150_s1982_s2008_r5787_r5853_p1846
mc14_13TeV.203531.PowhegPythia8_AZNLOCTEQ6L1_DYmumu_2500M2750.merge.DAOD_EXOT0.e3150_s1982_s2008_r5787_r5853_p1846
mc14_13TeV.203532.PowhegPythia8_AZNLOCTEQ6L1_DYmumu_2750M3000.merge.DAOD_EXOT0.e3150_s1982_s2008_r5787_r5853_p1846
mc14_13TeV.203533.PowhegPythia8_AZNLOCTEQ6L1_DYmumu_3000M3500.merge.DAOD_EXOT0.e3150_s1982_s2008_r5787_r5853_p1846
mc14_13TeV.203534.PowhegPythia8_AZNLOCTEQ6L1_DYmumu_3500M4000.merge.DAOD_EXOT0.e3150_s1982_s2008_r5787_r5853_p1846
mc14_13TeV.203535.PowhegPythia8_AZNLOCTEQ6L1_DYmumu_4000M4500.merge.DAOD_EXOT0.e3150_s1982_s2008_r5787_r5853_p1846
mc14_13TeV.203536.PowhegPythia8_AZNLOCTEQ6L1_DYmumu_4500M5000.merge.DAOD_EXOT0.e3150_s1982_s2008_r5787_r5853_p1846
mc14_13TeV.203537.PowhegPythia8_AZNLOCTEQ6L1_DYmumu_5000M.merge.DAOD_EXOT0.e3150_s1982_s2008_r5787_r5853_p1846

Top

mc14_13TeV.110401.PowhegPythia_P2012_ttbar_nonallhad.merge.DAOD_EXOT0.e2928_s1982_s2008_r5787_r5853_p1846

Diboson

mc14_13TeV.200920.Sherpa_CT10_llll.merge.DAOD_EXOT0.e3213_s1982_s2008_r5787_r5853_p1846
mc14_13TeV.200922.Sherpa_CT10_llvv.merge.DAOD_EXOT0.e3213_s1982_s2008_r5787_r5853_p1846

Z' signal

mc14_13TeV.182920.Pythia8_AU2MSTW2008LO_Zprime_NoInt_mumu_E6Chi2000.merge.DAOD_EXOT0.e3150_s1982_s2008_r5787_r5853_p1846
mc14_13TeV.182921.Pythia8_AU2MSTW2008LO_Zprime_NoInt_mumu_E6Chi3000.merge.DAOD_EXOT0.e3150_s1982_s2008_r5787_r5853_p1846
mc14_13TeV.182922.Pythia8_AU2MSTW2008LO_Zprime_NoInt_mumu_E6Chi4000.merge.DAOD_EXOT0.e3150_s1982_s2008_r5787_r5853_p1846
mc14_13TeV.182923.Pythia8_AU2MSTW2008LO_Zprime_NoInt_mumu_E6Chi5000.merge.DAOD_EXOT0.e3150_s1982_s2008_r5787_r5853_p1846

Bibliography

[1] M. Thomson, *Modern particle physics*, Cambridge University Press (2013)

[2] B. R. Martin, *Nuclear and particle physics*, Second Edition, John Wiley & Sons, Ltd (2009)

[3] ATLAS Collaboration, *Observation of a new particle in the search for the Standard Model Higgs boson with the ATLAS detector at the LHC*, Phys. Lett. B **716**, 1 (2012)

[4] CMS Collaboration, *Observation of a new boson at a mass of 125 GeV with the CMS experiment at the LHC*, Phys. Lett. B **716**, 30 (2012)

[5] F. Englert, R. Brout, *Broken Symmetry and the Mass of Gauge Vector Mesons*, Phys. Rev. Lett. **13**, 321 (1964)

[6] P.W. Higgs, *Broken symmetries, massless particles and gauge fields*, Phys. Lett. **12**, 132 (1964)

[7] P.W. Higgs, *Broken Symmetries and the Masses of Gauge Bosons*, Phys. Rev. Lett. **13** 508 (1964)

[8] G.S. Guralnik, C.R. Hagen, T.W.B. Kibble, *Global Conservation Laws and Massless Particles*, Phys. Rev. Lett. **13** 585 (1964)

[9] P.W. Higgs, *Spontaneous Symmetry Breakdown without Massless Bosons*, Phys. Rev. **145** 1156 (1966)

[10] T.W.B. Kibble, *Symmetry Breaking in Non-Abelian Gauge Theories*, Phys. Rev. **155** 1554 (1967)

[11] ATLAS and CMS Collaborations, *Combined Measurement of the Higgs Boson Mass in pp Collisions at $\sqrt{s} = 7$ and 8 TeV with the ATLAS and CMS Experiments*, Phys. Rev. Lett. **114**, 191803 (2015)

[12] F. Mandl and G. Shaw, *Quantum field theory*, Second Edition, John Wiley & Sons, Ltd (2010)

[13] R. N. Mohapatra, *Unification and Supersymmetry*, Springer, Berlin (1986)

[14] M. V. Chizhov and G. Dvali, *Origin and phenomenology of weak-doublet spin-1 bosons*, Phys. Lett. B **703**, 593 (2011)

[15] S. Weinberg, *Implications of dynamical symmetry breaking: An addendum*, Phys. Rev. D **19**, 1277 (1979)

[16] L. Randall and R. Sundrum, *Large mass hierarchy from a small extra dimension*, Phys. Rev. Lett. **83**, 3370 (1999)

[17] D. London and J. L. Rosner, *Extra gauge bosons in E_6*, Phys. Rev. D **34**, 1530 (1986)

[18] P. Langacker, *The physics of heavy Z' gauge bosons*, Rev. Mod. Phys. **81**, 1199 (2009)

[19] ATLAS Collaboration, *Search for high-mass dilepton resonances in pp collisions at $\sqrt{s}$ = 8 TeV with the ATLAS detector*, Phys. Rev. D **90** 052005 (2014)

[20] ATLAS Collaboration, *The ATLAS Experiment at the CERN Large Hadron Collider*, JINST **3**, S08003 (2008)

[21] A. Miucci, *The ATLAS Insertable B-Layer project*, JINST **9** C02018 (2014)

[22] R. Brun, F. Rademakers, *ROOT - An object oriented data analysis framework*, Proceedings of the AIHENP'96 Workshop, Lausanne, Sep. 1996, Nucl. Instr. and Meth. in Phys. A **389** (1997) 81-86. See also `http://root.cern.ch/`

[23] M. Elsing, R. Seuster, G. Stewart, V. Tsulaia, *Status and future evolution of the ATLAS offline software*, Proceedings of the 21st International Conference on Computing in High Energy and Nuclear Physics (CHEP2015) J. Phys.: Conf. Ser.

[24] A. Buckley, T. Eifert, M. Elsing, D. Gillberg, K. Koeneke, A. Krasznahorkay, E. Moyse, M. Nowak, S. Snyder, P. Van Gemmeren, *Implementation of the ATLAS Run 2 event data model*, Proceedings of the 21st International Conference on Computing in High Energy and Nuclear Physics (CHEP2015) J. Phys.: Conf. Ser.

[25] J. Catmore, J. Cranshaw, T. Gillam, E. Gramstad, P. Laycock, N. Ozturk, G. A. Stewart, *A new petabyte-scale data derivation framework for ATLAS*, Proceedings of the 21st International Conference on Computing in High Energy and Nuclear Physics (CHEP2015) J. Phys.: Conf. Ser.

[26] M. Borodin, K. De, J. Navarro, A. Klimentov, T. Maeno, A. Vaniachine, *Scaling up ATLAS production system for the LHC Run 2 and beyond: project ProdSys2*, Proceedings of the 21st International Conference on Computing in High Energy and Nuclear Physics (CHEP2015) J. Phys.: Conf. Ser.

[27] ATLAS Collaboration, *The ATLAS Simulation Infrastructure*, Eur. Phys. J. C **70**, 823 (2010)

[28] S. Agostinelli et al. (GEANT4 Collaboration), *Geant4 - a simulation toolkit*, Nucl. Instrum. Methods Phys. Res., Sect. A **506**, 250 (2003)

[29] ATLAS Collaboration, *Search for Dilepton Resonances in pp Collisions at s¿=7¿¿TeV with the ATLAS Detector*, Phys. Rev. Lett. **107**, 272002 (2011)

[30] S. Alioli, P. Nason, C. Oleari, and E. Re, *A general framework for implementing NLO calculations in shower Monte Carlo programs: the POWHEG BOX*, J. High Energy Phys. 06 (2010) 043

[31] T. Sjöstrand, S. Mrenna, and P. Z. Skands, *A brief introduction to PYTHIA 8.1*, Comput. Phys. Commun. **178**, 852 (2008)

[32] H.-L. Lai, M. Guzzi, J. Huston, Z. Li, P. M. Nadolsky, J. Pumplin, and C.-P. Yuan, *New parton distributions for collider physics*, Phys. Rev. D 82, 074024 (2010)

[33] T. Sjöstrand, S. Mrenna, and P. Z. Skands, *PYTHIA 6.4 physics and manual*, J. High Energy Phys. 05 (2006) 026

[34] J. Pumplin, D. R. Stump, J. Huston, H.-L. Lai, P. Nadolsky, and W.-K. Tung, *New Generation of Parton Distributions with Uncertainties from Global QCD Analysis*, J. High Energy Phys. 07 (2002) 012

[35] P. Golonka and Z. Was, *PHOTOS Monte Carlo: a precision tool for QED corrections in Z and W decays*, Eur. Phys. J. C **45**, 97 (2006)

[36] A. D. Martin, W. J. Stirling, R. S. Thorne, and G. Watt, *Parton distributions for the LHC*, Eur. Phys. J. C **63**, 189 (2009)

[37] M. J. Woudstra (on behalf of the Atlas Collaboration), *Performance of the ATLAS muon trigger in pp collisions at* $\sqrt{s} = 8$ *TeV*, J. Phys.: Conf. Ser. **513** 012040 (2014)

[38] ATLAS Collaboration, *Search for high-mass resonances decaying to dilepton final states in pp collisions at* $\sqrt{s} = 7$ *TeV with the ATLAS detector*, J. High Energy Phys. 11 (2012) 138

[39] ATLAS Collaboration, *Search for high-mass dilepton resonances in 6.1/fb of pp collisions at* $\sqrt{s} = 8$ *TeV with the ATLAS experiment*, ATLAS-CONF-2012-129

[40] P. Osland, A. A. Pankov, A. V. Tsytrinov, and N. Paver, *Spin identification of the Randall-Sundrum resonance in lepton-pair production at the CERN LHC*, Phys. Rev. D **78**, 035008 (2008), arXiv:0805.2734v2 [hep-ph]

[41] T. Gleisberg, S. Hoche, F. Krauss, M. Schonherr, S. Schumann, F. Siegert, and J. Winter, *Event generation with Sherpa 1.1*, J. High Energy Phys. 02 (2009) 007